

AD\_\_\_\_\_

Award Number: W81XWH-11-2-0076

TITLE: New Methods of Low-Field Magnetic Resonance Imaging for Application to Traumatic Brain Injury

PRINCIPAL INVESTIGATOR: Matthew S. Rosen, Ph.D.

CONTRACTING ORGANIZATION: Harvard University, Cambridge MA 02138

REPORT DATE: February 2013

TYPE OF REPORT: Annual

PREPARED FOR: U.S. Army Medical Research and Materiel Command  
Fort Detrick, MD 21702-5012

DISTRIBUTION STATEMENT:

X Approved for public release; distribution unlimited

Distribution limited to U.S. Government agencies only;  
report contains proprietary information

The views, opinions and/or findings contained in this report are those of the author(s) and should not be construed as an official Department of the Army position, policy or decision unless so designated by other documentation.



REPORT DOCUMENTATION PAGE				Form Approved OMB No. 0704-0188	
Public reporting burden for this collection of information is estimated to average 1 hour per response, including the time for reviewing instructions, searching existing data sources, gathering and maintaining the data needed, and completing and reviewing this collection of information. Send comments regarding this burden estimate or any other aspect of this collection of information, including suggestions for reducing this burden to Department of Defense, Washington Headquarters Services, Directorate for Information Operations and Reports (0704-0188), 1215 Jefferson Davis Highway, Suite 1204, Arlington, VA 22202-4302. Respondents should be aware that notwithstanding any other provision of law, no person shall be subject to any penalty for failing to comply with a collection of information if it does not display a currently valid OMB control number. <b>PLEASE DO NOT RETURN YOUR FORM TO THE ABOVE ADDRESS.</b>					
1. REPORT DATE (DD-MM-YYYY) February 2013		2. REPORT TYPE Annual		3. DATES COVERED (From - To) 10January2012-9January2013	
4. TITLE AND SUBTITLE New Methods of Low-Field Magnetic Resonance Imaging for Application to Traumatic Brain Injury				5a. CONTRACT NUMBER	
				5b. GRANT NUMBER W81XWH-11-2-0076	
				5c. PROGRAM ELEMENT NUMBER	
6. AUTHOR(S) Matthew S. Rosen, PhD				5d. PROJECT NUMBER	
				5e. TASK NUMBER	
				5f. WORK UNIT NUMBER	
7. PERFORMING ORGANIZATION NAME(S) AND ADDRESS(ES) Harvard University, Cambridge MA 02138				8. PERFORMING ORGANIZATION REPORT NUMBER	
9. SPONSORING / MONITORING AGENCY NAME(S) AND ADDRESS(ES) USAMRAA U.S. Army Medical Research and Materiel Command Fort Detrick, MD 21702-5012				10. SPONSOR/MONITOR'S ACRONYM(S)	
				11. SPONSOR/MONITOR'S REPORT NUMBER(S)	
12. DISTRIBUTION / AVAILABILITY STATEMENT  Approved for public release; distribution unlimited.					
13. SUPPLEMENTARY NOTES					
14. ABSTRACT We are developing robust low-magnetic-field implementations of MRI (LFI) focused on brain imaging with two complimentary test scanner systems: electromagnet and permanent magnet based. We are also developing injury-sensitive MRI based on the detection of free radicals associated with injury using the Overhauser effect and subsequently imaging that modified nuclear polarization using low-field MRI (OMRI). Much of the hardware development of the human head LFI test bed systems and the OMRI system is now complete. We now focused on imaging sequence development and optimization, image reconstruction, and the implementation of parallel imaging acceleration. We have successfully demonstrated high-speed free-radical OMRI, and investigated the sensitivity of spectroscopy- and image-based measurements to free radical concentrations as a path toward <i>in vivo</i> applications. Application of the suite of techniques and technologies from our work could advise future development of a deployable device with a high diagnostic impact, transforming diagnosis and monitoring of secondary injury prevalent in TBI.					
15. SUBJECT TERMS Low-field brain MRI, Injury-sensitive MRI, Free radical Overhauser imaging.					
16. SECURITY CLASSIFICATION OF:			17. LIMITATION OF ABSTRACT  UU	18. NUMBER OF PAGES  96	19a. NAME OF RESPONSIBLE PERSON USAMRMC
a. REPORT U	b. ABSTRACT U	c. THIS PAGE U			19b. TELEPHONE NUMBER (include area code)



# Table of Contents

<b>INTRODUCTION:</b>	<b>5</b>
<b>BODY:</b>	<b>6</b>
<b>Low Field Imager (LFI)</b>	<b>6</b>
<b>TASK 1A: Low-field MRI Hardware Development</b>	<b>6</b>
<i>BIPLANAR ELECTROMAGNET LFI OPTIMIZATION:</i>	
<i>3D SEQUENCE DEVELOPMENT</i>	<b>7</b>
<i>3D FAST IMAGING USING B-SSFP</i>	<b>8</b>
<i>COMPRESSED SENSING AND UNDERSAMPLED B-SSFP</i>	<b>9</b>
<i>HALBACH ARRAY (PERMANENT MAGNET) LFI</i>	<b>11</b>
<i>NMR-BASED FIELD MAPPING</i>	<b>12</b>
<i>IN-PLANE (XY) AND SLICE (Z) SPATIAL ENCODING STRATEGY</i>	<b>15</b>
<i>RF TRANSMIT COILS</i>	<b>16</b>
<i>RF RECEIVE COIL ARRAYS</i>	<b>17</b>
<i>RF TRANSMIT PULSES</i>	<b>19</b>
<i>1D PROJECTIONS &amp; 2D IMAGING</i>	<b>21</b>
<i>ENCODING &amp; RECONSTRUCTION SIMULATIONS</i>	<b>23</b>
<i>FUTURE WORK</i>	<b>23</b>
<i>PARALLEL-ARRAY DETECTORS FOR THE ELECTROMAGNET LFI</i>	<b>24</b>
<i>RECEIVE COIL DEVELOPMENT</i>	<b>24</b>
<i>DATA PROCESSING AND OLE AUTOMATION</i>	<b>26</b>
<i>8 CHANNEL IMAGE ACQUISITION AND RECONSTRUCTION</i>	<b>27</b>
<b>TASK 1B: System control and image acquisition</b>	<b>34</b>
<i>INTEGRATION OF TECMAG REDSTONE CONSOLE WITH THE HARDWARE OF TASK 1A:</i>	<b>34</b>
<i>BEGIN DEVELOPMENT OF IMAGE NAVIGATION AND RECONSTRUCTION METHODS:</i>	<b>35</b>
<b>OMRI Injury Imaging</b>	<b>36</b>



<b>TASK 2A: OMRI Hardware Development</b>	<b>36</b>
<i>EPR COIL DESIGN FOR OMRI 3D RADICAL IMAGING</i>	<b>36</b>
<i>3D OVERHAUSER MRI USING B-SSFP</i>	<b>37</b>
<b>TASK 2B: In vitro nitroxide Overhauser-enhanced proton spectroscopy</b>	<b>42</b>
<i>OVERHAUSER DNP SENSITIVITY TO FREE RADICALS</i>	<b>42</b>
<i>INVESTIGATION OF FREE RADICAL SENSITIVITY IN OMRI B-SSFP IMAGING SEQUENCES</i>	<b>43</b>
<b>TASK 2C: Ex vivo nitroxide detection in whole blood</b>	<b>45</b>
<b>KEY RESEARCH ACCOMPLISHMENTS:</b>	<b>46</b>
<b>REPORTABLE OUTCOMES:</b>	<b>47</b>
<b>CONCLUSION:</b>	<b>48</b>
<b>REFERENCES:</b>	<b>50</b>
<b>APPENDICIES:</b>	<b>53</b>
<i>YEAR 2 STATEMENT OF WORK</i>	<b>54</b>
<i>ABSTRACTS ACCEPTED FOR PRESENTATION</i>	<b>55</b>
<i>MANUSCRIPT ACCEPTED FOR PUBLICATION</i>	<b>61</b>



## INTRODUCTION:

Year Two of this applied research program continues to build on recent advances by our collaboration in the development of novel methods of low-magnetic-field MRI and advanced MRI hardware. Without major innovation, high-field MRI instruments offer limited utility for imaging TBI in widely deployable contexts. We focus our research effort on the high-risk and critical challenges that must be solved to enable deployment of a transportable human-head MRI system applicable to TBI imaging in battlefield medical facilities. Our goal is to establish proof-of-principle of a suite of techniques and technologies to advise future development of a field-deployable device with high diagnostic impact. This research effort has two specific aims:

**Specific Aim 1:** Develop a low-field human-head MRI system (LFI) suitable for high-resolution multi-nuclear imaging, and improve the ability to attain brain images based on the intrinsic *in vivo*  $^1\text{H}$  NMR signal in this scanner.

This includes the development of robust low-field scanner hardware methodologies (both electromagnet and permanent magnet based), the development of novel high-speed parallel imaging detection systems, and work on advanced adaptive reconstruction methods including navigators and sparse sampling.

**Specific Aim 2:** Develop injury-sensitive MRI based on converting the electron spin of free radicals associated with injury (specifically TBI) into nuclear polarization using the Overhauser effect and subsequently imaging that modified nuclear polarization using low-field MRI (**OMRI**). Successful demonstration of OMRI of free radicals associated with injury will be directly applicable to the MRI systems of **Aim 1**, enhancing image-based injury specificity and/or shortening scan acquisition time.

The development of this new MRI contrast mechanism may provide an unambiguous non-invasive *in vivo* marker for cerebral injury, and has potential for assisting the imaging of TBI at both low and high magnetic fields.



## BODY:

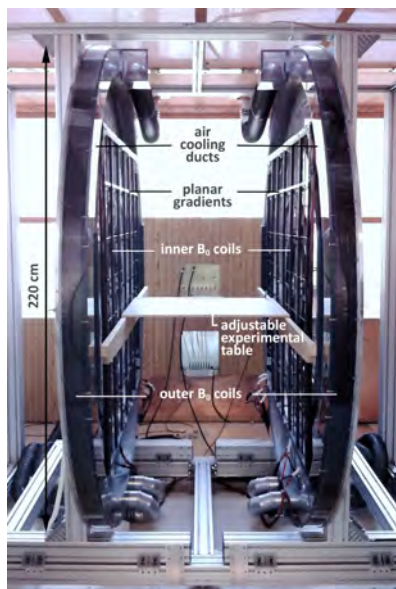
Progress in Year 2 has focused on the demonstration of the low-field MRI hardware developed during Y1 for both the human head **LFI** systems (**Aim 1**) and for the **OMRI** system (**Aim 2**). Additionally, we have successfully combined aspects of Aim 1 and Aim 2, and developed a new method of Overhauser enhanced MRI that dramatically improves the attainable speed and resolution of free radical imaging and offering new perspectives for the measurement of free radicals *in vivo*.

## Low Field Imager (LFI)

### TASK 1A: Low-field MRI Hardware Development

Much of the hardware development for the human head LFI test bed systems (Aim 1) and for the OMRI system (Aim 2) was completed in Y1. Progress in Y2 for Aim 1 focused on imaging sequence development and optimization, and implementation of parallel imaging acceleration. Aim 2 efforts included work to maximizing the OMRI signal attainable from free-radical test solutions with a minimum of applied Overhauser power. We have also successfully demonstrated high-speed free-radical OMRI, and investigated both spectroscopy- and image-based sensitivity to free radical concentrations as a path toward *in vivo* applications.

The electromagnet LFI (shown below) has been optimized to provide an ideal state-of-the art test bed for all of the novel acquisition, detection methodologies, and reconstruction algorithms including navigators



and sparse sampling, and additionally will provide necessary experience and data to advise optimal construction and magnetic field for any future electromagnet-based deployable systems. Currently, this state-of-the-art scanner enables high-performance spectroscopy and 8-channel imaging at 6.5 mT, and is fully equipped for Overhauser DNP experiments.

The permanent magnet system is a lightweight (45 kg) and portable Halbach array. This Halbach array scanner is a highly specialized and potentially disruptive technology scanner that could greatly ease both the cost and burden of a field-forward instrument purpose-built for TBI imaging. This Halbach imager contrasts markedly with the electromagnet LFI in that it has a highly inhomogeneous magnetic field, but we intend to use this inhomogeneity to our advantage and use it to acquire head images without the use of an additional gradient set.



## Biplanar electromagnet LFI optimization: 3D sequence development

Given the success we had in late Y1 in optimizing the biplanar electromagnet LFI magnetic performance (shown in the field maps in Figure 3 of the Y1 Annual Report), we have been able to quickly design and optimize 3D gradient echo sequences in order to demonstrate low-field  $^1\text{H}$  in a nominal head-sized phantom at 6.5 mT. The imaging phantom used for these demonstrations is a plastic cylinder filled with doped water. It contains internal structures of varying shapes and patterns and is a commercially available clinical MRI calibration phantom. We acquired a fully 3D gradient echo imaging dataset (Figure 1) on the LFI, demonstrating that we can resolve structures inside the phantom.

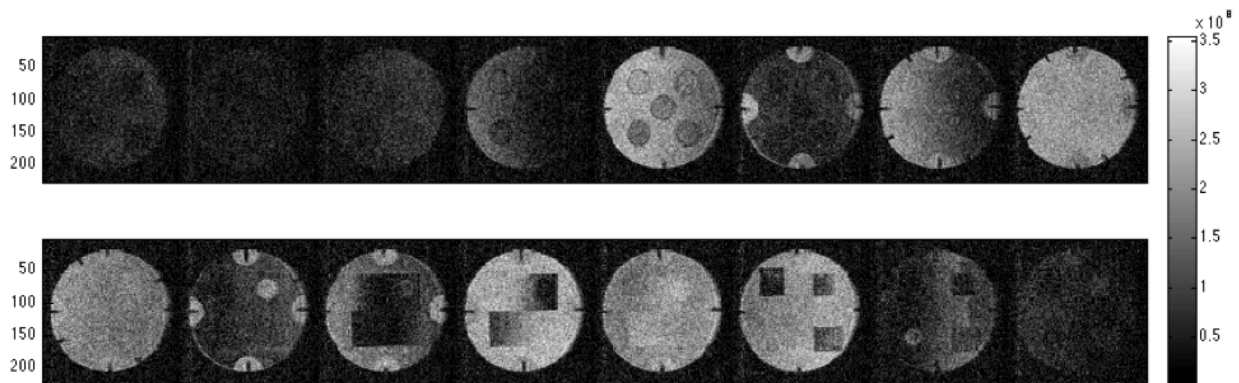


Figure 1: 3D gradient echo MRI data set of the Siemens Multipurpose-Phantom acquired in the LFI at 6.5 mT (276 kHz) with a single channel solenoid detector. Matrix= $128 \times 90 \times 16$ , FOV= $250 \times 190 \times 190 \text{ mm}^3$ , voxel size= $2 \times 2 \times 12 \text{ mm}^3$ , TE/TR=27/338 ms,  $\alpha=90^\circ$ . Number of averages = 40. Total MR scan time was 5 h 24 min. This data was moved from the TNMR/Redstone console and processed using our in-house data pipeline previously described in the Y1 annual report.

The homogeneity of the LFI static magnetic field over this large field of view ( $250 \times 250 \times 200 \text{ mm}$ ) allowed us to achieve  $2 \text{ mm} \times 2 \text{ mm}$  in plane resolution in the phantom for a 12 mm thick slice. A MATLAB package was written to process 3D rendered images from the acquired datasets, and the 3D rendered MRI dataset is shown alongside a photograph of the imaging phantom in Figure 2. The quality of this image, while extremely impressive for such a low magnetic field, required a very long acquisition time, more than 5 hours. Our next steps in optimizing the LFI system focused on reducing this acquisition time. This development and implementation of more efficient imaging sequences, as well as the use of the parallel array coils effort is described in the following sections.



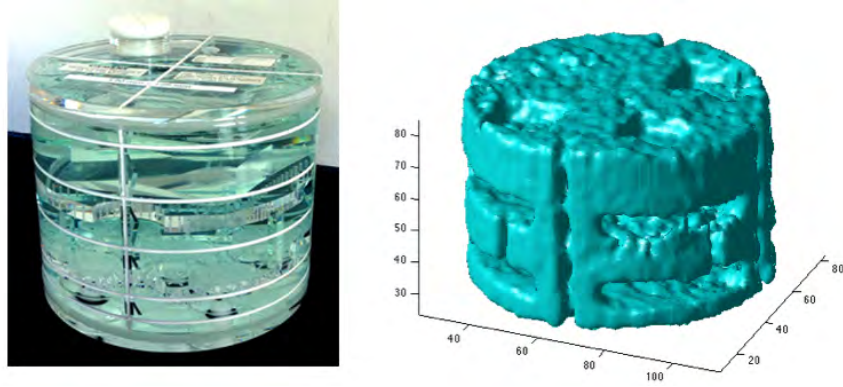


Figure 2: **(Left)** Photograph of cylindrical “Siemens Multipurpose Phantom E” filled with doped water. The inner diameter is 170 mm, and the inner axial length is 125 mm. **(Right)** 3D rendering of the gradient echo MRI data set acquired in LFI at 6.5 mT. This data set was moved from the TNMR/Redstone console and processed in MATLAB using our in-house data pipeline previously described in the Y1 annual report.

### Biplanar electromagnet LFI optimization: 3D fast imaging using b-SSFP

The next steps in optimizing the LFI system focus on *significantly* reducing this acquisition time using fast imaging techniques. Fast imaging was implemented in the electromagnet LFI using 3D balanced steady state free precession sequences (b-SSFP). In contrast with conventional gradient echo sequences, this sequence saves considerable time by recycling the magnetization flipped in the transverse plane during the acquisition, eliminating the extra delays typically used for  $T_2$  decay and  $T_1$  recovery. The pulse sequence diagram is shown in Figure 3. The b-SSFP excitation train consists of an initial  $-\alpha/2$  preparation pulse immediately followed by a train of alternating  $\pm\alpha$  excitation pulses as previously described by Scheffler *et al.* [1]

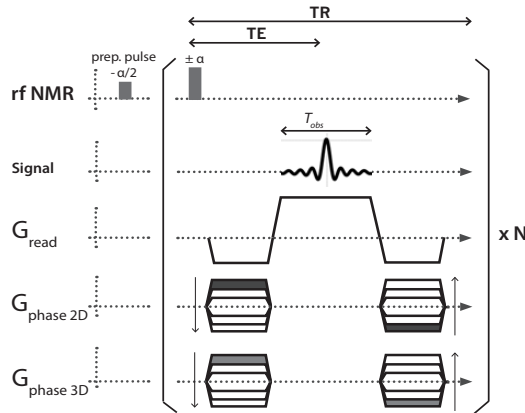


Figure 3: Diagram of the 3D b-SSFP sequence.  $N$  is the total number of TRs in the sequence

The  $\pm\alpha$  pulses are separated by a time  $TR$  and the time interval between the  $-\alpha/2$  preparation pulse and the first  $\alpha$  pulse is  $TR/2$ . Of critical importance to successful implementation of b-SSFP in the LFI is a very stable magnetic field, as off-resonance effects can distort the image and cause severe banding artifacts (Scheffler, 2003). MRI images of a bell pepper were acquired with this b-SSFP sequence in the LFI scanner (Figure 4). To the best of our knowledge, these results represent the first time that b-SSFP has been suc-



cessfully implemented in a low magnetic field scanner and represents a *tremendous* improvement for high speed MRI at low magnetic field, representing more than a 25-fold time savings.

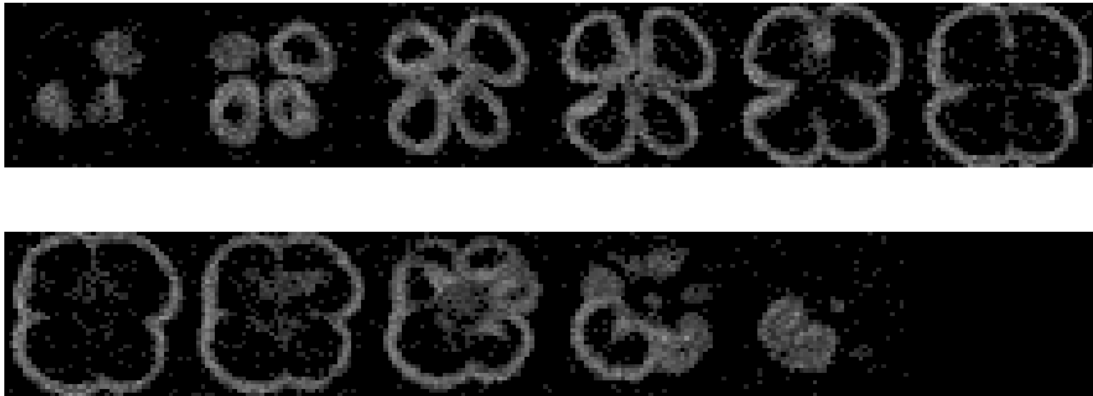


Figure 4: 3D b-SSFP MRI of a bell pepper acquired in the LFI 6.5 mT (276 kHz) with a single channel solenoid detector coil. **Total acquisition time: 12 minutes.** TE/TR=20/40 ms, Matrix=128×41×11, voxel size=2.5×2.4×10 mm<sup>3</sup>,  $\alpha = 90^\circ$ . Number of averages (NA) = 45. This data was moved from the TNMR/Redstone console and processed using our in-house data pipeline previously described in the Y1 annual report.

### Biplanar electromagnet LFI optimization: compressed sensing and undersampled b-SSFP

In order to further improve the temporal resolution attainable using low-field b-SSFP imaging, we investigated the combination of compressed sensing (CS) algorithms and undersampling strategies in the electromagnet LFI. Most images are sparse in the sense that they can be accurately represented with fewer coefficients than one would assume given their spectral bandwidth [2]. Compressed sensing (CS) is a framework for exploiting sparsity to reconstruct high-fidelity MR images from undersampled  $k$ -space datasets that do not fulfill the Nyquist sampling theorem [3]. The use of CS in MRI relies on the possibility to acquire a priori compressed information and be able to reconstruct the original image as if the latter was fully sampled [4]. In the context of data acquisition, this motivates the use of undersampling (US). Compressed sensing has been found to work best when  $k$ -space is randomly undersampled so as to produce incoherent artifacts rather than the familiar wrap-around ghosts due to field-of-view (FOV) contraction when  $k$ -space lines are skipped in a regular coherent pattern as is done in conventional parallel imaging [5]. For the images presented here, a choice was made to acquire random lines of  $k$ -space chosen in the phase-encode directions ( $ky$ ,  $kz$ ) following a Gaussian probability density function. The readout direction was fully sampled. The standard deviations of the sampling pattern as a fraction of the FOV along  $y$  and  $z$ ,  $\sigma_y$  and  $\sigma_z$  respectively, were adjusted manually to preserve adequate high-frequency information for each undersampling rate.

The 3D imaging experiments presented here were performed using b-SSFP with Cartesian acquisition of  $k$ -space at 6.5 mT (276 kHz), using a bell pepper as an imaging phantom. 50% undersampling of  $k$ -space was achieved using a Gaussian probability density function with  $\sigma_y$  and  $\sigma_z = 0.14$ . The sequence was set with TE/TR = 14/29.2 ms, NA=10, acquisition matrix = 64×32×11, voxel size = 2×3×9 mm<sup>3</sup>. The readout duration was 7.04 ms with a total readout bandwidth of 9091 Hz. Total acquisition time was 1 min 40 s. For comparison purpose, a fully sampled dataset using the same bell pepper was also acquired with 3×



many averages. The sequence was set with the same parameters as described above but with acquisition matrix =  $64 \times 64 \times 11$  and  $NA=30$ . The total acquisition time in the fully sampled case was 10 min. Figure 5 shows (A) the fully sampled  $k$ -space and (B) the 50% US  $k$ -space. The variable-density strategy used in the undersampled dataset preserves the center of  $k$ -space more than the edges. This strategy preserves low spatial frequencies in the image (*i.e.*, intensity) while minimizing losses in high spatial frequencies that can result in image blurring.

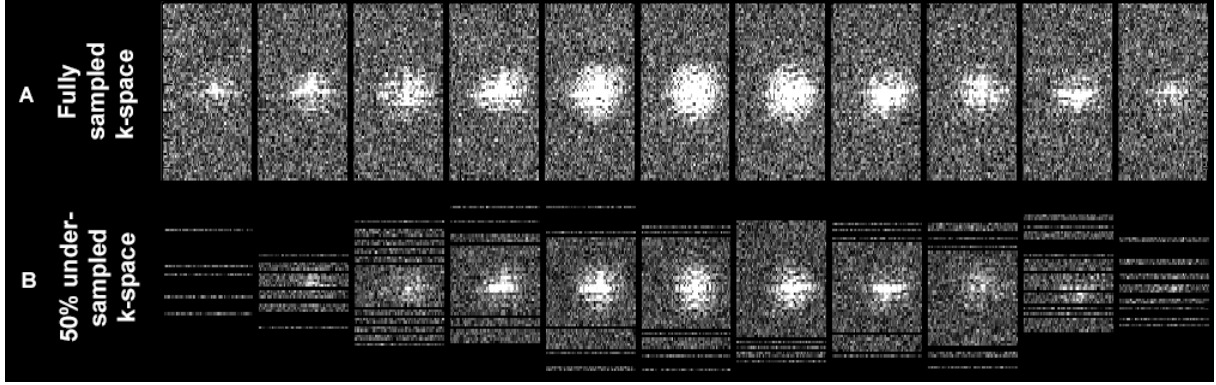


Figure 5: Eleven partitions of the  $k$ -space b-SSFP data set are shown for (A) a fully sampled and (B) a 50% undersampled bell pepper. Acquisition is at 6.5 mT (276 kHz) with a single 10 cm solenoid detector.

Images reconstructed from the  $k$ -space data of Figure 5 are shown in Figure 6. The maximum signal to noise ratio (SNR) is 14.6 in the fully sampled image (Figure 6A) and 12.4 in the 50% undersampled image (Figure 6B). Although the SNR is smaller in the case of the undersampled dataset, it is not substantially less than the fully sampled  $k$ -space, despite being acquired 6 $\times$  faster. This is due to the non-sampled lines in  $k$ -space being identically replaced by zeros before reconstruction, thus decreasing the noise floor. The compressed sensing algorithm is then applied to the undersampled  $k$ -space, further decreases the noise floor with a final SNR of 30 (Figure 6C), more than 2 $\times$  higher than the fully acquired dataset with  $NA=30$ . The efficiency of the CS reconstruction can be particularly seen in the extremities of the image (Figure 6C, slices 1, 9, 10), where the object features may be recovered despite low acquired signal magnitudes (Figure 6B).

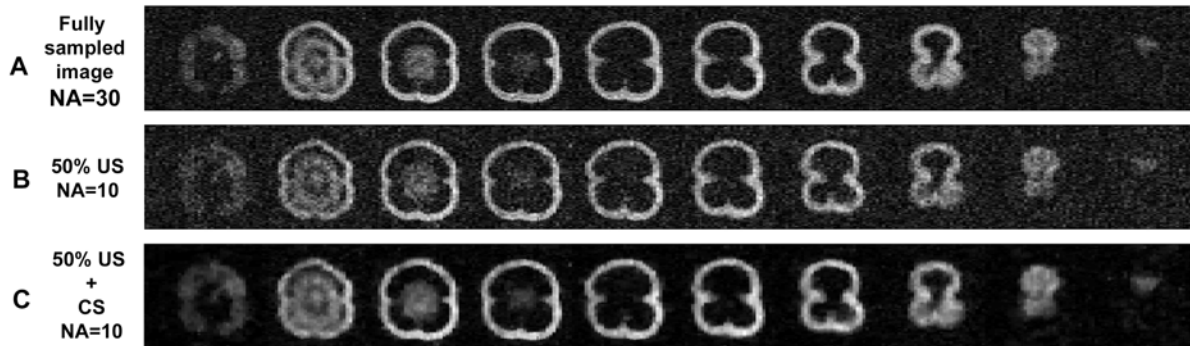


Figure 6: 10 slices of the bell pepper reconstructed from the b-SSFP data set in Figure 5 (A) fully sampled  $k$ -space with  $NA=30$ , (B) 50% undersampled  $k$ -space with  $NA=10$  and (C) 50% undersampled  $k$ -space with  $NA=10$  after CS reconstruction. Total acquisition time is 10 min for (A) and 1 min 40 s for (C).



A 3D reconstruction of the undersampled image of Figure 6C is shown in Figure 7. These imaging experiments with the optimized electromagnet LFI are compelling: high quality 1H MRI at 6.5 mT is in fact attainable over reasonable averaging times using high performance hardware and advanced MRI sequences. We successfully implemented compressing sensing and  $k$ -space undersampling strategies at 6.5 mT; 3D MRI with 50% undersampling and compressed sensing was obtained in 1 min 40 s, providing 2 $\times$  higher SNR and 6 $\times$  faster acquisition compared to a fully sampled acquisition with 3 $\times$  more averages (NA=30). This work shows high potential to overcome the main limitations of working at low field, which typically results in poor SNR and prohibitively long acquisition times. In this study, undersampling fractions of 50 % gives unperceivable reconstruction errors when compared to fully sampled data sets.



Figure 7: Three views of the 3D render of the undersampled b-SSFP data set of Figure 6 shown in false color. Total acquisition time 1 min 40 s. NA=10. TE/TR: 14.4/29.2 ms. Matrix=64 $\times$ 64 $\times$ 11.  $\alpha$ =90.

A critical question for this work will be understanding the clinical balance and impact that the tradeoff between acquisition time and resolution implicit in imaging plays on the operation of a deployable scanner. Time-critical triage and treatment decisions may be able to be made in the field with lower resolution images—acquired with the right contrast—obtained very quickly. The question of what is “good enough” is evolving, and careful attention to the individual needs of point-of-care physicians such as neurointensivists will guide this work going forward.

### Halbach array (permanent magnet) LFI

The second LFI test bed scanner we have been developing is based around a lightweight array of permanent magnets in a so-called Halbach configuration. This magnet is ideal for portable MRI in that it creates a relatively uniform field transverse to the head without the use of a cryostat or power supplies. This Halbach array scanner is a highly specialized scanner and a potentially disruptive technology that could greatly ease both the cost and burden of a field-forward instrument purpose-built for TBI imaging. This Halbach imager contrasts markedly with the electromagnetic LFI in that it has a highly inhomogeneous magnetic field, but we intend to use this inhomogeneity to our advantage and use it to acquire head images without the use of an additional gradient set.

A truly portable MR system has the potential to quickly detect brain injury at the site of injury. For example hemorrhage detection is critical for both stroke patients and traumatic brain injury victims. In stroke, rapid distinction between a hemorrhagic and non-hemorrhagic event could allow administration of a clot-busting drug such as tPA (tissue plasminogen activator) in an ambulance prior to transportation to the



hospital, perhaps advancing this time-sensitive treatment by up to an hour. Subdural hemorrhage (or hematoma) is a form of traumatic brain injury, in which blood gathers between the dura and arachnoid mater (in meningeal layer) and is likely to be visualized on coarse resolution (e.g. 5mm) T1 images.

In Y1 we designed and built a very portable 45 kg Halbach array magnet for portable MRI, and mapped the magnetic field and drift of the using rudimentary NMR measurements at 3.3 MHz. The Halbach LFI in this measurement configuration described below is show in Figure 8. In Y2 we focused on the hardware and encoding techniques needed to turn this magnet into an imager. These developments are described in the subsections below.



Figure 8: The Halbach LFI in the configuration used to take the FID and echo data. The solenoid transmit coil and the single turn loop receive surface coil are visible. The non-magnetic rollers that will be used to rotate the magnet around the sample for spatial encoding are visible at the bottom of the photograph (orange). A 300 mm ruler is shown for scale.

The Neodymium-Iron-Boron (NdFeB) magnets used in our Halbach array have a very high energy density and residual induction, maximizing the strength of the  $B_0$  magnetic field and consequently the NMR signal. Unfortunately, NdFeB also has a significant coefficient of magnetic field drift with temperature ( $\sim 0.08\%/C$ ). As our nonlinear image reconstruction method depends critically on an accurate knowledge of the frequency map within the object, we have taken steps to monitor and stabilize the temperature during imaging experiments. We have insulated the Halbach array from sunlight and the ambient air temperature using a thick-walled Styrofoam enclosure. Additionally, we have implemented real-time monitoring of the temperature using a thermocouple with an Agilent LXI Data Acquisition Unit. Based on these temperature measurements, scanner frequency drifts can be built into the image reconstruction using the known drift coefficient for the material.

### Halbach array LFI: NMR-based field mapping

Our initial field maps in Y1 were obtained using a robotic 3-axis Hall-effect Gauss meter. These field maps were measured off-site and could not be easily repeated *in situ* to provide up-to-date calibration of the center frequency prior to imaging data acquisition. The problem with this approach is that mapping a 3D



volume is relatively slow and the Halbach field may drift with temperature during the time that probe is being translated throughout the imaging volume. As generalized image reconstruction relies on accurate knowledge of the encoding matrix, it is critical that we accurately model the fields produced in our experiment during the reconstruction process.

To perform on-site field mapping, an array of 8 NMR probes [6] were built and mounted on a horizontal rail (Figure 9). Each probe consists of a solenoid tightly wound around a 3-mm diameter NMR tube filled with water doped to reduce  $T_1$  to  $\sim 25$  ms. The solenoid probes are capacitively tuned to resonate at the nominal Larmor frequency at the center of the Halbach magnet and have sufficient bandwidth to acquire signals anywhere in the bore. The probes are excited with a short broadband RF pulse and free induction decays are recorded. The FFT of each probe signal is fit with a Lorentzian lineshape, providing an estimate of the frequency within each probe. The rail is then translated along the axis of the Halbach bore and the measurements are repeated. Additional spokes on the frequency map are acquired by rotating the Halbach around the probes. The resulting set of frequencies was approximated by a third-order polynomial to generate the spatial field map used for image reconstruction. Data acquired using this procedure is shown in Figure 10.



Figure 9: Array of 8 miniature NMR field probes spaced at regular intervals along a positioning arm. The arm is mounted on a fixed cylinder that is concentric with the bore of the Halbach magnet. The magnet is rotated around the field probes, allowing the frequency to be measured at different points within the bore. The arm can also be translated along  $z$  to acquire additional slices for the field map. Ruler marks are mm. Water bulbs are 3 mm.



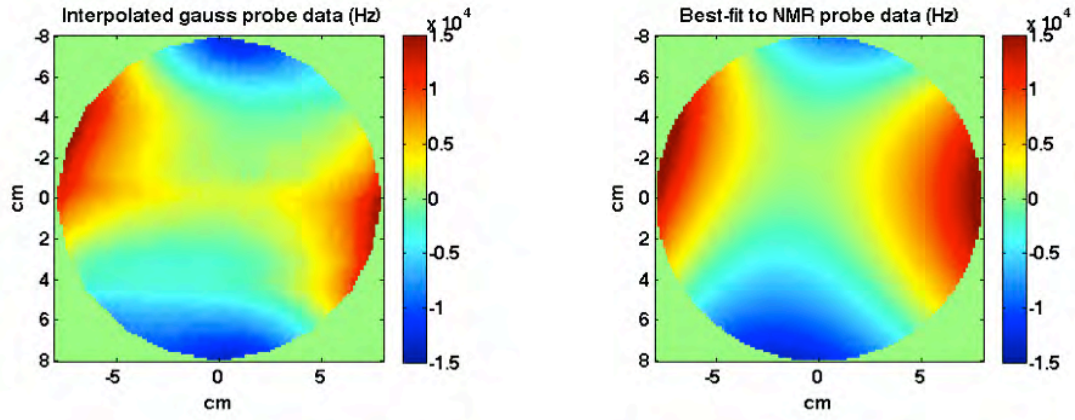


Figure 10: Field maps generated using interpolated gauss meter measurements (**left**) show the same quadrupolar shape as field maps generated from NMR field probe signals using a third-order polynomial fit (**right**). The transverse slice at  $z=0$  is shown. This verifies the utility of our *in situ* NMR mapping system

At our latitude, the Earth’s magnetic field is approximately 0.5 gauss. This field can introduce an appreciable shift in the Halbach field maps as the magnet is rotated—a contribution to the  $^1\text{H}$  Larmor frequency of 2.129 kHz—biasing the image reconstruction and potentially ruining the images.

The 3-mm field probes weren’t sufficiently small enough to map the spatial variation of the Halbach magnetic field particularly near the edge of the field of view. This limited spatial resolution results in a broad NMR line that makes it difficult to accurately measure the frequency at a point in space. To circumvent this problem, we built a second array of 7 field probes using 1-mm water-filled capillaries. While the signal-to-noise ratio (SNR) is substantially reduced due to the small sample size, the smaller probes allow us to more accurately sample the frequency at each point in the Halbach. Signal averaging is used to recover the lost SNR, and this new magnetic field map is shown in Figure 11.

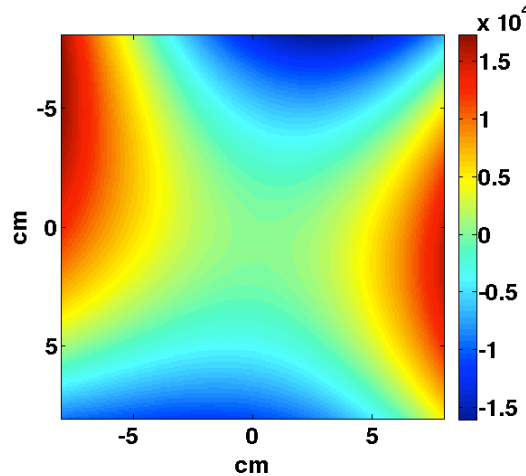


Figure 11: Field map slice from magnet mid-plane obtained using array of seven 1-mm field probes to improve frequency localization along “spokes” in space. Frequencies acquired along 16 spokes were fit with spherical harmonics up to third order to create the resulting map for use in image reconstruction. An additional “navigator” probe was used to remove the effects of the earth’s magnetic field as well as temperature drift.



The sources of bias in our field maps caused by (1) thermal drift of the rare earth magnets in the array and (2) the varying contribution of the earth’s magnetic field as the orientation of the Halbach  $B_0$  field changes with rotation angle (while acquiring different projections) were eliminated by building one additional 1-mm “navigator” NMR probe and attaching it to the frame of the Halbach array so that it remains at the same Halbach frequency isocontour as the magnet rotates. By quickly taking 16 frequency measurements with this probe at different rotation angles, we were able to measure the component of the earth’s magnetic field that is aligned with the Halbach  $B_0$  field. The resulting frequency plot versus angle was a sinusoid with amplitude of 2 kHz. Equipped with this knowledge, we were then able to use the navigator probe during imaging experiments to track thermal drift of the  $B_0$  field over longer time scales. Any frequency change not caused by the component of the earth’s field along  $B_0$  was assumed to result from temperature drift. This drift (typically on the order of hundreds of Hz per hour) is then built into the encoding matrix during image reconstruction. Additionally, the navigator probe can be used to track changes caused by other external field sources, such as those produced by the electromagnet LFI system with which the Halbach experiment shares laboratory space.

### Halbach array LFI: in-plane ( $xy$ ) and slice ( $z$ ) spatial encoding strategy

The magnetic field produced by the Halbach array has a roughly 50 kHz variation over a head-sized FOV. The shape of the inhomogeneity is approximately a second-order hyperbolic field, with higher-order impurities. Rather than consider this ‘built in’ inhomogeneity as an obstacle to imaging, we exploit this “intrinsic” gradient field as a way to perform in-plane spatial encoding. By analogy to PATLOC [7] and O-Space [8] imaging, 1D NMR projections taken with a nonlinear encoding field may be used to reconstruct an image using an iterative matrix solver. The Halbach imager magnet is then rotated around the head (in either a stepped or continuous manner) and signals are acquired at each rotation angle, providing independent projections of the head. For a second-order field, the resolution is best near the periphery, where the field variation is the greatest. Further spatial encoding is provided by the encircling array of RF receiver coils during signal detection. We have modeled this spatial encoding method (Figure 12 and Figure 13) and based on the real parameters of our magnet expect this approach to provides good image quality in the transverse ( $xy$ ) plane.



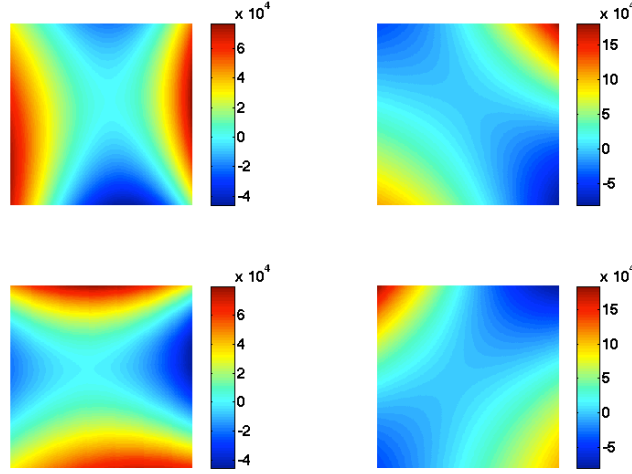


Figure 12: Different projections of the object are acquired by mechanically rotating the Halbach array around its axis. Here four rotation angles are shown for a representative transverse slice near the center of the array. The background homogeneous component of the magnetic field has been subtracted out to emphasize the spatial variation of the field (plotted in Hz).

Methods for spatial encoding in the Z-direction are presently under investigation. One potential approach is to acquire thin, curvilinear “onion skin” isocontours in the inhomogeneous field using narrowband RF pulses. Another method is to use two oppositely-oriented linear phase RF transmit coils to impart z-phase ramps across the object during a spin echo train readout, effectively performing phase encoding in the slice direction [9], [10]. We continue to investigate both of these slice-encoding methods.

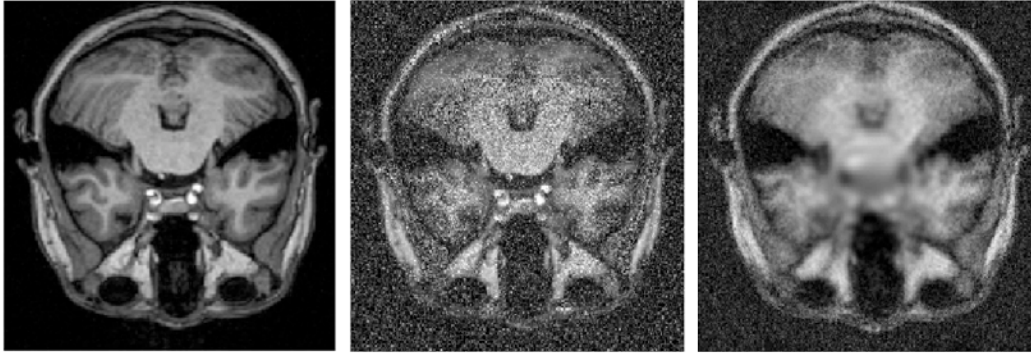


Figure 13: Simulated Halbach array reconstructions in the presence of noise (SNR  $\sim 6$ ). The reference object (**left**) is contaminated with Gaussian noise equivalent to our expected SNR (**center**). A 64-projection Halbach acquisition is simulated using the measured magnetic fields. The image (**right**) is the reconstruction using the Kaczmarz iterative method, a solver well-suited to large matrices that can not be directly inverted. The nonlinearity of the Halbach field causes spatially-varying resolution, with sharp image detail at the periphery and blurring at the center. Slice selection has not been incorporated into this simulation.

### Halbach array LFI: RF transmit coils

Because the magnetic field produced by the permanent magnet Halbach LFI is oriented along the transverse X direction, RF excitation of the spins requires a transmit B1 field oriented in the YZ plane. The so-



lenoid coil geometry is a simple and efficient way to meet this requirement since it may be wound along the axis of the Halbach array and nested within the magnet. This configuration provides a homogeneous B1 field oriented along Z. In order to excite spins across the range of frequencies present within the bore of the magnet, the frequency response of the transmit coil is broadened by a resistor placed in series with the inductive solenoid. Resistive broadening reduces the coil quality factor  $Q$  from  $\sim 90$  to  $\sim 18$ , providing sufficient bandwidth for the Halbach imager. To detune the transmit coil during RF reception, a PIN diode with a suitably long carrier lifetime is added at the input to the coil. This prevents noise in the transmit system from coupling into the receiver coils and overloading the high-gain pre-amp. A diode biasing circuit was built using an op-amp comparator and a TTL logic pulse generated by the Tecmag Apollo spectrometer.

## Halbach array LFI: RF receive coil arrays

The wide frequency range over the imaging area of the Halbach magnet ( $\sim 50$  kHz) with a nominal Larmor frequency of 3.3 MHz means the quality factor of tuned received coils must be less than  $Q = 3.3 \text{ MHz}/50 \text{ kHz} = 66$ . It is difficult to achieve a  $Q$  this low without adding resistance that in general raises the noise-temperature of the coil. Therefore, we considered using “untuned” coils, i.e. coils that possess only a self-resonance high off-resonance. A coil comparison was done to find the coil geometry that provided the highest SNR in the Halbach magnet as a function of configuration. The untuned coils are 8 cm diameter circular loop coils that were connected to the MITEQ preamplifier through a reactive bandpass filter. It was difficult to keep the experimental setup constant, as the mean Larmor frequency of the magnet drifts with temperature, and the SNR depends strongly on the exact position of the coil and sample in the magnet. Therefore, several iterations of SNR measurements were done over 5 days and averages.

It was concluded that an 8 cm, 1 turn, untuned coil design would provide the best SNR given the magnet and preamplifier. This is also a very simple geometry to implement. A single surface coil was used in the center of the magnet with a 2 cm sphere of water as a sample to collect FIDs (Figure 14, left) and spin echoes (Figure 14, right) and spin-echo trains (Figure 15) In particular, our ability to acquire spin-echo trains out to more than 128 echoes is key to enabling imaging using spin echo-based imaging sequences such as RARE.

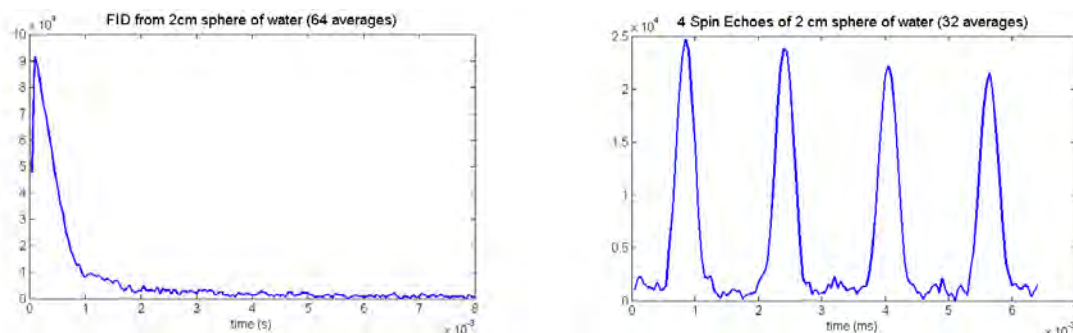


Figure 14: **(Left)** Free induction decay (NA=64) and **(right)** four spin echoes from a CPMG sequence (NA=32) obtained from a 2 cm sphere of water using an 8 cm, 1 turn, untuned, receive coil at 3.3 MHz in the Halbach magnet.



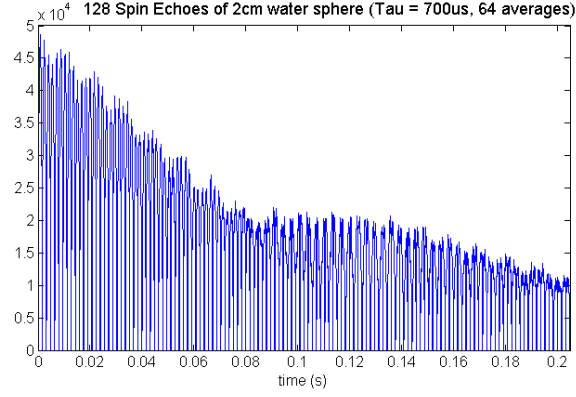


Figure 15: 128 spin echoes acquired using a CPMG sequence with phase cycling at 3.3 MHz in the Halbach magnet. Only the tops of the echoes are sampled. SW=20 kHz, 32 points, NA=64.

An 8 coil receive array was constructed using the 1 turn untuned coils determined to be optimal in the table above in order to perform parallel imaging. These 8 cm coils have an overlap of about 1.5 cm for geometric decoupling of the coils [11]. A photograph of this 8-coil array is shown in Figure 16.

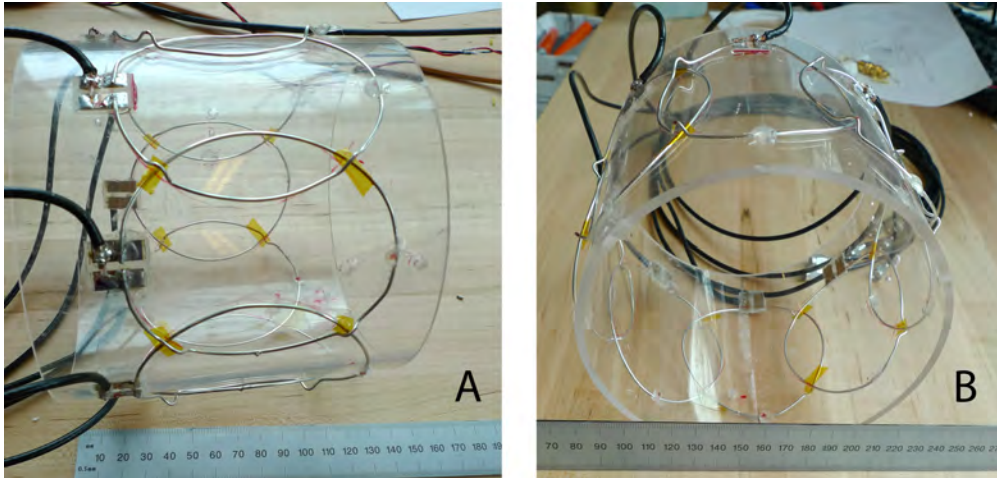


Figure 16: Eight-channel receive array for the Halbach imager.

A multiplexing switch has been developed to acquire data from an 8-channel receive array using the single available receive channel on the Apollo spectrometer. Previously a mechanical switch was used for the purpose. The electrical switch is synced to the pulse sequence, streamlining the acquisition process. Multi-channel receive arrays provide crucial image encoding because each coil is preferentially sensitive to signals in its spatial vicinity. When nonlinear gradients are used for spatial encoding, local coil encoding permits unwrapping of image voxels that have the same frequency isocontour, a problem not encountered in conventional Cartesian imaging with linear gradients.

In the 8-channel receive array, coupling to the transmit coil was not previously an issue because the receive coils were untuned. To obtain better sensitivity, the coils were changed to resonant RF circuits during Q4Y2 (Figure 17). PIN diodes were used to create a parallel LC trap circuit at the input to each receive



coil during RF transmission to prevent coupling between the receive coils and the transmit solenoid [12]. Conversely, the transmit coil is disabled with a reverse-biased PIN diode during signal readout.



Figure 17: RF subsystem includes (**left**) multiplexing 8-to-1 switch with a bank of 8 pre-amplifiers, (**center**) 8-channel array of receiver loops, and (**right**) solenoid transmit coil for producing a uniform  $B_1$  field.

### Halbach array LFI: RF transmit pulses

The novelty of the Halbach imager is its use of a permanent inhomogeneous  $B_0$  field to perform spatial encoding. One drawback of this approach is that the encoding field is intrinsic and may not be switched off during RF transmission. When a rectangular “hard” pulse envelope is transmitted, the spin flip angle and phase are a function of the off-resonance frequency. The shortest pulses that we can achieve with our 250 W Tomco RF power amplifier for the  $90^\circ$  and  $180^\circ$  pulses are 50 ms and 100 ms, respectively, corresponding to a Rabi frequency of 10 KHz. Because our off-resonance frequency approaches (and may even exceed) the Rabi frequency in many regions of the object, particularly near the periphery, the flip angle and phase vary dramatically within the field-of-view. This causes signal loss near the periphery and applies a different phase distribution from the one that is assumed in the forward model. The most straightforward solution to this problem is to transmit shorter, higher power RF pulses, increasing the Rabi frequency with respect to the off-resonance frequencies. This requires much more careful handling of the transmit RF coil design to avoid arcing and other complications of high-power operation.

The other source of systematic error in our experiments is off-resonance effects during RF excitation. In conventional MRI, the primary source of frequency dispersion among spins during RF excitation is the linear gradient field. The bandwidth of the RF pulse is set to excite a slice or slab or a desired thickness. For non-selective “hard” pulses, no linear gradient is played and the only frequency dispersion is that which remains after  $B_0$  shimming procedures have been performed. Typically this inhomogeneity is on the order of a few hundred Hz.

In the Halbach encoding scheme, the strongly varying inhomogeneous field shown above in Figure 11 is always on, even during spin excitation and refocusing pulses. This changes the effective flip angle as well as the spin phase distribution as a function of the off-resonance frequency. For phase sensitive image reconstruction such as the iterative matrix inversion used in our experiment, phase errors can be deleterious to the resulting image. To counter this effect, we explored ways to reduce the length of our hard pulses used for excitation and refocusing in order to make the pulses intrinsically more broadband. We doubled the transmit coil Q to increase its efficiency, and upgraded our RF transmit amplifier from 250 W to 1 kW, bringing a factor of two reduction in the achievable pulse lengths.



The benefit of the more powerful amplifier is shown in Figure 18, where Bloch simulations of the spin ensemble after the RF pulses in spin-echo imaging sequence (just prior to readout) is shown. The flip angle and spin phase are much more uniform within the field of view when the more powerful amplifier is used. To take advantage of the higher power available from the 1 kW amplifier, we rebuilt our transmit solenoid coil using high-voltage tuning- and matching capacitors.

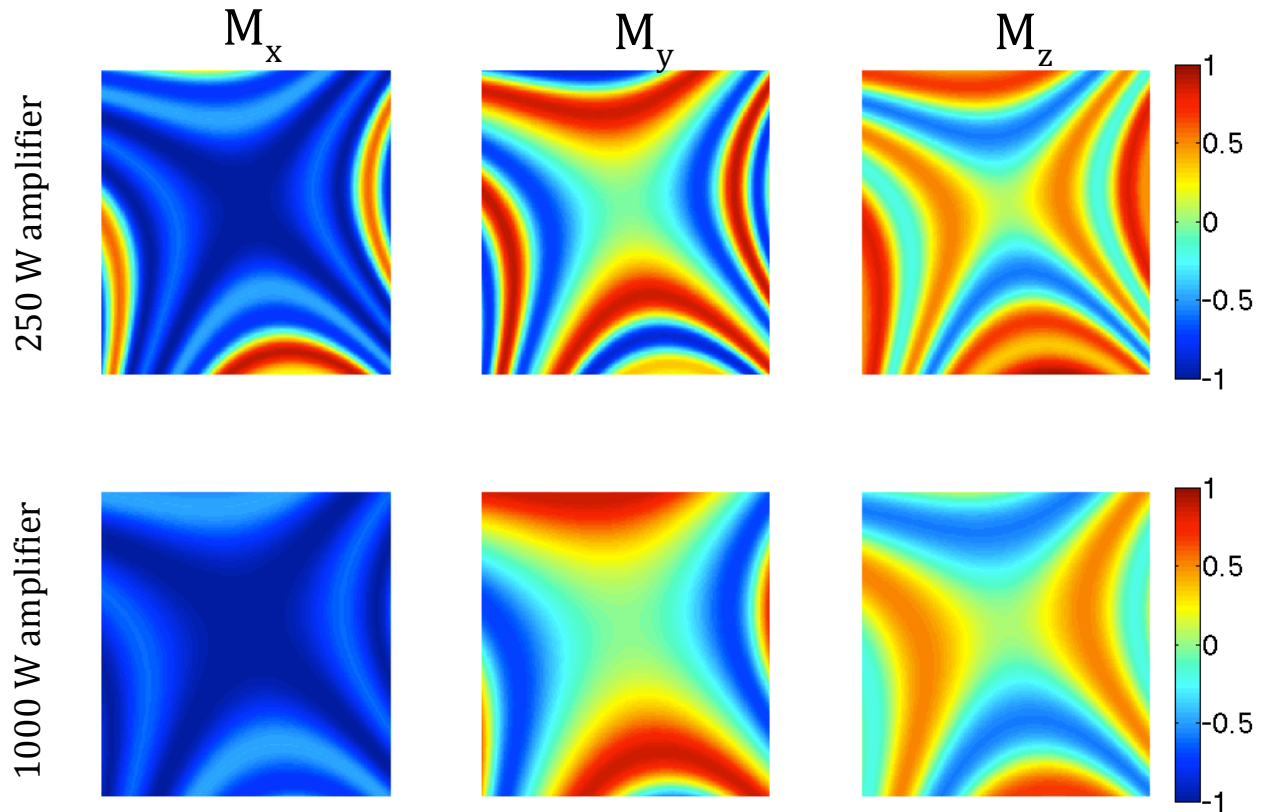


Figure 18: Phase evolution across the 8-cm field of view following spin echo excitation and refocusing with hard pulses (just before readout). Switching from a 250 W to 1000 W amplifier allows us to shorten the excitation ( $90^\circ$ ) pulse from 40 ms to 20 ms and the refocusing ( $180^\circ$ ) pulse from 80 ms to 40 ms.

Unfortunately, some residual off-resonance effects are evident in the figure even when 1 kW of transmit power is used. A novel idea is to redesign the RF pulses so that they excite both on-resonance and off-resonance spins. Traditional composite pulses [13] increase the range of frequencies over which a desired flip angle is achieved, but they still alter the spin phase in proportion to the off-resonance frequency. For our full-encoding matrix image reconstruction, this phase needs to be known accurately.

A better approach is to design a tailored RF pulse that applies a flat phase distribution across the object [14]. Our spectrometer has full amplitude and phase control on a very fine timescale (less than one microsecond), making such a custom pulse a possibility, and the control computer for the Apollo console was updated and the control software migrated from NTNMR to the latest version of TNMR, allowing pulse sequences to be shared between the Halbach scanner and the electromagnet LFI scanner test bed. To further mitigate this effect and achieve a truly uniform spin phase distribution after the refocusing pulse, we



are presently designing  $90^\circ$  composite pulses that are optimized to produce uniform phase everywhere in the object using the small tip angle approximation to increase the pulse length while *reducing* the effective bandwidth. In the optimization problem, the pulse waveform is constrained to provide a uniform flip angle and phase across the object. While this approach is less effective for  $180^\circ$  pulse design, we are exploring other possibilities for improving the  $180^\circ$  refocusing pulse, including an optimization on the full Bloch simulation of the pulse waveform to enforce uniform phase and flip angle. While such an approach is more computationally demanding, it is more accurate than the low tip angle approximation.

## Halbach array LFI: 1D projections & 2D imaging

Improvements in calibration methodology now permit the imaging of two-dimensional test phantoms positioned at the axial isocenter of the Halbach array. Temporal drift of the magnetic field was monitored with NMR probes and incorporated into the appropriate rows of the encoding matrix. As the Halbach magnet is rotated around the sample, different views are acquired along curvilinear isocontours. Time-domain reconstruction is performed using the algebraic reconstruction technique (ART), which cycles through the encoding matrix one row at a time, back-projecting the data point corresponding to each row [8]. Because reconstruction relies on accurate knowledge of each isocontour's location in space, field drift must be compensated when the encoding matrix is calculated.

We made a simple phantom with 2-cm diameter balls of water placed at the center and at 6-cm from the center (Figure 19, **left**) to explore NMR-based projection-encoding in our nonlinear field. Two surface coils in quadrature were used for RF reception, with one coil placed in the vicinity of each peripheral ball. When the resulting data is Fourier transformed, nonlinear projections of the balls are obtained in the frequency domain. As shown in Figure 19 (**right**), the peak from the center ball is much narrower than those from the peripheral balls, as expected from the much sharper variation of the encoding field away from the center of the magnet.

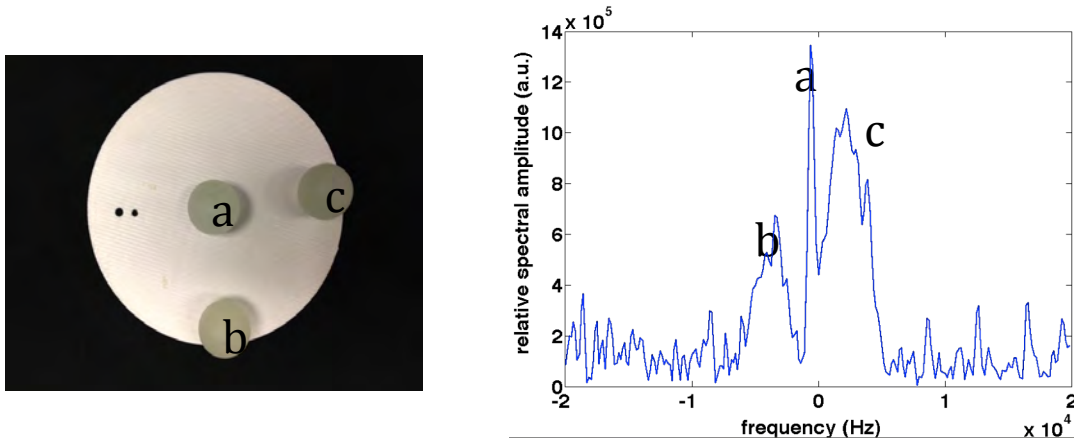


Figure 19: Calibration phantom (**left**) consisting of three 2-cm balls (at isocenter or at a radius of 6 cm) is used to obtain NMR projections (**right**) in the magnet's nonlinear encoding field. As expected, the balls at the periphery show greater frequency dispersion since the field varies roughly quadratically with radius from the center



To evaluate two-dimensional imaging performance, generalized projections of a two-ball phantom were made over several rotation angles between  $0^\circ$  and  $90^\circ$  (Figure 20). At each angle, the object is projected along the curvilinear frequency isocontours of the approximately quadrupolar encoding field.

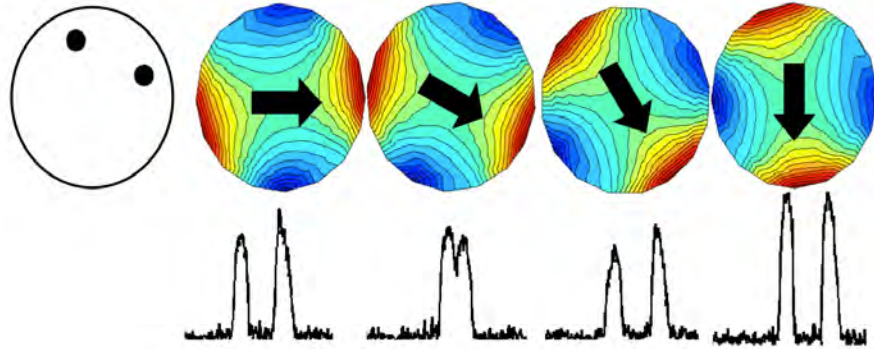


Figure 20: **(left)** Schematic of imaging phantom. **(right)** Six representative encoding field rotations and experimental projections of phantom on left (single coil, 128 averages, SNR~30). Arrow is B0 direction.

Common to all higher-order gradient encoding methods is the problem of aliasing due to redundant frequency contours, which can be resolved using additional spatial encoding from local RF receive coils [7]. Another issue is the flatness of higher-order fields at the center of the FOV, where encoding can only be achieved through the addition of linear or odd-spatial order fields [8]. We build on previous encoding methods by assessing the encoding of a single rotating field, with and without parallel imaging and a spatial offset between the axis of rotation and the axis of field symmetry.

A spin echo sequence with TR/TE=200 ms/9.4 ms and a 40 kHz bandwidth was used to acquire projection data. The resulting images of the Gd-doped two-ball phantom (Figure 21a) show the expected pattern of aliasing through the isocenter when a single receive coil is used (Figure 21 b,f,g). When multiple coils are used (Figure 21 c-d), the ghosts disappear. Streaking artifacts occur due to the undersampling of the dataset, as with conventional radial imaging using linear gradients. When more projections are acquired (Figure 21a) the streaking artifacts diminish, as evident in the background of (Figure 21b), which was acquired with more projections than the other data shown.

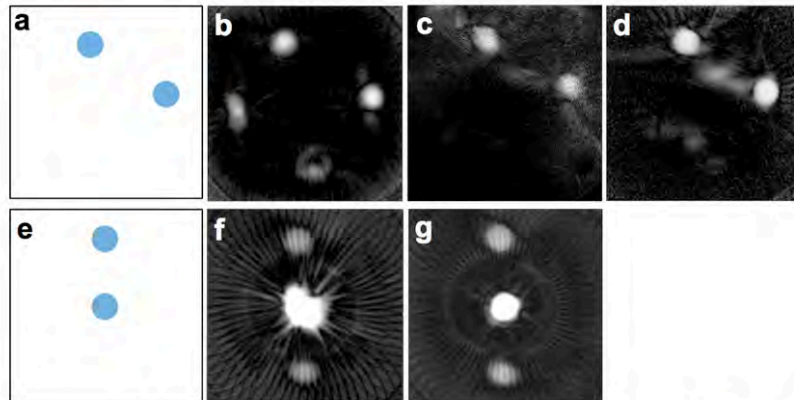


Figure 21: **(a)** Ball locations in ground truth phantom 1, **(b)** 80 projections of phantom 1 using a single solenoid receive coil **(c)** 24 projections of phantom 1 using 4 receive coils, **(d)** simulated version of **c**, **(e)** ground truth phantom 2, **(f)** 35 projections of phantom 2 using one coil, **(g)** simulated version of **f**. FOV is 16 cm.



## Halbach array LFI: encoding & reconstruction simulations

We simulate the encoding/reconstruction to examine the effect of breaking the encoding field symmetry by shifting it off-center using a linear component (2000 Hz/cm or 3000 Hz/cm). We further simulate the ability of the encircling array of 8 local RF receive coils to remove aliasing.

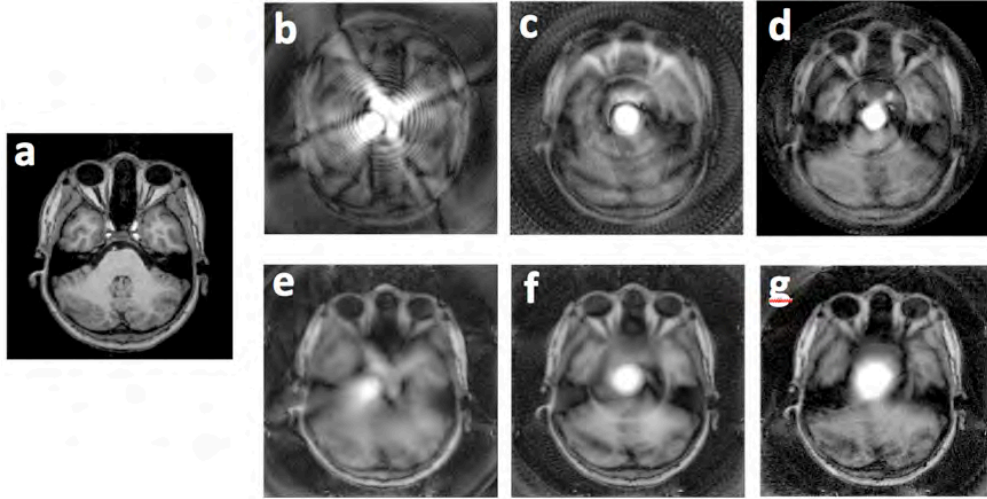


Figure 22: Simulated  $256 \times 256$  reconstructions of reference brain image (a), encoded using 128 projections with no field offset (b), 2000 Hz/cm offset (c), and 3000 Hz/cm (d) with no RF coil encoding. The offset removes much of the aliasing associated with the symmetry of the multipolar fields and recovers some resolution near the center. The addition of eight receive coils in each case (e-g) further improves resolution and removes aliasing, though resolution remains better near the periphery. Simulated FOV is 28 cm.

Even with the non-ideal encoding fields used here, much of the detail in the object is retained in the reconstructions (Figure 22). As expected, a linear offset recovers some resolution, though some detail is still lost at the very center. Consistent with previously published work (and with our experimental data), surface coils are shown to be an effective way to reduce aliasing artifacts and also to improve resolution, particularly when no field offset is used.

## Halbach array LFI: future work

Simulations above suggest that performance gains are possible by breaking the symmetry of fields using a linear field to offset the quadrupolar Halbach field. Such a field could be achieved in future experiments by placing small permanent magnets at fixed locations around the Halbach array. We plan to compare the imaging performance of centered and offset quadrupolar Halbach fields.

We will begin to generalize the imaging approach to three dimensions, possibly through curvilinear slice selection [15]. An alternative approach is to phase-encode the through-plane direction using a transmit coil with linearly-varying phase along the axis of the Halbach [10].

Image reconstruction with a “total generalized variation” prior [16] will also be explored as a way to suppress streaking artifacts for highly undersampled data.



Opportunities exist to speed up the image reconstruction process by Fourier transforming the encoding matrix into a domain where most of the coefficients are small and can be zeroed out [17]. In this way, reconstruction times may be decreased by a factor of 10 or more with minimal (almost imperceptible) blurring of the image.

Finally, the SNR efficiency of the Halbach imaging pulse sequence will be increased using an echo train to acquire, and then average, multiple readouts per TR.

### Parallel-array detectors for the electromagnet LFI

We continue to work to understand the limits of acceleration that are possible with low-field MRI including implementation of parallel imaging with array coils. At conventional high-field MRI scanner operational frequencies, “body noise” dominates inductive copper loop detection, resulting in strongly correlated noise on each receive coil in the parallel array. At low field, uncorrelated Johnson noise dominates, which proves a benefit to parallel imaging and accelerated imaging using SENSitivity Encoding (SENSE). We have demonstrated the first 8-channel parallel imaging and acceleration obtained in this new Johnson-noise dominated regime [18], and attach this abstract as an Appendix.

### Parallel-array detectors: receive coil development

NMR parallel imaging at low frequency is a new regime and the optimal receive coil parameters are unknown from the literature. Based on our measurements in Y2 Q1, we elected to build our 8-channel array using 24 gauge copper wire using 30-turn coils with an inner diameter of 8 cm. When laid out flat with coil center points aligned, optimal geometric decoupling between neighboring coils was found to occur at 1.6 cm of overlap.

For simplicity, our first phased array coil was built on a cylindrical form with the 8 coils individual elements forming a ring. Including the proper 1.6 cm overlap as described above, this results a circle with an inner diameter of 15.6 cm. The design for the coil former was created in a 3D CAD program (Google Sketchup) (Figure 23) and printed on a 3D printer (Dimension SST 1200es) in polycarbonate.

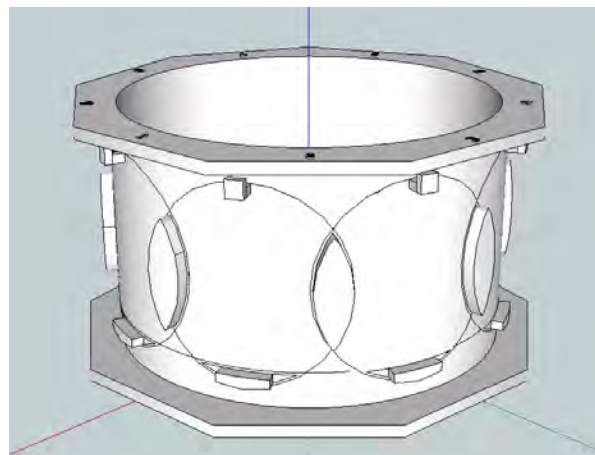


Figure 23: Final design of 8-channel phased array coil former



The individual elements of this coil each required their own tuning and matching circuit board, which was designed and produced on our circuit board router. Each coil element was placed on the 3D form and tuned/matched to 276 kHz with at least  $-20$  dB return loss (Table 1). The coupling between all coils was measured and recorded in (Table 2) A photograph of the complete 8-channel receive array coil is shown in Figure 24

Coil	Freq (kHz)	dB	Coil	Freq (kHz)	dB
1	276.5	-33	5	276.5	-45
2	276.75	-36	6	276.25	-50
3	276.75	-39	7	276.5	-37
4	276.25	-45	8	276.25	-35

Table 1: Tuning frequency (in kHz) and attenuation (in dB) for 8 receive coils in parallel array coil

Coil	1	2	3	4	5	6	7	8
1	-	-40	-	-	-	-	-	-
2	-41	-	-41	-	-	-	-	-
3	-11	-41	-	-38	-	-	-	-
4	-17	-11	-38	-	-39	-	-	-
5	-19	-17	-11	-40	-	-41	-	-
6	-17	-19	-17	-11	-41	-	-39	-
7	-13	-19	-19	-19	-13	-40	-	-40
8	-41	-11	-17	-19	-17	-11	-40	-

Table 2: Measured coupling (in dB) between coils in the 8-channel receive array coil



Figure 24: The final eight-channel array coil (left) and the tune/match electronics stack (right).



## Parallel-array detectors: data processing and OLE automation

### *Update existing data processing tools*

While the TNMR software that runs the Tecmag Redstone console has the ability to process data, doing so ties up console computer and prevents data acquisition. Instead, the data is taken off the console computer and analyzed by researchers on individual computers. Because most processing is done in MATLAB, our laboratory has developed and maintains a library of scripts and functions capable of taking the raw binary data file from TNMR and converting them to  $k$ -space and image-space figures. However, these files were all developed for single-channel data. When acquiring from eight channels, TNMR interleaves the data into two groups and then concatenates the data into a single data stream. The data must first be deinterlaced and redimensioned before Fourier transformation is performed and the image reconstructed. All data processing functions were therefore rewritten and expanded to load an entire raw TNMR binary file (containing acquired data as well as sequence timing and acquisition parameters) and auto-detect the number of channels acquired and slices as well as the number of phase encode and readout steps. The rewritten script now returns to the user a matrix properly dimensioned and ready for display, simplifying and streamlining the steps needed for viewing an image for both single and multi-channel data sets. This is a major workflow improvement for our laboratory and is essential for multi-channel data.

### *Improve data flow via OLE automation*

Field of view (FOV) is set in our MRI sequences by adjusting gradient strengths and step sizes in phase encoding tables. However, the Redstone console running TNMR is a general purpose instrument and as such requires a complex multi-step process to set FOV, requiring gradient table values to be computed first in MATLAB and then copied into the TNMR program. This approach is vulnerable to error through both miscalculation and operator oversight. At the least, it proved time consuming, particularly when generated the sophisticated phase encode tables used in under-sampling sequences.

TNMR supports OLE automation, a process whereby one application is controlled by another, and MATLAB is capable of automation. A MATLAB script was written that would take the computed gradient table values for a given number of slices, phase encode steps and under-sampling ratio and write them directly to their corresponding variables in TNMR. This improvement increases the speed at which adjustments can be made while scanning and decreases the risk of operator error in setting the FOV.

### *Develop image reconstruction tools for multi-channel data*

All previous work in our lab has used only a single receive channel. All tools developed for visualization were developed assuming single channel acquisition. However, N-channel coils will produce N images that must then be combined into a single image. While algorithms for doing this have existed for years, a function for doing so with our data had not yet been developed. We therefore wrote code that will combine the images using a sum of squares approach (Eq 1),

$$(Eq. 1) \quad P = \sqrt{P^T R^{-1} P^*}$$



where  $P$  is the resulting pixel intensity and  $p$  is a vector of the pixels from each coil [11].  $R$  is the noise resistance matrix in general, but for this preliminary data we assume it to be the identity matrix.

## Parallel-array detectors: 8 channel image acquisition and reconstruction

### *Acquire and successfully reconstruct a multi-channel image*

We first tested the parallel imaging coil by collecting FIDs using the b-SSFP sequence developed previously and modified for eight-channel acquisition. For this setup, the parallel imaging coil was centered inside of a 25 cm solenoid tuned transmit coil, with a 15 cm diameter cylindrical CuSO<sub>4</sub>-doped water phantom (Figure 25). The orientation shown resulted in the lowest coupling between the transmit and receive coils.



Figure 25: Test setup of 8 channel parallel imaging coil and phantom inside a 25 cm transmit coil in the 6.5 mT electromagnet LFI. The pale blue color is the CuSO<sub>4</sub>-doped water phantom.

Using a pulse width of 100  $\mu$ s and frequency of 276 kHz, we collected an FID from a single channel (Figure 26 **left**). We then collected FIDs from all eight channels (Figure 26 **right**, sorted in Figure 27) and verified that all 8 channels were receiving signal. Some fluctuation in signal between individual channels is expected due to the varying angle between each coil and the main magnetic field, as well as to small differences in the inductance, decoupling, tuning and matching of each coil.

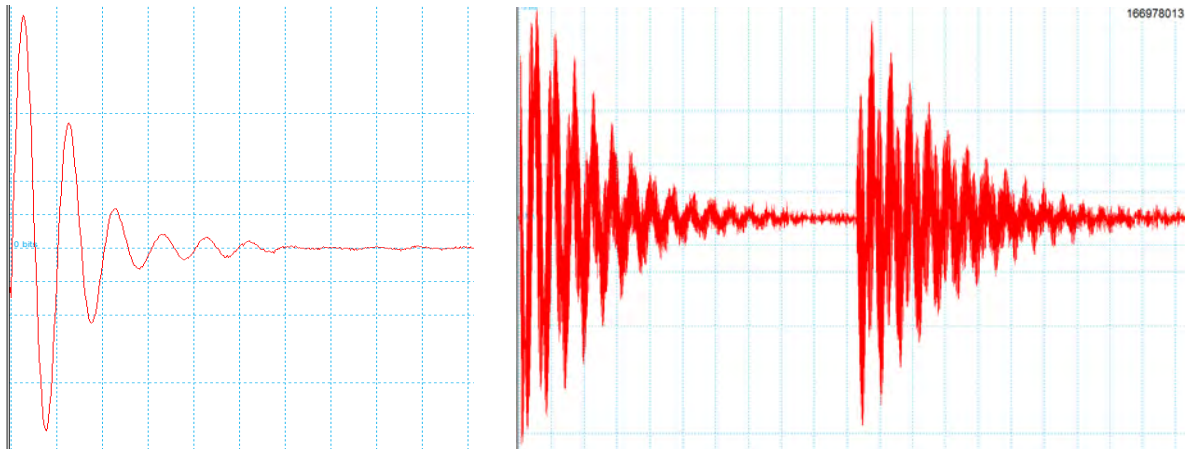


Figure 26: (L) FID acquired from a single coil (channel 1) of an eight-channel phased array at 6.5 mT (276 kHz.) (R) Interleaved and concatenated FIDs acquired simultaneously from all eight elements of the phased array at 6.5 mT (276 kHz).



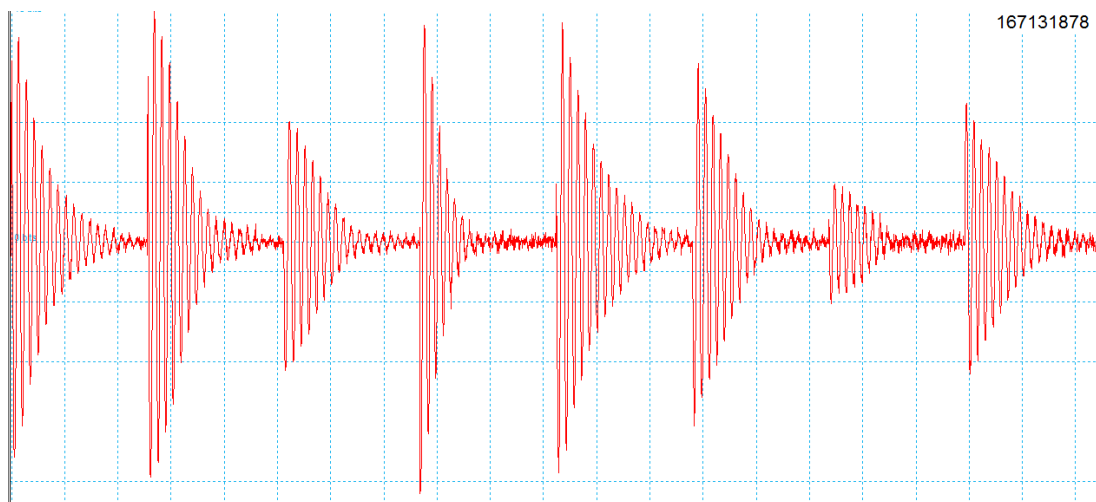


Figure 27: Eight simultaneous FIDs from the experiment of Figure 26, deinterlaced and sorted.

In order to test the ability of the parallel array to acquire images in the electromagnet LFI, we acquired an image of a homogenous doped-water phantom from each channel simultaneously. A typical single channel image (channel 1) is shown in Figure 28 (**left**). The geometric location of channel 1 is revealed in the single channel image reconstruction. As anticipated, the NMR signal is strongest closest to the coil and drops off as the distance from the sample to the coil increases. Image data from all eight coils was combined into a single reconstructed image using a sum of square approach (Figure 28 **right**). This result represents the very first parallel MRI acquired at low field, in the frequency regime known as the Johnson noise-dominated regime. Using a more optimized 3D b-SSFP imaging sequence and using a  $\text{CuSO}_4$  phantom with a 3D-printed MGH/MIT logo inside, we acquired and reconstructed the eight-channel image shown in Figure 29. These images represent the first parallel imaging results ever obtained in the low field Johnson-noise-dominated regime.

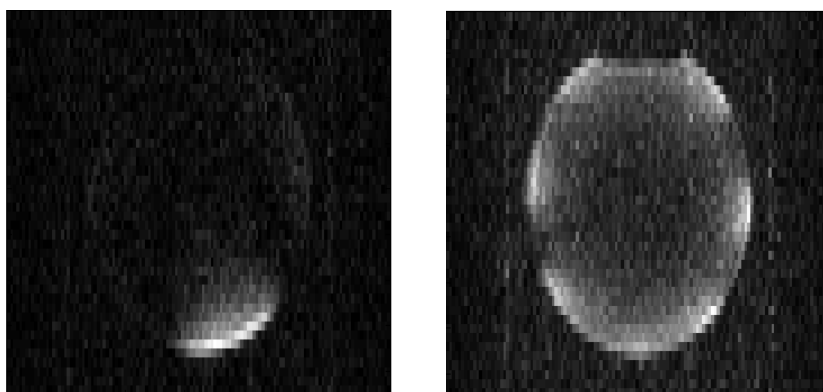


Figure 28: (**left**) MRI image of homogenous phantom reconstructed using a single channel (channel 1) of the eight-channel parallel imaging coil. (**right**) MRI image reconstructed using a sum-of-squares of all eight channels. Both images acquired with 3D b-SSFP, NA 20, TE/TR=35 ms/56 ms, acquisition matrix:  $128 \times 42 \times 24$ , voxel size:  $3 \times 4.5 \times 7 \text{ mm}^3$ . Total acquisition time = 18.8 min.





Figure 29: First image of structured phantom reconstructed from an eight-channel simultaneous acquisition in the 6.5 mT LFI with 3D b-SSFP, NA 100, TE/TR=18 ms/36 ms, acquisition matrix: 128x60x5, voxel size: 2x3x7 mm<sup>3</sup>. Total acquisition time = 18 min.

#### *Decoupling strategies for receive array and transmit coil*

NMR receive coils are oriented optimally when they are orthogonal to  $B_0$ . In this orientation, precessing transverse magnetization generated by RF pulses punches flux orthogonally through each coil loop, generating the maximum inductive NMR signal. However, depending on the experimental geometry, the transmit coil can also generate flux through the resonant detection coils. When this occurs, the Tx coil will inductively couple to the Rx coils, and in this case the presence of the tuned Rx coil elements affect the RF profile. Preliminary attempts to image using the eight channel array coil in the preferred orientation (*ie*, Rx array in the  $xy$  plane) resulted in unacceptable coupling between the array and the transmit coil and adversely affected the quality of the images collected. Because the coupling decreased with the array in the  $yz$  plane (Figure 30), all parallel images above were all acquired with the array in this non-optimal (from a signal perspective) orientation where Tx and Rx are essentially decoupled.

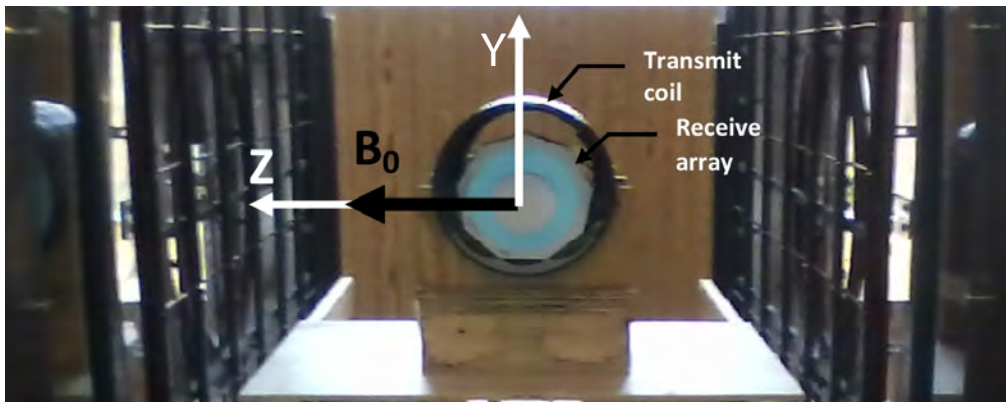


Figure 30: Orientation of eight channel array in the  $yz$  plane inside the electromagnet LFI.

Image data acquired with the array in this  $yz$  orientation (Figure 30) showed good signal from the coils on the top and bottom of the array (*ie*. Rx coils orthogonal to  $B_0$ ) but reduced signal from coils on the left and right sides of the array (*ie*. Rx coils parallel to  $B_0$ ). While the reconstructed images have better SNR in



this orientation, approximately half the coils are performing below their capability due to poor signal along the  $z$ -axis. In the interest of maximizing signal in all the array coils, it was imperative to resolve the inductive coupling between transmit and receive coils.

A decoupling solution would need to detune the receive coils when transmitting and likewise detune the transmit coil while receiving. The usual solution for the high-field MRI relies on PIN diodes, however no PIN diodes exist that have carrier lifetimes long enough for operation at our frequency of 276 kHz. A passive solution was decided upon because it could be quickly implemented with minimal modification to the array and hardware and required no extra cables or circuitry. It consisted of placing high-speed silicon crossed-diodes (BAV99) in series with the transmit coil and in parallel with each receive coil. A schematic is shown in Figure 31.

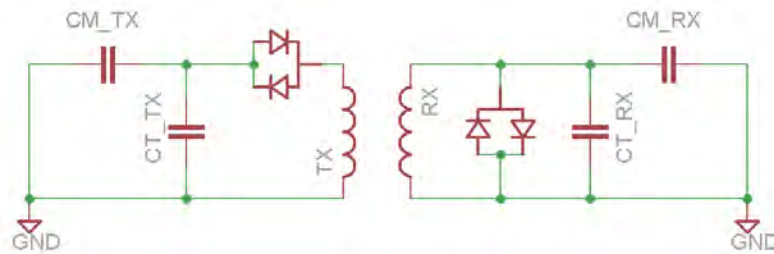


Figure 31: Schematic of the passive decoupling scheme used for parallel imaging at low frequency. The transmit (TX) coil resonator and a single receive (RX) coil resonator element are shown in a parallel-tune (CT)/series-match (CM) circuit.

The crossed-diodes in the transmit circuit allow the transmit pulse to reach the transmit coil when the pulse voltage is greater than the bias voltage (nom.  $0.7 V_{DC}$ ), a condition easily met during RF transmit. When receiving, however, the voltage induced in the Tx coil from precessing magnetization is too small to forward bias the crossed diodes, and the Tx coil remains decoupled during receive. On the receive coil, the crossed-diodes short to ground any induced voltage greater than the bias voltage, a condition that may be met during transmit. This decouples Rx during transmit. This very simple passive crossed-diode decoupling scheme greatly reduces coupling, and enables signal acquisition with the array coil played in the more efficient  $xy$  plane. Greatly improved raw images collected with this new decoupling scheme are shown in Figure 32, and reconstructed images are shown in Figure 33.



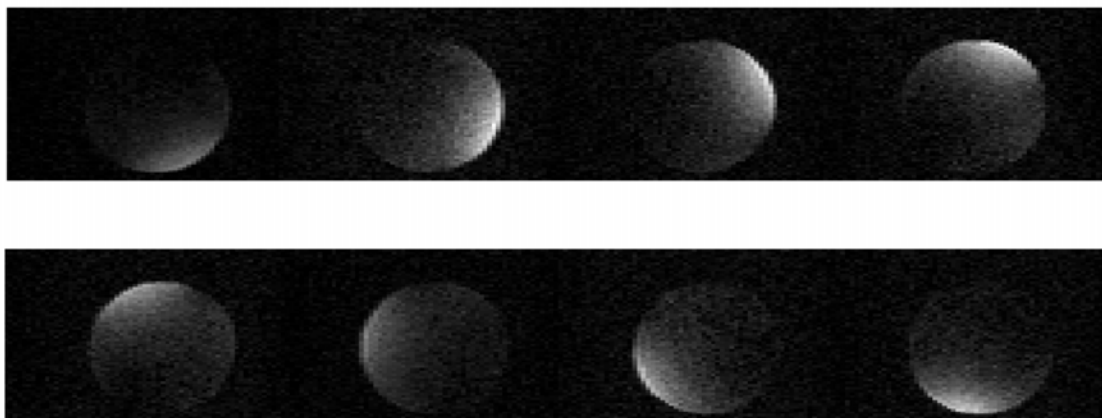


Figure 32: Raw images acquired from individual elements of the eight-channel receive array, used to reconstruct the final image shown in Figure 33C.

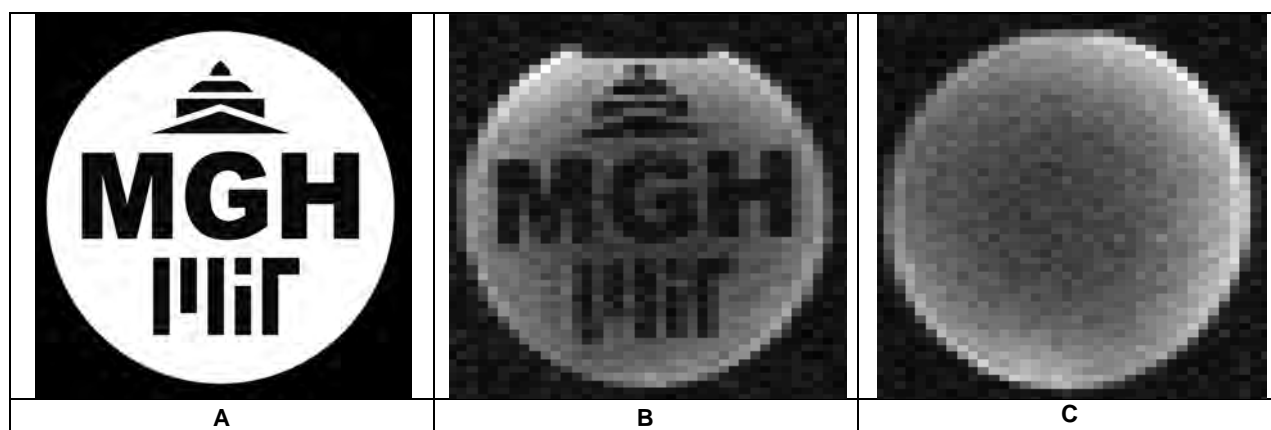


Figure 33: Schematic of the water-filled structured phantom (A), reconstruction of structured phantom (NA=200, B) and reconstruction of a homogeneous phantom (NA=200, C). These improved images are the consequence of the Tx/Rx decoupling strategy described above. Receive array was oriented in the  $xy$  plane.

#### *Development of multi-channel data processing user interface*

Previous work in developing data processing tools for multi-channel acquisitions has been expanded to a master data processing interface that would allow each investigator in our lab to customize the data processing to meet their needs without requiring modification of the underlying code. A graphical user interface has been developed and is currently under evaluation (Figure 34).



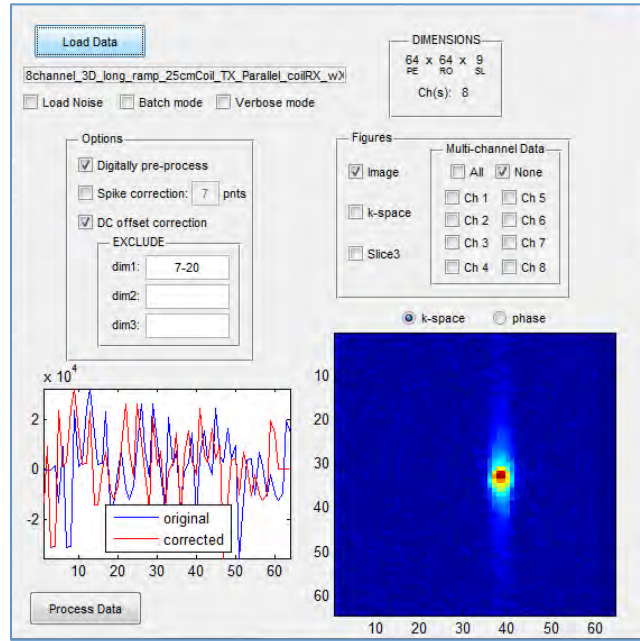


Figure 34: Screenshot of the graphical user interface for processing acquired multi-channel data. The user selects various processing options (**middle left**) and the figures to display (**middle right**). Images at the bottom of the GUI include a representative readout (**bottom left**) and display either  $k$ -space or phase for a single channel/slice (**bottom right**). Changes made in options are reflected immediately in the images. Once all settings are as desired, the “Process Data” button generates the Fourier transformed data and figures.

This graphical interface provides basic information about the data (name, size) and provides several processing options as well as image output choices. Once a data file is loaded, a representative readout acquisition is displayed as well as an image of the  $k$ -space or phase for a single channel (user selectable). As different processing options are turned on or off the plots are immediately updated, and the “Process Data” button will produce the selected figures. For multi-channel data, the user can also choose display image data from individual channels (e.g. Figure 32). As future work improves processing and output options, this graphical data processing interface reduces the risk of errors appearing in the code while still providing all investigators the flexibility needed in processing their data. As a side benefit, the interface offers those with limited knowledge of MATLAB a simpler and more intuitive method for data processing and visualization.

#### *Development of image reconstruction tools for accelerated parallel acquisition data*

The use of multi-channel receive arrays partially oversample each voxel. As a result, it is possible to implement undersampling techniques which shorten scan times while maintaining comparable quality in reconstructed images. At high magnetic field strengths, so-called “body noise” dominates, resulting in strongly correlated noise between each receive element in the parallel array. At the low frequency that the electromagnet LFI operates (276 kHz), uncorrelated Johnson noise dominates, providing a benefit to parallel imaging and accelerated imaging using SENSE as described in the next section.

It was necessary to develop additional reconstruction tools in order to reconstruct undersampled (*i.e.* reduced by the reduction factor  $R$ ) SENSE data. Undersampling lines of  $k$ -space results in aliased or folded



images, and unaliasing the image requires solving a set of over-determined linear equations. MATLAB routines for this have been developed previously at the MGH/Martinos Center and are available online<sup>1</sup>. This code was modified so it could be included seamlessly with our previously developed multi-channel reconstruction tools.

### *Implementation of image acceleration via SENSE*

The negligible noise correlation between channels at low-field benefits the implementation of SENSE. As a feasibility study, 1D SENSE reconstruction (reduction factor  $R=2$ ) was simulated on the middle slice of the fully sampled image. The noise covariance matrix and coil sensitivity maps were estimated from the data. The corresponding experiment ( $R=2$ ) was performed from a structured phantom. Noise data were acquired using a b-SSFP sequence with RF transmit blanked (total acquisition = 704 s). Sensitivity maps were estimated from the fully sampled data set acquired previously using third-order polynomial smoothing. Aliased images were unfolded using the reconstruction code described above (Figure 35 and Figure 36).

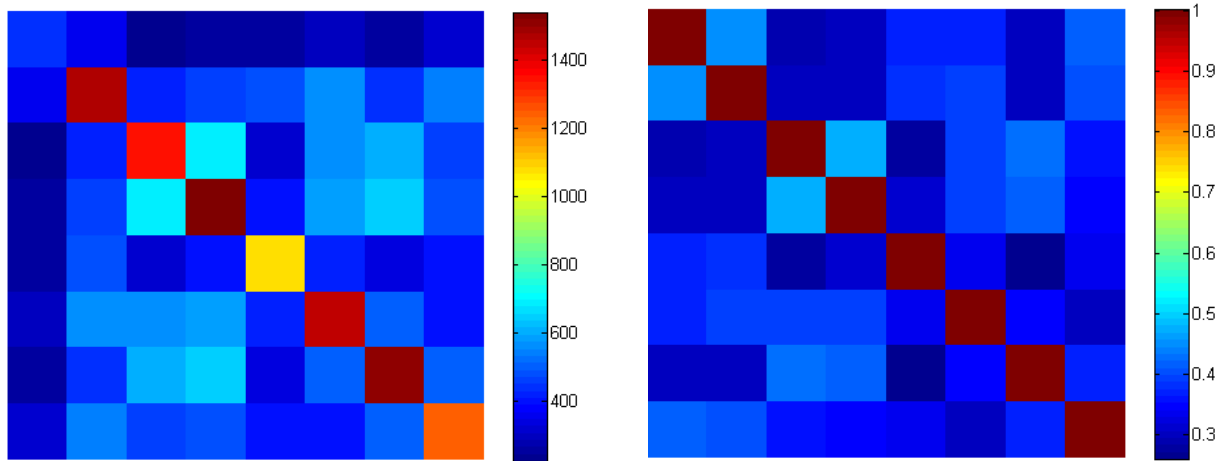


Figure 35: **(left)** Noise covariance matrix for the eight-channel parallel array coil oriented in the  $xy$  plane. The maximum value is approximately half the maximum value of when the array is placed in the  $yz$  plane. **(right)** Correlation coefficient matrix for the eight-channel parallel array coil oriented in the  $xy$  plane. The matrix is essentially the identity matrix, an indication that imaging at low field is Johnson noise dominated. These measurements were made before passive decoupling was implemented, hence the difference between the two Rx array orientations.

<sup>1</sup> Available at <http://www.nmr.mgh.harvard.edu/~fhlin/>



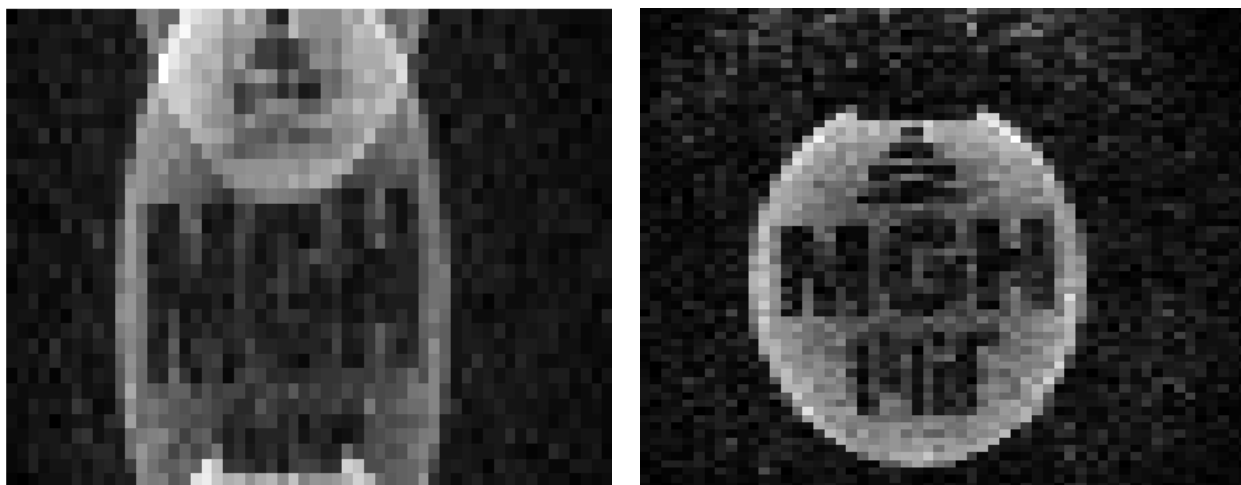


Figure 36: **(left)** SENSE acquisition using the eight-channel parallel imaging coil with a reduction factor  $R=2$ , results in an aliased image. **(right)** MRI image reconstructed using SENSE reconstruction algorithms. Both images acquired with 3D bSSFP at 6.5 mT, NA 200, acquisition matrix : **(left)** 32x64x5, **(right)** 64x64x5.

The results shown here are first inductively-detected SENSE reduction images attained in the Johnson noise dominated regime. Development of parallel imaging and SENSE acceleration are important steps toward human imaging at very-low field. Future work will optimize the sequence to further improve image quality. Additional array designs will be tested and SENSE combined with random undersampling strategies will be investigated. We are encouraged by the image improvement attainable with our passive decoupling scheme, and this will improve future SENSE acceleration as well.

## TASK 1B: System control and image acquisition

Integration of Tecmag Redstone console with the hardware of Task 1A:

In Y1, we worked with Tecmag Inc. to design and deliver the final design specification of the multi-channel enhanced MRI console upgrade for the LFI known as Redstone. This highly customized Redstone console is used for RF and gradient pulse control and signal reception for the electromagnet LFI. It contains the same capabilities of RF and gradient pulse control and signal reception as a clinical MRI scanner, while maintaining much greater flexibility and operator control for MR sequence development. The Redstone console enables high-speed parallel imaging (including eight low-frequency receive channels) at the unusual frequency regime of low-field MRI. It also contains two additional channels: a high-frequency transmit channel and a high-frequency receive channel. The addition of these channels to the Redstone offers the rather unique capability of performing simultaneous NMR/ESR in the LFI, unifying the effort of Specific Aim 1 and the effort of Specific Aim 2, particularly critical for us in Y2 and in Y3. In Y2, we continued to work with Tecmag development engineers to improve the performance of this Redstone console. A 5-bit (0–31 dB) digital attenuator was added allowing us to manage the enormous dynamic range difference between conventional  $^1\text{H}$  MRI and Overhauser-enhanced experiments from within sequence control. Tecmag has also been developing the 4<sup>th</sup> generation NMR receiver board (“RX4”) and we have tested a single channel prototype. This new receiver board has a much more linear gain over its 50 dB range and,



especially at low-gain, we have measured improved SNR by at least a factor of 4. We expect an in-field upgrade for the remaining receiver boards to the new RX4 boards early in Y3.

## Begin development of image navigation and reconstruction methods:

In Y1, we developed a bidirectional control and processing pipeline between TNMR and MATLAB. This pipeline allows us to seamlessly move data between the acquisition computer and the processing scripts. The bidirectional pipeline allows MATLAB to directly control the TNMR pulse language and this control the Tecmag Redstone directly. During Y2, we added additional functionality—spectroscopy processing and single and multi-channel image reconstruction—by developing suites of MATLAB packages. The Tecmag software that runs our Redstone console, TNMR, offers great flexibility in the design and implementation of designing and implementing new pulse sequences and is crucially enhanced by these software packages as the work being developed in our laboratory such as bSSFP-based OMRI is not a standard MRI technique. The parallel imaging reconstruction suite was described above in section *Data processing and OLE automation* (p. 26ff). Below we detail the development of the NMR spectroscopy suite.

### *NMR data processing suite*

We have greatly increased our efficiency in the processing and analysis of NMR data acquired in the LFI with a more complete NMR data processing user interface written in MATLAB. An example of one the user interface panels is shown in Figure 37. The NMR suite loads a TNMR data file and allows the user do many of the most common data processing techniques much more quickly than in TNMR. The two most important improvements of this custom software compared to TNMR are: 1) raw data is always readily available so the user can quickly revert back and apply different processing parameters should the initial parameters prove unsatisfactory. The user can quickly flip between looking the raw data, Fourier transform, phase, peak amplitudes, and integral values. In TNMR, the raw data and processed data reside in separate files, meaning the raw data must be reloaded whenever a change is to be made. 2) MATLAB has much more robust curve fitting routines and more easily allows the user to create custom equations than in TNMR. This last feature is very important as the optimal parameters for b-SSFP depend on the ratio of the  $T_2$  and  $T_1$  relaxation times and requires an accurate pulse calibration.



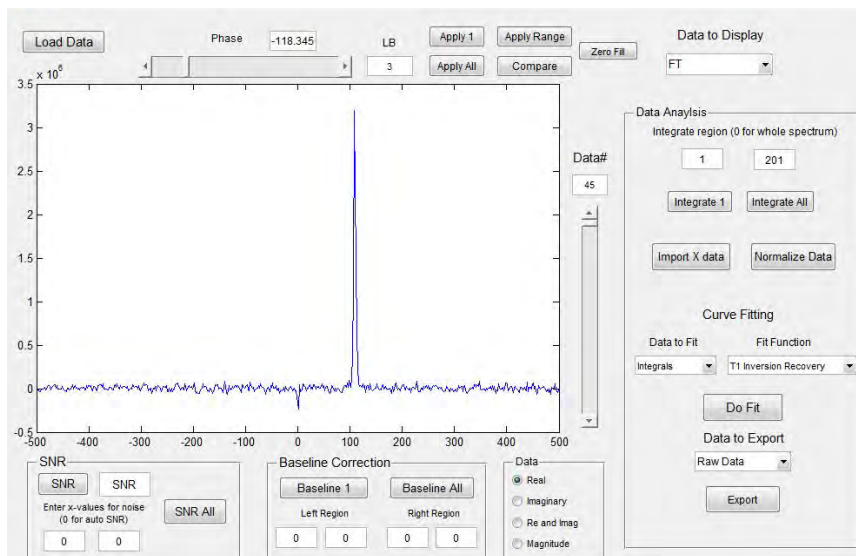


Figure 37: Typical screen shot of the in-house developed NMR data processing suite. The user interface allows us to process data for our most common NMR experiments more quickly than the TNMR software that runs the Tecmag console. For example, phase, apodization, and baseline correction parameters can be applied and changed multiple times very quickly without the need to reopen the raw data file. Additionally, curve fitting routines for several common experiments have been automated, significantly decreasing the time spent determining important sample parameters.

## OMRI Injury Imaging

### TASK 2A: OMRI Hardware Development

The design and development of hardware systems required for Overhauser Magnetic Resonance Imaging (OMRI) is of key importance to Specific Aim 2. We describe below critical hardware design and sequence optimization as well as the realization of a new method for Overhauser-enhanced free radical fast imaging in the electromagnet LFI.

#### EPR coil design for OMRI 3D radical imaging

Development of EPR coils for 3D Overhauser-enhanced MRI has continued with several key advances. At the end of Y1, we obtained a 78-fold NMR signal enhancement in a TEMPO/water solution using an 8 mm diameter EPR coil (194 MHz) as a proof of principle in the electromagnet LFI. During Y2, Q1 we have designed and tested two different EPR coils designed to fit inside our 10 cm NMR imaging coil. A saddle coil design is frequently used as a transverse resonator for its large  $B_1$  amplitude, but can become unsuitable for large samples at high frequencies because increased resistance of the coil results in reduced performance. An Alderman-Grant (AG) coil is often used for larger coils at high frequencies as the resistive losses are less severe, often more than making up for the theoretical loss in maximum  $B_1$  amplitude compared to a saddle coil. To help minimize resistive losses in the coil, as well as reduce SAR on the sample, both of the coils were tuned to the low field nitroxide resonance of 140.8 MHz rather than the central resonance of 194 MHz. We been using glass formers for these coils as they provide excellent thermal stability in the presence of the Overhauser drive field.



With an eye towards imaging applications, scaling the EPR transmit coils for larger samples presents several challenges. Larger coils require higher input powers to achieve the same  $B_1$  as smaller coils. Additionally, large aqueous samples suffer significant more loss than smaller samples, resulting in a smaller quality factor and decreased  $B_1$  amplitude. This is problematic because Overhauser enhancement (and thus sensitivity to nitroxide radicals) requires large  $B_1$  amplitude. The new generation of coils is over 800 times larger by volume than the coil used to measure the 78-fold NMR enhancement last year and yet we succeeded in measuring a 50-fold NMR signal enhancement on a TEMPO/water solution.

### 3D Overhauser MRI using b-SSFP

As described above, we have successfully implemented 3D fast imaging on the LFI scanner using balanced steady state free precession sequence (b-SSFP), achieving imaging speeds 27 $\times$  faster as compared to 3D gradient echo sequences for the same resolution. Our next step aims to combine fast 3D imaging with Overhauser enhanced MRI (OMRI) to continue to improve temporal resolution and to prototype “injury-sensitive” imaging with free-radical solutions. Our manuscript describing this work in more detail, “High Speed 3D Overhauser-enhanced MRI using combined b-SSFP and Compressed Sensing” has been accepted for publication at Magnetic Resonance in Medicine, and is attached as Appendix 8.

OMRI exploits the dipolar coupling between the unpaired electrons of free radicals and the  $^1\text{H}$  nuclei of water to increase nuclear magnetization via dynamic nuclear polarization (DNP) and subsequently images the enhanced nuclear spin polarization with MRI. A difficulty of OMRI is that high power RF is needed to saturate the electron spin for a time on the order of the nuclear  $T_1$ . Additionally, as EPR frequencies are two orders of magnitude higher than  $^1\text{H}$  frequencies, a high frequency resonator is required, leading to high specific absorption rate (SAR), and limited penetration depth. For these reasons OMRI is usually performed at a low- to intermediate magnetic field [19] or in a field-cycled setup [20], [21] but these experiments are much slower and more complex than traditional MRI due to the need to refresh the DNP-enhanced signal many times within the acquisition time.

We redesigned the 3D b-SSFP sequence described on p. 8 to incorporate EPR pulses (Figure 38). Unlike other OMRI methods previously reported, this sequence requires no separate Overhauser polarization step. By taking advantage of a steady-state sequence, the problem of rapid decay of the Overhauser-enhanced signal is overcome by providing constant polarization in the sample during the acquisition instead of in a separate imaging step.



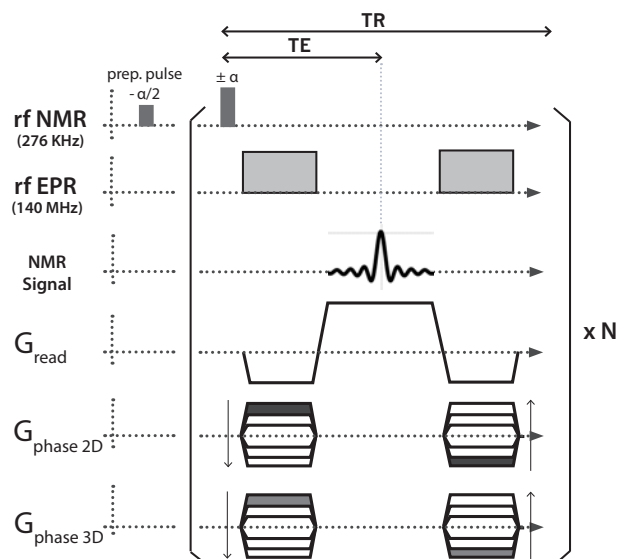


Figure 38: Diagram of the 3D b-SSFP sequence with embedded EPR pulses.  $N$  is the total number of TRs in the sequence.

### OMRI setup

A 7 cm OD, 13 cm long Alderman-Grant coil [22], [23] (Figure 39a) with guard rings to reduce sample heating was made to saturate the electron spin resonance of the nitroxide radical 4-hydroxy TEMPO (Sigma-Aldrich, St. Louis, MO, USA). The electron spin resonance is split into three transitions by the hyperfine coupling of the spin 1  $^{14}\text{N}$  nucleus. As the SAR scales with  $\omega^2$  [24]-[28] the EPR coil was tuned to the low energy transition of 140.8 MHz to minimize SAR. The EPR coil was placed inside of a 10 cm OD, 16 cm long solenoid coil used for NMR excitation and detection at 276 kHz (Figure 39b). The coils were oriented such that their  $B_1$  fields were perpendicular to each other and to  $B_0$ .

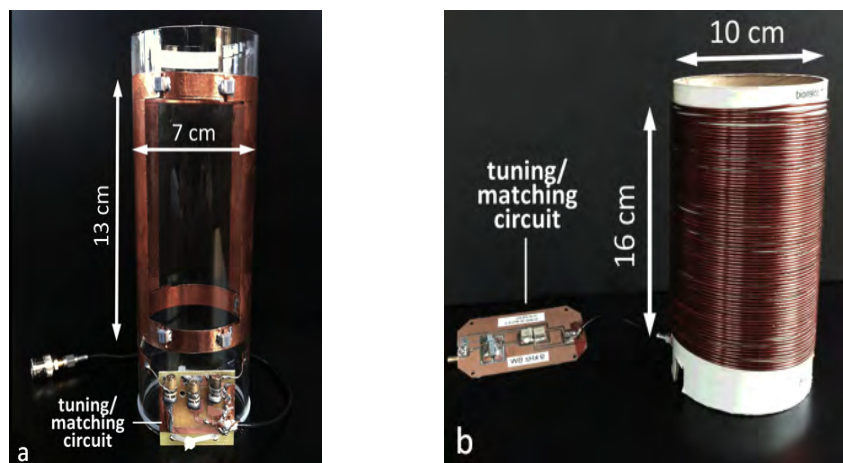


Figure 39: OMRI setup: photographs of (a) the EPR (140.8 MHz) and (b) NMR (276 KHz) coils used for the OMRI experiments.



In order to understand the approach of transverse magnetization to steady state with embedded EPR pulses in the sequence, Bloch simulations (Figure 40) were performed in a 1D experiment (without the phase encode gradients, i.e., at the center of  $k$ -space), with and without EPR irradiation to predict the buildup and time course of transverse magnetization as well as the signal enhancement provided by DNP. Input parameters to the simulations were the measured  $T_1$  and  $T_2$  relaxation times in the test sample, the measured DNP enhancement with 1.5 s EPR pulse ( $\sim 3 \times T_1$ ) in a 1D experiment (-44.5),  $TR/TE = 27/54$  ms and  $\alpha = 90^\circ$ . Simulations were run on MATLAB using code written in house. The corresponding experiments successfully matched with the simulations. The sequence was set with  $TR/TE = 27/54$  ms, total bandwidth  $BW = 9091$  Hz, and 71 Hz bandwidth per pixel.

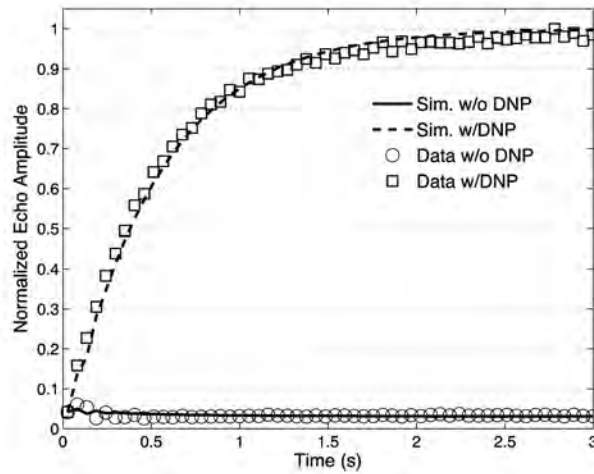


Figure 40: Simulation and measurement of the approach to steady-state with- and without DNP. Plotted are the echo amplitudes acquired during the pulse sequence of Figure 38 with only the read gradient active. The DNP signal is nearly 30 times larger than the signal without DNP after reaching steady-state. Solid curves plotted are *not* a fit to the data but rather an *exact* simulation with no free parameters.

### OMRI structured phantom design

A configurable imaging phantom was built for these experiments. Various pieces designed to demonstrate resolution in three dimensions and test the ability to resolve sharp edges in under-sampled  $k$ -space were 3D printed in polycarbonate on a Fortus 360mc (StrataSys, Eden Prairie, MN, USA). The 3D printed pieces were stacked inside a 5.5 cm ID, 13 cm long machined polycarbonate cylinder. The advantage of this phantom is the flexibility to design and 3D print any desired structure for a particular experiment. The cylinder was then filled with 250 mL of 2.5 mM 4-hydroxy TEMPO solution in water, and a leak-tight polycarbonate cap inserted. The assembled phantom and individual pieces are shown in Figure 41. Imaging experiments were performed in two different phantom stacking configurations. The first stacked geometry consists of two interlocking sets of a trio of stepwise-smooth cones and was used to evaluate the 3D character of the sequence and the minimum structure sizes that can be resolved for round shaped objects Figure 41 f–i. The second configuration used more complex structures with finer details to assess the sequence performance, ability to resolve small in plane structures (Figure 41 b–e).



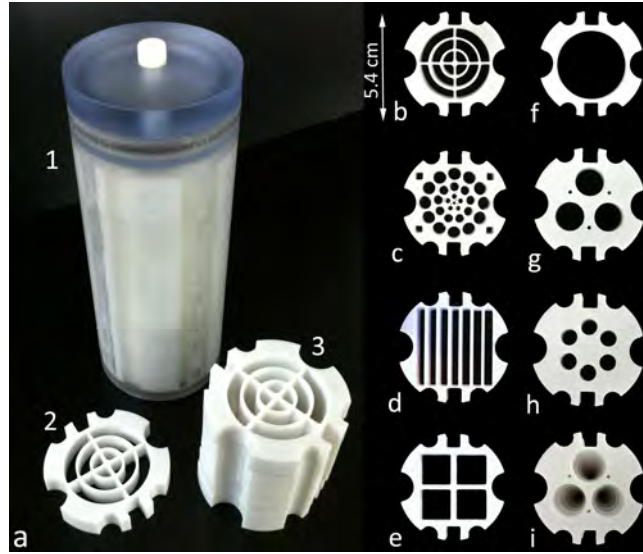


Figure 41: Photograph of (1a) the assembled OMRI phantom, (2a) a 10 mm thick internal piece, and (3a) a stack of internal pieces. Shown in (b-h) are individual pieces of the configurable phantom. A top view of the stacked pieces for the phantom in configuration 1 as described in the text is shown in (i).

### *Imaging*

The 3D imaging sequence was performed with full Cartesian acquisition of k-space. The sequence was set with  $TR/TE = 54/$  ms, a  $256 \times 64 \times 112$  mm<sup>3</sup> field of view, and acquisition matrix of  $128 \times 64 \times 32$ , resulting in a  $2 \times 1 \times 3.5$  mm<sup>3</sup> voxel size. Images are shown in Figure 42, Figure 43, and Figure 44. The balanced phase gradient durations were both set to 20 ms to reach the desired in plane spatial resolution when the gradient amplifiers were at maximum power. The readout duration was 14 ms with 9091 Hz bandwidth and total acquisition time was 114 s. Critical to the success of these experiments was a very stable magnetic field as off-resonance effects can distort the image and cause severe banding artifacts[1].



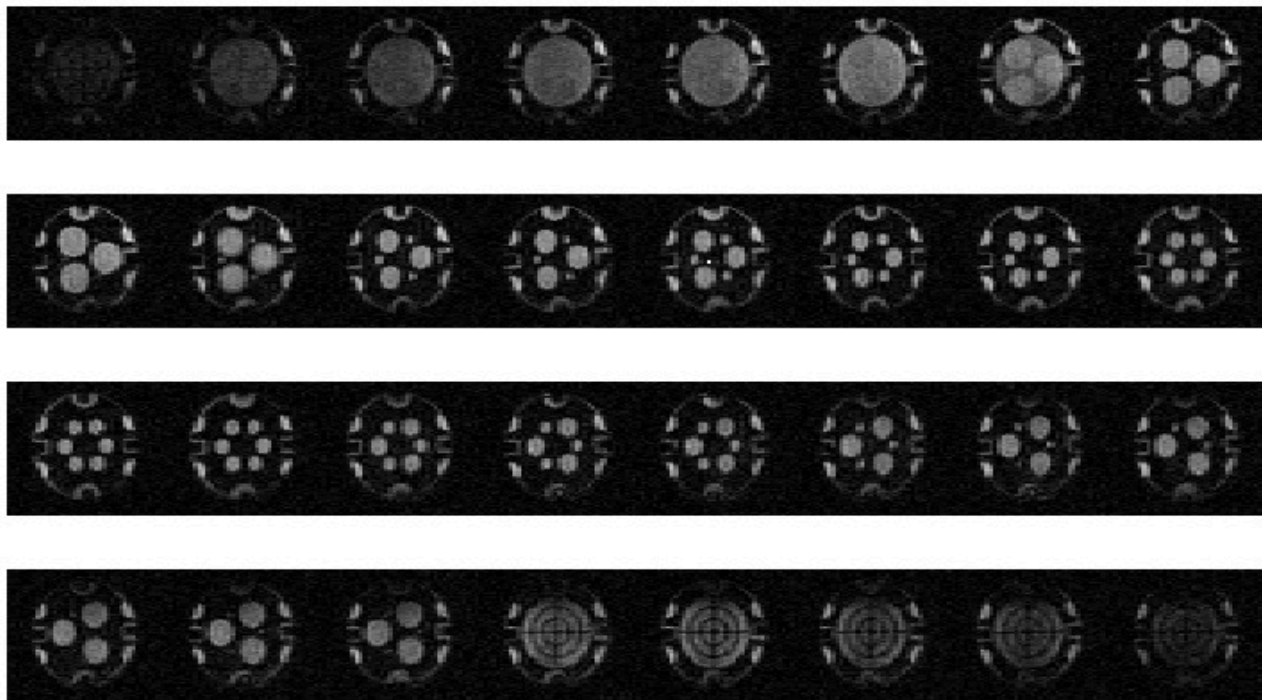


Figure 42: Images of the phantom of Figure 41 in configuration 1. Acquisition matrix:  $128 \times 64 \times 32$ , voxel size:  $2 \times 1 \times 3.5 \text{ mm}^3$ . Total acquisition time = 114 s. Maximum SNR = 23.

Application of the EPR irradiation while the gradients are on is possible because our maximum gradient strength is only  $0.1 \text{ Gauss} \cdot \text{cm}^{-1}$ , giving a spread in electron resonance frequencies across the 5.5 cm sample (in plane dimension) of  $\sim 1.54 \text{ MHz}$ . The loaded FWHM of our coil in an S21 measurement was  $\sim 2.3 \text{ MHz}$  ( $Q = 62$ ), thus the spread in electron spin frequencies is well covered.



Figure 43: 3D rendering of the two sets of interlocked stepwise-smooth cones (slices 8-27 from Figure 42)



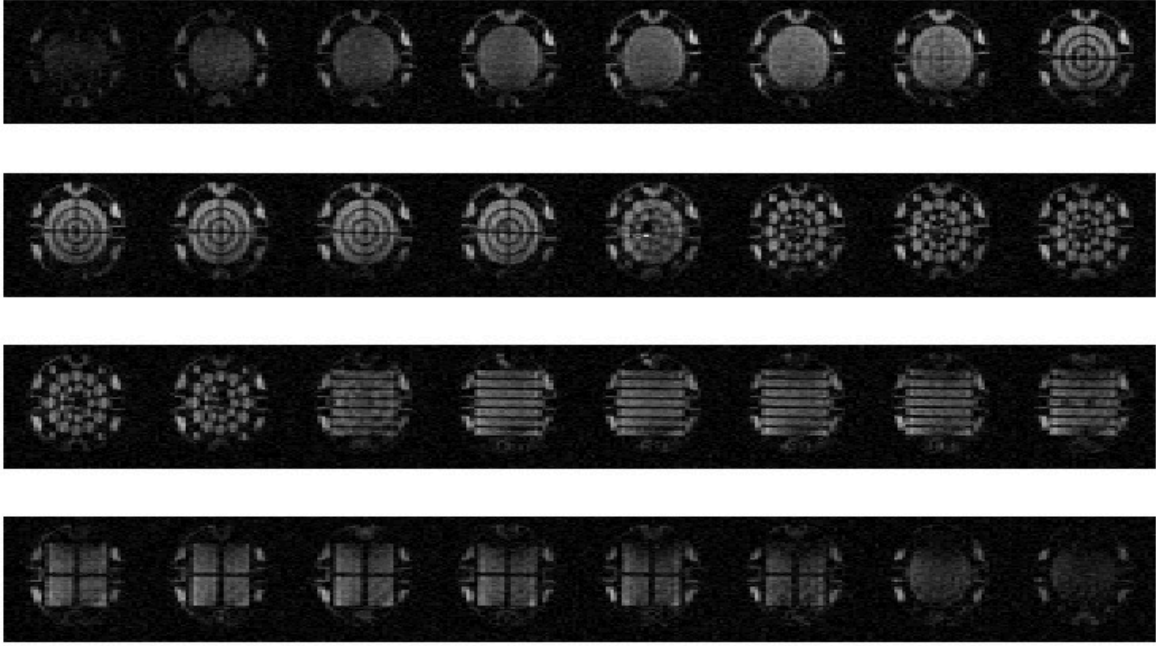


Figure 44: Images of the phantom of Figure 41 in configuration 2. Acquisition matrix:  $128 \times 64 \times 32$ , voxel size:  $2 \times 1 \times 3.5 \text{ mm}^3$ . Total acquisition time = 114 s. Maximum SNR = 24.6.

## TASK 2B: In vitro nitroxide Overhauser-enhanced proton spectroscopy

### Overhauser DNP sensitivity to free radicals

A key challenge in implementing OMRI for TBI will be detecting the small concentrations of NO radical present in vivo. Reports on the local concentrations of NO found in TBI patients are difficult to find, however a study of isolated rat ischemic hearts found more than a 10-fold increase in the EPR signal compared to a normally perfused heart indicating elevated levels of radical [29]. It has also been shown that the high levels of NO radical result from the reduction of nitrite, which was found to be  $\sim 12 \text{ mM}$  in ischemic rat hearts [30]. Thus we investigated the ability to detect small concentrations of nitroxide radical via the Overhauser effect by spectroscopy. DNP is usually associated with a larger signal than thermal equilibrium, but because the Overhauser enhanced signal has the opposite phase of the thermal equilibrium signal, useful contrast can be gained when the Overhauser effect is very weak. For concentrations as low as 20 mM, we observed an Overhauser signal with the opposite phase (Figure 45) as the thermal equilibrium signal (black line). At 10 mM nitroxide concentration, the Overhauser signal (blue line) is significantly smaller than the thermal equilibrium but has the same phase. While large signal enhancements would provide easy to observe contrast, these smaller signals can also be used by comparing an MRI with DNP to an MRI without DNP and looking at the difference between the two images [21]. Locations where free radical is present at sufficient concentrations will present a different signal between the two images so that free radical species may still be detected at small concentrations. We move now towards determining the sensitivity to free radical in b-SSFP imaging sequences as well as investigating theoretical limits to see if further improvements can be made.



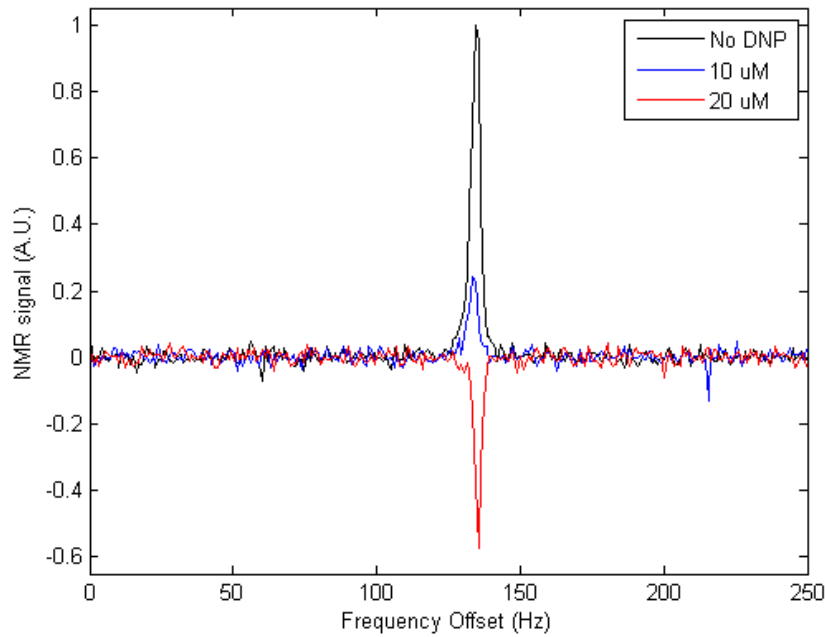


Figure 45: Measurement of the sensitivity threshold to small concentrations of nitroxide radical via Overhauser enhanced NMR spectroscopy. These spectra were acquired in the electromagnet LFI at 6.5 mT (276 kHz). The ESR frequency was 140 MHz.

### Investigation of free radical sensitivity in OMRI b-SSFP imaging sequences

At present, the amount of free radical produced in TBI and reperfusion injuries is not known, but estimates for NO concentrations range from nM to tens of  $\mu\text{M}$  [31]-[38]. It is therefore important to determine the sensitivity of our OMRI hardware to small radical concentrations. As described in the previous section and shown in Figure 45, DNP spectroscopy measurements of varying nitroxide concentrations were used to estimate our ultimate detection limit of nitroxide free radicals. In these experiments, we observe signal contrast for nitroxide concentrations down to 10  $\mu\text{M}$  and estimate that significant signal contrast is attainable under ideal conditions to  $< 7 \mu\text{M}$ . Ideal in this context means that the the DNP enhancement is not limited by the B1 field of the EPR coil, and that the competition between electron-nuclear dipolar relaxation (that drives DNP )with other relaxation mechanisms are not significantly affected. The first of these two conditions can be difficult to fulfill. In spectroscopy, small RF coils with high filling factors can be easily built to generate a strong B1. For imaging experiments, the coil often needs to surround a volume that is much larger than the area of interest due to the size of the sample, and this can significantly decrease B1. We therefore have tested our sensitivity using the OMRI setup described above. A 2D b-SSFP sequence with the following parameters was used: matrix size =  $128 \times 55$ , pixel size =  $2.5 \times 1.5$  mm, TR/TE = 49.52/24.56 ms,  $\alpha=90^\circ$ . Total acquisition time was 20 minutes. After image acquisition, a  $5\sigma$  threshold was applied to a reference image (Figure 46b) to remove noise. The signal regions of the reference image after applying the threshold were then used as a mask for the DNP image (Figure 46c).



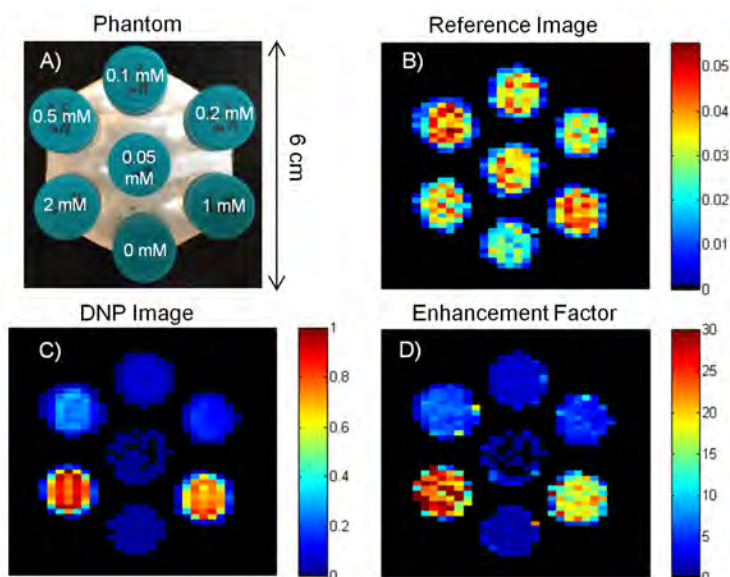


Figure 46: **A)** Photograph of the phantom used to measure sensitivity to small nitroxide radical concentrations. **B)** Reference b-SSFP image with no DNP pulses applied. The color scale is normalized to the peak amplitude of the image taken with DNP. **C)** Image with DNP using the same sequence parameters as the reference image. **D)** Pixel by pixel enhancement factor (*i.e.*, the DNP image amplitude divided by reference image amplitude). DNP contrast for all sample concentrations except for the control sample.

We used a phantom consisting of six vials of water with nitroxide concentrations ranging from 2 mM to 50  $\mu$ M (Figure 46A). A seventh vial with no free radical was used as a control to ensure the application of EPR pulses for DNP did not affect the signal. A reference MRI, acquired with no DNP, is shown in Figure 46B. It is worth noting in the reference image that all seven vials have very similar magnitudes regardless of the nitroxide concentration. This is due to the insensitivity of bSSFP to T1 as long as  $TR \ll T1$ . This is important because unlike relaxation contrast agents, such as Gd complexes, we can turn the DNP contrast on and off simply by turning the EPR pulses in the imaging sequence on and off. Figure 46C is an image taken with EPR pulses applied in the sequence. Figure 46B and Figure 46C differ only in the application of EPR pulses during the phase encode gradients as shown in Figure 38. Notice the difference in scale between the reference and DNP image (both images normalized to the maximum signal in the DNP image). The signal amplitude of the control sample with no free radical is the same as in the reference image. All samples except for the center vial of 50  $\mu$ M show an increase in signal implying positive contrast with DNP. The signal amplitude of the 50  $\mu$ M sample actually decreases by  $\sim 70\%$ . This means we still have significant negative contrast for 50  $\mu$ M nitroxide concentration. Figure 46D shows the pixel by pixel signal enhancement,  $E$  (*i.e.*, signal with DNP divided by reference signal).  $E$  greater than 1 represents positive contrast,  $E$  less than 1 is negative contrast, while  $E = 1$  means there is no signal contrast with DNP. The average enhancement factor for each vial is shown in Table 3.



Sample Conc.	Enhancement Factor
0 (Control)	$1 \pm 0.3$
0.05 mM	$0.25 \pm 0.2$
0.1 mM	$2.2 \pm 0.4$
0.2 mM	$4.5 \pm 1$
0.5 mM	$6 \pm 1$
1 mM	$18 \pm 3$
2 mM	$26 \pm 7$

Table 3: The average enhancement factor,  $E$ , calculated from Figure 46D for each of the seven vials.  $E > 1$  represents positive contrast,  $E < 1$  is negative contrast, and  $E = 1$  is no contrast. All concentrations show DNP contrast except the control sample.

## TASK 2C: *Ex vivo* nitroxide detection in whole blood

We have been developing protocols for the *ex vivo* detection of NO following a rodent transient ischemia/reperfusion model [39] of endogenous nitroxide production as a first step to estimate *in vivo* detection limits. We have established a collaboration with Dr. Cenk Ayata and Dr. Fannie Herisson in the departments of Neurology and Neuroscience at Massachusetts General Hospital, and they will perform the biological work described below.

### *Ischemia reperfusion model in rodents*

Endogenous reactive oxygen species such as hydroxyl radical  $\text{OH}^-$ , azote monoxide  $\text{NO}^-$ , superoxide anion  $\text{O}_2^-$ , and their combined highly reactive product peroxynitrite  $\text{ONOO}^-$  have been demonstrated in rodent models of cerebral ischemia [40], [41]. Comparing permanent and transient occlusion of the middle cerebral artery in rats, Peters and colleagues demonstrated a burst of free radical superoxide anion *in vivo* during the first hour following the recanalization, whereas permanent occlusion led to a steady increase in reactive oxygen species (ROS) production [42]. These ROS are normally inactivated by endogenous scavenging systems, but overwhelm them in ischemic conditions.

In the transient occlusion rodent models, a nylon filament is used to occlude the middle cerebral artery (MCA), one of the intracranial branches of the internal carotid artery. Rats are operated under anesthesia and temperature control system with a heating pad. After cervicotomy and dissection of the carotid bifurcation, the pterygopalatine artery, which is the only cervical branch of the internal carotid artery, is ligated. A nylon monofilament will be then inserted into the internal carotid artery from the external carotid artery and pushed in the circulation to the MCA in the brain. The right positioning and the effectiveness of the filament occlusion is continuously monitored by transcranial Doppler. After 30 to 60 minutes of filament occlusion, the reperfusion is allowed by removing the filament. Blood will be drawn following ischemia and reperfusion, and Overhauser-enhanced spectroscopy similar to that of Figure 45 will be performed on this sample to estimate the types of DNP enhancement factors that may be expected *in vivo*.



## KEY RESEARCH ACCOMPLISHMENTS:

### *Electromagnet LFI:*

- Demonstrated  $^1\text{H}$  imaging in the reconfigured biplanar electromagnet LFI head imager test bed at 6.5 mT (276 kHz) with 2 mm in-plane resolution using 3D gradient echo imaging
- Demonstrated 25 $\times$  faster  $^1\text{H}$  imaging in LFI using the first low-field implementation of b-SSFP
- Demonstrated an additional 6 $\times$  acceleration in  $^1\text{H}$  imaging using the first implementation of compressed sensing and undersampled b-SSFP at low field
- Developed 3D printed polycarbonate phantoms for use in both  $^1\text{H}$  MRI and OMRI experiments

### *Permanent magnet Halbach LFI:*

- Acquired high spatial resolution NMR-based magnetic field maps of the Halbach imaging field
- Developed and simulated strategy for spatial encoding and reconstruction
- Designed, built, and tested RF transmit coils
- Designed, built, and evaluated 8-channel RF receive array and channel multiplexer
- Evaluated and simulated effect of finite RF pulse length and off-resonance RF pulses
- Acquired initial 1D and 2D projection images of test phantom

### *Parallel imaging in electromagnet LFI*

- Designed, built, and evaluated 8-channel Rx array for 276 kHz
- Acquired and reconstructed the first 8-channel MRI image in the Johnson noise regime
- First demonstration of accelerated SENSE imaging in the Johnson noise regime.
- Developed and implemented passive multi-channel decoupling strategy suitable for low frequency

### *System control/Integration of Redstone console with electromagnet LFI*

- Fully integrated TNMR/MATLAB pulse sequence control
- Installed digital attenuator board and spec'd/tested new low-noise RX4 receiver module
- Developed NMR spectroscopy data processing suite
- Developed multi-channel data processing user interface
- Developed image reconstruction tools for accelerated parallel imaging

### *Overhauser NMR and MRI in electromagnet LFI:*

- Improved high-power high-Q EPR coils for OMRI imaging
- Simulated and measured NMR spin dynamics under b-SSFP combined with Overhauser DNP
- Developed new MRI sequence for free radical imaging: Overhauser-enhanced MRI using b-SSFP
- Acquired 32 slice, 1 mm in-plane resolution very high-speed OMRI free-radical images at 6.5 mT
- Calculated and measured sensitivity limit for free radicals Overhauser-enhanced spectroscopy
- Investigated free radical sensitivity in OMRI b-SSFP imaging sequences
- Established protocol to measure NO via *ex vivo* OEPS/OMRI in whole blood



## REPORTABLE OUTCOMES:

1. J P Stockman, C Z Cooley, M S Rosen, and L L Wald, “Flexible encoding and reconstruction strategies using a rotating inhomogeneous magnetic field for new MRI applications”, presented at the *ISMRM Data Sampling and Image Reconstruction Workshop*, 3–6 February 2013, Sedona, AZ.
2. M Sarracanie, B D Armstrong, and M S Rosen, “High speed 3D b-SSFP at 6.5 mT”, to be presented at the *2013 Experimental NMR Conference*, 14–19 April 2013, Pacific Grove, CA.
3. B D Armstrong, M Sarracanie, J Stockman, and M S Rosen, “High speed 3D Overhauser-enhanced MRI using combined b-SSFP and compressed sensing”, to be presented at the *2013 Experimental NMR Conference*, 14–19 April 2013, Pacific Grove, CA.
4. C D LaPierre, M Sarracanie, L L Wald, and M S Rosen, “Parallel imaging and acceleration in the Johnson noise dominated regime”, to be presented at the *2013 Experimental NMR Conference*, 14–19 April 2013, Pacific Grove, CA.
5. C Z Cooley, J P Stockman, B D Armstrong, M S Rosen, and L L Wald, “A lightweight, portable MRI brain scanner based on a rotating Halbach magnet”, to be presented at the *2013 Experimental NMR Conference*, 14–19 April 2013, Pacific Grove, CA.
6. M Sarracanie, B D Armstrong, and M S Rosen, “High speed 3D b-SSFP at 6.5 mT”, to be presented at the *2013 International Society for Magnetic Resonance in Medicine*, 20–26 April 2013, Salt Lake City, UT.
7. B D Armstrong, M Sarracanie, J Stockman, and M S Rosen, “High speed 3D Overhauser-enhanced MRI using combined b-SSFP and compressed sensing”, to be presented at the *2013 International Society for Magnetic Resonance in Medicine*, 20–26 April 2013, Salt Lake City, UT.
8. C D LaPierre, M Sarracanie, L L Wald, and M S Rosen, “Parallel imaging and acceleration in the Johnson noise dominated regime”, to be presented at the *2013 International Society for Magnetic Resonance in Medicine*, 20–26 April 2013, Salt Lake City, UT.
9. C Z Cooley, J P Stockman, B D Armstrong, M S Rosen, and L L Wald, “A lightweight, portable MRI brain scanner based on a rotating Halbach magnet”, to be presented at the *2013 International Society for Magnetic Resonance in Medicine*, 20–26 April 2013, Salt Lake City, UT.
10. J P Stockman, C Z Cooley, M S Rosen, and L L Wald, “Flexible spatial encoding strategies using rotating multipolar fields for unconventional MRI applications”, to be presented at the *2013 International Society for Magnetic Resonance in Medicine*, 20–26 April 2013, Salt Lake City, UT.
11. M S Rosen, invited talk, “New methods of low-field MRI for application to TBI”, given at the *Next Generation Medical Imaging Workshop*, Carnegie Mellon University, 5 Sept 2012, a video of which is available at [http://wms.andrew.cmu.edu:81/nmvideo/Bio/9\\_Rosen.mov](http://wms.andrew.cmu.edu:81/nmvideo/Bio/9_Rosen.mov)



12. M S Rosen, invited talk, “New methods of low-field MRI for application to TBI: first results”, given at the *Military Health System Research Symposium*, Ft Lauderdale, FL, 13-16 August 2012.
13. M S Rosen, “Molecular imaging at low magnetic field; endogenous and exogenous free radical MRI”, 28 January 2013, *MGH/Martinos Molecular Imaging Seminar*, Boston MA.
14. M Sarraçanie, B D Armstrong, J P Stockman, and M S Rosen, “High Speed 3D Overhauser-enhanced MRI using combined b-SSFP and Compressed Sensing”, accepted for publication in *Magnetic Resonance in Medicine*.

## CONCLUSION:

The reason MRI is not widely deployable is that high-strength magnetic fields (of order 1 T) are necessary with conventional MRI to obtain useful brain images. Such high magnetic fields involve large, heavy, fragile, expensive equipment (such as superconducting magnets) that is incompatible with operation in field hospitals. We contend that low-magnetic-field implementations of MRI can be developed to allow robust, transportable imaging modalities well suited to diagnose the types of battlefield injuries prevalent in TBI and practical for operation in field hospitals. Application of the suite of techniques and technologies from our work could advise future development of a deployable device with a high diagnostic impact and could be transformative, enabling improved diagnosis and monitoring of battlefield injuries prevalent in TBI.

Much of the hardware development for the human head LFI test bed systems (**Aim 1**) and for the OMRI system (**Aim 2**) was completed in Y1. Progress in Y2 for Aim 1 focused on imaging sequence development and optimization, and implementation of parallel imaging acceleration. Aim 2 efforts included work to maximizing the OMRI signal attainable from free-radical test solutions with a minimum of applied Overhauser power. We have also successfully demonstrated high-speed free-radical OMRI, and investigated the sensitivity of both NMR and MRI-based measurements to free radical concentrations as a path toward *in vivo* applications.

The electromagnet LFI has been optimized to provide an ideal state-of-the art test bed for all of the novel acquisition, detection methodologies, and reconstruction algorithms including navigators and sparse sampling, and additionally will provide necessary experience and data to advise optimal construction and magnetic field for any future electromagnet-based deployable systems. In its current configuration, this state-of-the-art scanner enables high-performance spectroscopy and 8-channel imaging at 6.5 mT, and is fully equipped for Overhauser DNP experiments. We continue to improve the ability to acquire images based on the intrinsic  $^1\text{H}$  signal by combining new low-field hardware methodology and advanced pulse sequence and reconstruction methods.

The imaging experiments presented above in the optimized electromagnet LFI are compelling: high quality  $^1\text{H}$  MRI at 6.5 mT is in fact attainable over reasonable averaging times using high performance hardware and advanced MRI sequences. A critical question for this work is the understanding of the clinical balance and impact that the tradeoff between acquisition time and resolution implicit in imaging plays on the operation of a deployable scanner.



Our second low field imaging test bed, the permanent magnet Halbach LFI is based around a lightweight (45 kg) and portable magnet with a built-in encoding field for MRI. Its a highly specialized and potentially disruptive scanner that could greatly ease both the cost and burden of a field-forward instrument purpose-built for TBI imaging. Imaging in the highly inhomogeneous magnetic field of the Halbach scanner is challenging, however results presented above using simultaneous NMR measurement to track magnet drift, and multi-channel receive arrays to unwrap image aliasing is encouraging.

We have also been developing technology for a wholly new approach to brain imaging that may revolutionize the use of MRI for the assessment and treatment of secondary brain injury following TBI: direct tomographic detection of endogenous free radicals as an early marker for TBI. This new form of contrast, “injury-sensitive MRI”, is based on the enormous signal enhancement attainable with Overhauser DNP, converting the electron spin of endogenous free radicals into nuclear polarization using the Overhauser effect and subsequently imaging that modified nuclear polarization using low-field MRI (OMRI).

We have developed and demonstrated a new, non-field-cycled strategy for fast high-resolution 3D OMRI using b-SSFP at 6.5 mT. The embedding of the EPR excitation pulses directly into the b-SSFP sequence which eliminates the pre-polarization step used in other OMRI sequences, reducing the acquisition time and obviating the need for long, high power RF EPR pulses. The use of undersampling strategies and compressed sensing reconstruction algorithms further reduces imaging time. We have shown that an undersampling rate of 70 % gives unperceivable reconstruction errors when compared with the fully sampled data sets

The low-field OMRI results presented above demonstrate promise for high-speed high-resolution free-radical imaging, and offers new perspectives for the measurement of free radicals in living organisms. The long-term goal of this work is an *in vivo* implementation of this technique. Free-radical sensitive low-field OMRI as a novel imaging and diagnostic MRI-based method with specificity to secondary-injury has the potential to clarify the mechanisms involved in secondary damage and the local effects of novel therapies. Time-critical imaging of free radicals can provide the unique interventional access critically needed for drug therapies and this technique would fill the clear need for an “injury imager”, suitable for non-invasive tomographic measurement (Figure 47).



Figure 47: Schematic of the development of a new interventional imaging and treatment tool for *in vivo* detection of endogenous free radicals associated with secondary injury following TBI using low-field OMRI as developed here. This same approach can similarly open up new treatment windows into stroke and other ischemic events. MRI-based *in vivo* free radical imaging using OMRI is impossible at high-field due to the inability of the ESR pulse to penetrate into tissue, and the danger of RF heating in the microwave regime.



Successful demonstration of this system *in vivo* will provide image-based injury specificity for TBI and for the first time open a window into a critical mechanism of TBI-related disease and an unambiguous non-invasive *in vivo* marker for cerebral injury. Time-critical imaging of free radicals associated with secondary injury can provide the unique interventional access critically needed to develop and deliver drug therapies to mitigate brain damage, reducing disability and death from secondary injury following TBI. The low-field approach would allow placement of this critical new diagnostic “injury imager” tool close to the source of injury—as well as in hospitals and clinics where rehabilitation takes place.

## REFERENCES:

- [1] K. Scheffler and S. Lehnhardt, “Principles and applications of balanced SSFP techniques,” *European Radiology*, vol. 13, no. 11, pp. 2409–2418, Nov. 2003.
- [2] E. J. Candes, J. Romberg, and T. Tao, “Robust uncertainty principles: exact signal reconstruction from highly incomplete frequency information,” *IEEE Trans. Inform. Theory*, vol. 52, no. 2, pp. 489–509.
- [3] “An Introduction To Compressive Sampling,” vol. 25, no. 2, pp. 21–30, 2008.
- [4] M. Lustig, D. Donoho, and J. M. Pauly, “Sparse MRI: The application of compressed sensing for rapid MR imaging,” *Magnetic Resonance in Medicine*, vol. 58, no. 6, pp. 1182–1195, 2007.
- [5] K. P. Pruessmann, M. Weiger, M. B. Scheidegger, and P. Boesiger, “SENSE: sensitivity encoding for fast MRI,” *Magnetic Resonance in Medicine*, vol. 42, no. 5, pp. 952–962, 1999.
- [6] N. de Zanche, C. Barmet, J. A. Nordmeyer-Massner, and K. P. Pruessmann, “NMR probes for measuring magnetic fields and field dynamics in MR systems,” *Magnetic Resonance in Medicine*, vol. 60, no. 1, pp. 176–186, Jul. 2008.
- [7] G. Schultz, H. Weber, D. Gallichan, W. R. T. Witschey, A. M. Welz, C. A. Cocosco, J. Hennig, and M. Zaitsev, “Radial Imaging With Multipolar Magnetic Encoding Fields,” *IEEE Trans. Med. Imaging*, vol. 30, no. 12, pp. 2134–2145.
- [8] J. P. Stockmann, P. A. Ciris, G. Galiana, L. Tam, and R. T. Constable, “O-space imaging: Highly efficient parallel imaging using second-order nonlinear fields as encoding gradients with no phase encoding,” *Magnetic Resonance in Medicine*, vol. 64, no. 2, pp. 447–456, 2010.
- [9] Q. Deng, J. Sharp, V. Volotovskyy, B. Tomanek, and S. King, “1D RF Phase Gradient Coil for TRASE RF Imaging,” presented at the Proc. Intl. Soc. Mag. Reson. Med., 2011, p. 1813.
- [10] J. C. Sharp and S. B. King, “MRI using radiofrequency magnetic field phase gradients,” *Magnetic Resonance in Medicine*, vol. 63, no. 1, pp. 151–161, Jan. 2010.
- [11] P. B. Roemer, W. A. Edelstein, C. E. Hayes, S. P. Souza, and O. M. Mueller, “The NMR phased array,” *Magnetic Resonance in Medicine*, vol. 16, no. 2, pp. 192–225, 2005.
- [12] G. C. Wiggins, C. Triantafyllou, A. Potthast, A. Reykowski, M. Nittka, and L. L. Wald, “32-channel 3 Tesla receive-only phased-array head coil with soccer-ball element geometry,” *Magnetic Resonance in Medicine*, vol. 56, no. 1, pp. 216–223, 2006.
- [13] M. H. Levitt and R. Freeman, “NMR population inversion using a composite pulse,” *Journal of Magnetic Resonance*, vol. 33, no. 2, pp. 473–476, 1979.
- [14] B. Luy, K. Kobzar, T. E. Skinner, N. Khaneja, and S. J. Glaser, “Construction of universal rotations



from point-to-point transformations,” *Journal of Magnetic Resonance*, vol. 176, no. 2, pp. 179–186.

- [15] H. Weber, D. Gallichan, G. Schultz, C. A. Cocosco, S. Littin, W. Reichardt, A. Welz, W. Witschey, J. Hennig, and M. Zaitsev, “Excitation and geometrically matched local encoding of curved slices,” *Magnetic Resonance in Medicine*, 2012.
- [16] F. Knoll, G. Schultz, K. Bredies, D. Gallichan, M. Zaitsev, J. Hennig, and R. Stollberger, “Reconstruction of undersampled radial PatLoc imaging using total generalized variation,” *Magnetic Resonance in Medicine*, pp. n/a–n/a, Jul. 2012.
- [17] D. Gallichan, C. A. Cocosco, G. Schultz, H. Weber, A. M. Welz, J. Hennig, and M. Zaitsev, “Practical considerations for in vivo MRI with higher dimensional spatial encoding,” *Magnetic Resonance Materials in Physics, Biology and Medicine*, vol. 25, no. 6, pp. 419–431, Apr. 2012.
- [18] C. D. LaPierre, M. Sarraçanie, L. L. Wald, and M. S. Rosen, “Parallel imaging and acceleration in the Johnson noise dominated regime,” To be presented at 21st Meeting of International Society of Magnetic Resonance in Medicine, Salt Lake City, Utah, April 20–26 2013. pp. 1–1, 11-Nov-2012.
- [19] Z. Sun, H. Li, S. Petryakov, A. Samouilov, and J. L. Zweier, “In vivo proton electron double resonance imaging of mice With fast spin echo pulse sequence,” *Journal of Magnetic Resonance Imaging*, vol. 35, no. 2, pp. 471–475, Dec. 2011.
- [20] W. Youngde, D. J. Lurie, and M. A. Foster, “Rapid imaging of free radicals in vivo using hybrid FISP field-cycled PEDRI,” *Physics in Medicine and Biology*, vol. 47, no. 7, pp. 1091–1100, Mar. 2002.
- [21] D. J. Lurie, D. J. Lurie, D. J. Lurie, G. R. Davies, G. R. Davies, G. R. Davies, M. A. Foster, M. A. Foster, M. A. Foster, J. M. S. Hutchison, J. M. S. Hutchison, and J. M. S. Hutchison, “Field-cycled PEDRI imaging of free radicals with detection at 450 mT,” vol. 23, no. 2, pp. 175–181, Feb. 2005.
- [22] D. Alderman and D. Grant, “An efficient decoupler coil design which reduces heating in conductive samples in superconducting spectrometers,” *J Magn Reson*, vol. 36, no. 3, pp. 447–451, 1979.
- [23] D. J. Lurie, H. Li, S. Petryakov, and J. L. Zweier, “Development of a PEDRI free-radical imager using a 0.38 T clinical MRI system,” *Magnetic Resonance in Medicine*, vol. 47, no. 1, pp. 181–186, Dec. 2001.
- [24] P. A. Bottomley and E. R. Andrew, “RF magnetic field penetration, phase shift and power dissipation in biological tissue: implications for NMR imaging,” *Physics in Medicine and Biology*, vol. 23, no. 4, pp. 630–643, May 2002.
- [25] J. Jin, *Electromagnetic Analysis and Design in Magnetic Resonance Imaging*. CRC Press, 1998.
- [26] C. M. Collins, S. Li, and M. B. Smith, “SAR and B1 field distributions in a heterogeneous human head model within a birdcage coil,” *Magnetic Resonance in Medicine*, vol. 40, no. 6, pp. 847–856, Dec. 1998.
- [27] C. M. Collins and M. B. Smith, “Calculations of B1 distribution, SNR, and SAR for a surface coil adjacent to an anatomically-accurate human body model,” *Magnetic Resonance in Medicine*, vol. 45, no. 4, pp. 692–699, 2001.
- [28] C. M. Collins and Z. Wang, “Calculation of radiofrequency electromagnetic fields and their effects in MRI of human subjects,” *Magnetic Resonance in Medicine*, vol. 65, no. 5, pp. 1470–1482, May 2011.



- [29] J. L. Zweier, P. Wang, and P. Kuppusamy, "Direct measurement of nitric oxide generation in the ischemic heart using electron paramagnetic resonance spectroscopy," *Journal of Biological Chemistry*, vol. 270, no. 1, pp. 304–307, 1995.
- [30] J. L. Zweier, P. Wang, A. Samouilov, and P. Kuppusamy, "Enzyme-independent formation of nitric oxide in biological tissues," *Nat Med*, vol. 1, no. 8, pp. 804–809, 1995.
- [31] P. A. Rashid, A. Whitehurst, N. Lawson, and P. M. W. Bath, "Plasma nitric oxide (nitrate/nitrite) levels in acute stroke and their relationship with severity and outcome," *Journal of Stroke and Cerebrovascular Diseases*, vol. 12, no. 2, pp. 82–87, Mar. 2003.
- [32] K. L. H. Carpenter, I. Timofeev, P. G. Al-Rawi, D. K. Menon, J. D. Pickard, and P. J. Hutchinson, "Nitric oxide in acute brain injury: a pilot study of NO<sub>x</sub> concentrations in human brain microdialysates and their relationship with energy metabolism," in *link.springer.com*, vol. 102, no. 41, Vienna: Springer Vienna, 2009, pp. 207–213.
- [33] C. Iadecola, "Bright and dark sides of nitric oxide in ischemic brain injury," *Trends in neurosciences*, vol. 20, no. 3, pp. 132–139, 1997.
- [34] L. Cherian, J. C. Goodman, and C. S. Robertson, "Brain nitric oxide changes after controlled cortical impact injury in rats," *Journal of neurophysiology*, vol. 83, no. 4, pp. 2171–2178, 2000.
- [35] L. Cherian, J. C. Goodman, and C. Robertson, "Neuroprotection with Erythropoietin Administration Following Controlled Cortical Impact Injury in Rats," *Journal of Pharmacology and Experimental Therapeutics*, vol. 322, no. 2, pp. 789–794, May 2007.
- [36] T. Malinski, F. Bailey, Z. G. Zhang, and M. Chopp, "Nitric oxide measured by a porphyrinic microsensor in rat brain after transient middle cerebral artery occlusion," *Journal of Cerebral Blood Flow & Metabolism*, vol. 13, no. 3, pp. 355–358, 1993.
- [37] M. J. Ahn, E. R. Sherwood, D. S. Prough, C. Yie Lin, and D. S. DeWitt, "The effects of traumatic brain injury on cerebral blood flow and brain tissue nitric oxide levels and cytokine expression," *Journal of Neurotrauma*, vol. 21, no. 10, pp. 1431–1442, 2004.
- [38] X. Zheng, K. Liu, and Y. Yang, "Real-Time Measurement of Murine Hippocampus Hippocampus NO Levels in Response to Cerebral Ischemia/Reperfusion Reperfusion," in *Nitric oxide methods and protocols*, vol. 704, no. 6, Totowa, NJ: Humana Press, 2010, pp. 73–80.
- [39] R. J. Traystman, J. R. Kirsch, and R. C. Koehler, "Oxygen radical mechanisms of brain injury following ischemia and reperfusion," *Journal of Applied Physiology*, vol. 71, no. 4, pp. 1185–1195, 1991.
- [40] Y. Gürsoy-Özdemir, H. Bolay, O. Saribaş, and T. Dalkara, "Role of endothelial nitric oxide generation and peroxynitrite formation in reperfusion injury after focal cerebral ischemia," *Stroke*, vol. 31, no. 8, pp. 1974–1981, 2000.
- [41] M. Suzuki, M. Tabuchi, M. Ikeda, and T. Tomita, "Concurrent formation of peroxynitrite with the expression of inducible nitric oxide synthase in the brain during middle cerebral artery occlusion and reperfusion in rats," *Brain research*, vol. 951, no. 1, pp. 113–120, 2002.
- [42] O. Peters, T. Back, U. Lindauer, C. Busch, D. Megow, J. Dreier, and U. Dirnagl, "Increased Formation of Reactive Oxygen Species After Permanent and Reversible Middle Cerebral Artery Occlusion in the Rat," *Journal of Cerebral Blood Flow & Metabolism*, pp. 196–205, Feb. 1998.



## APPENDICIES:

### Year 2 Statement of Work

We attach for reference the Year 2 SOW as **Appendix 1**.

### Abstracts accepted for presentation

We attach as **Appendices 2–7** six abstracts accepted for presentation that result from research presently funded in the Rosen lab by DoD/DMRDP. The first five of these will be presented at the 21<sup>st</sup> Annual Meeting of the International Society for Magnetic Resonance in Medicine (ISMRM), to take place 20–26 April 2013 in Salt Lake City, UT. An additional abstract was accepted for presentation at the ISMRM Data Sampling and Image Reconstruction Workshop, which took place 3–6 February 2013 in Sedona, AZ.

1. High speed 3D b-SSFP at 6.5 mT
2. High speed 3D Overhauser-enhanced MRI using combined b-SSFP and compressed sensing
3. Parallel imaging and acceleration in the Johnson noise dominated regime
4. A Lightweight, portable MRI brain scanner based on a rotating Halbach magnet
5. Flexible spatial encoding strategies using rotating multipolar fields for new MRI applications
6. Flexible encoding and reconstruction strategies using a rotating inhomogenous magnetic field for new MRI applications

### Manuscript accepted for publication

We attach as **Appendix 8** the manuscript “High Speed 3D Overhauser-enhanced MRI using combined b-SSFP and Compressed Sensing”, accepted for publication in *Magnetic Resonance in Medicine*.



<b>Y2 1. Low Field Imager</b>		
<b>Q1-4 1A</b>	Low-field MRI Hardware Development	<p>DEMONSTRATION of thermal management for electromagnet.</p> <p>DEMONSTRATION of B<sub>0</sub> homogeneity and stability.</p> <p>DEMONSTRATION of linearity of gradient coils.</p> <p>DEMONSTRATION of sensitivity and acceleration provided by of multi-coil-array parallel imaging system.</p>
<b>Q1-4 1B</b>	System Control and Image Acquisition	<p>INTEGRATE commercial MRI console with hardware developed in sub-task 1A.</p> <p>Complete DEVELOPMENT of image navigation and reconstruction methods.</p>
<b>Q3-4 1C</b>	Demonstration of Head Imager	DEVELOPMENT of head-shaped phantoms.
<b>Y2 2. OMRI injury imaging</b>		
<b>Q1-4 2A</b>	OMRI Hardware Development	OPTIMIZATION of OMRI system sensitivity based on findings from subtasks 2B and 2C.
<b>Q1-4 2B</b>	<i>In Vitro</i> NO Overhauser effect-Enhanced Proton Spectroscopy (OEPS)	COMPARISON of NO-Hb OEPS with free-NO OEPS in aqueous solution at a variety of Hb concentrations.
<b>Q3-4 2C</b>	<i>Ex Vivo</i> “Gold Standard” for NO Detection	DEVELOPMENT of protocols for “Gold Standard” <i>Ex Vivo</i> detection of NO-Hb in whole blood via X-band (9.4 GHz) Electron Paramagnetic Resonance (EPR) spectroscopy.

**YEAR 2 DELIVERABLES:** Detailed technical reports on development and initial tests of the low-field human head imager and the OMRI system for imaging Overhauser-enhanced free radicals.

## Appendix 1: Year 2 Statement of Work



# High Speed 3D b-SSFP at 6.5 mT

Mathieu Sarraçanie<sup>1,2</sup>, Brandon D. Armstrong<sup>1,2</sup>, and Matthew S. Rosen<sup>1,2</sup>

<sup>1</sup>Department of Physics, Harvard University, Cambridge, MA, United States, <sup>2</sup>MGH/Martinos Center for Biomedical Imaging, Boston, MA, United States

**Target audience:** MR physicists and clinicians interested in performing fast 3D imaging at very-low magnetic field and on the design of high-performance purpose-built MRI systems.

## Purpose

Without major innovation, high-field MRI instruments offer limited utility in field deployable and portable contexts. Our effort focuses on the high-risk and critical challenges that must be solved to enable deployment of transportable dedicated MRI systems. This includes the development of robust low-field scanner hardware methodologies, the development of state of the art high-speed imaging strategies and work on advanced adaptive reconstruction methods including navigators and sparse sampling. With the goal of demonstrating a proof-of-principle of a suite of techniques and technologies to advise future development of a field-deployable device with high diagnostic impact, the present work reports on the development of fast 3D imaging at very-low magnetic field (6.5 mT) using the intrinsic <sup>1</sup>H NMR signal and balanced steady state free precession (b-SSFP).

## Methods

A very stable magnetic field is a critical element of the experiment as off-resonance effects can distort the image and cause severe banding artifacts [2]. A custom built, low-field MRI scanner with a bi-planar 6.5 mT electromagnet (B<sub>0</sub>) and bi-planar gradients was used for all experiments and was previously described [1]. The system was upgraded and optimized for <sup>1</sup>H imaging resulting in improved B<sub>0</sub> stability, higher gradient slew rates, and lower overall noise. This effort included the use of an improved power supply (System 854T, Danfysik, Taastrup, Denmark) for the electromagnet with  $\pm 1$  ppm stability over 20 minutes and  $\pm 2$  ppm stability over 2 hours, and the addition of high-current shielded cables throughout the system. The scanner operates inside a double-screened enclosure (ETS-Lindgren, St. Louis, MO, USA) with a RF noise attenuation factor of 100 dB from 100 kHz to 1 GHz. The 3D imaging experiment was performed with Cartesian acquisition of k-space using b-SSFP. The sequence was set with TR/TE = 42/21 ms, acquisition matrix = 128×41×11, voxel size = 2.7×2.5×9 mm<sup>3</sup>, number of averages (NA) = 40. The readout duration was 7.04 ms with 9091 Hz bandwidth and total acquisition time was 12.6 min for fully sampled k-space.

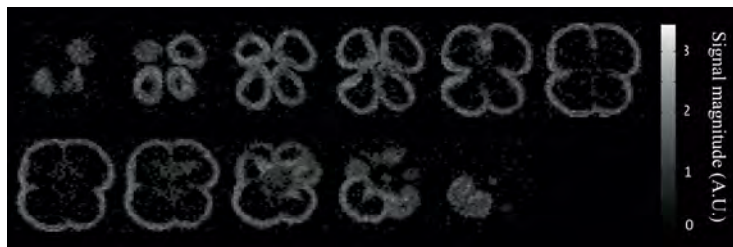


**Figure 1:** 11 slices of the imaged bell pepper at 6.5 mT with 2.7×2.5×9 mm<sup>3</sup> resolution in 12.6 min.



**Figure 2:** 3D rendered image of the bell pepper reconstructed from the acquired MRI dataset.

## Results

Figure 1 shows the 11 slices of a bell pepper acquired using 3D b-SSFP with 2.7×2.5×9 mm<sup>3</sup> resolution. Figure 2 shows a 3D rendered image of the reconstructed object.

## Conclusion

3D imaging across a 10 cm diameter bell pepper with 2.7×2.5×9 mm<sup>3</sup> voxel size was achieved within 13 min at 6.5 mT. This result is the first implementation of b-SSFP at very low magnetic field. The presented work overcomes the main limitations of working at low field, which typically results in poor SNR and prohibitively long acquisition times, by using a custom built optimized scanner with stable magnetic field B<sub>0</sub> and low overall noise that allows implementation of b-SSFP imaging. The use of undersampling strategies and compressed sensing reconstruction algorithms could further reduce the imaging time. We have recently shown that an undersampling rate of 70 % gives unperceivable reconstruction errors when compared with fully sampled data sets [3]. Thus, we expect the total acquisition time for the presented image to reach ~6 min and ~3 min with 50% and 70% undersampling respectively. The optimized bi-planar electromagnet combined with fast 3D imaging strategies and sparse sampling has potential to reach clinical standards for patient imaging and open new perspectives for a generation of low-cost, high-performance, and purpose-built imagers practical for operation in hospitals, battlefield medical facilities, or forward triage centers.

**References:** [1] Tsai LL *et al.* JMR 2008; 193: 174-85 ; [2] Scheffler K *et al.* Eur Radiol 2003;13:2409-18; [3] Sarraçanie M *et al.* MRM 2012; submitted.

**Acknowledgement:** This research was supported by the Department of Defense, Defense Medical Research and Development Program, Applied Research and Advanced Technology Development Award W81XWH-11-2-0076 (DM09094).



# High Speed 3D Overhauser-Enhanced MRI using combined b-SSFP and Compressed Sensing

Brandon Dean Armstrong<sup>1,2</sup>, Mathieu Sarraçanie<sup>1,2</sup>, Jason Stockmann<sup>1,2</sup>, and Matthew Rosen<sup>1,2</sup>

<sup>1</sup>Physics, Harvard University, Cambridge, MA, United States, <sup>2</sup>Martinos Center for Biomedical Imaging, Boston, MA, United States

**Target Audience:** Free radical imaging, hyper-polarization, MR method development and hardware

## Purpose

Free radical imaging has been used to investigate physiological processes such as  $pO_2$  mapping and to monitor the distribution and metabolism of free radicals in organs under oxidative stress. We present a new pulse sequence for rapid 3D imaging of free radicals using Overhauser-enhanced MRI (OMRI). In contrast to other OMRI methods that use a time consuming pre-polarization Overhauser irradiation step, the sequence presented here embeds the EPR pulses into the phase encode step of a balanced steady state free precession sequence (b-SSFP), greatly reducing the acquisition time. A further increase in temporal resolution is gained by undersampling of k-space and using compressed sensing reconstruction. This new OMRI sequence enables both improved spatial and temporal resolution of free radical distribution than other techniques.

## Methods

Experiments were performed in a custom built, 6.5 mT, bi-planar electromagnet with bi-planar gradients. A 7 cm OD, 13 cm long Alderman-Grant coil was used to saturate the 140.8 MHz electron spin resonance of the nitroxide radical 4-hydroxy-TEMPO. The EPR coil was placed inside a 10 cm OD, 16 cm long solenoid coil for  $^1H$  NMR excitation and detection. The EPR irradiation pulses were embedded into the phase encode and rewind steps of a fully balanced SSFP sequence as shown in Figure 1. 3D printed polycarbonate pieces 5.4 cm in diameter were used as a phantom (Figure 2a) with 2.5 mM TEMPO solution in water. Pieces were designed to evaluate the ability to resolve small feature in 3 dimensions. Image parameters were: matrix =  $256 \times 64 \times 32$ , voxel size =  $1 \times 1 \times 3.5$  mm,  $TR/TE = 54/27$  ms,  $\alpha = 90^\circ$ , 70% undersampling rate, acquisition time = 65 s.

## Results

Figure 2a) shows two segments of our phantom with the corresponding images in Figure 2b). The under-sampled data accurately reproduces the object, including the 1 mm diameter holes and 1 mm spacer. To confirm that this new sequence with imbedded EPR pulses is still a steady-state sequence, the sequence was run with only the read gradient while the echo amplitude was measured. After an initial buildup of polarization due to  $T_1$ , the signal reaches a steady-state amplitude that is  $\sim 30X$  larger than without embedded EPR pulses.

## Conclusion

Embedding electron spin saturation into the phase encode step allows the use of a traditional b-SSFP sequence with no additional timings added. This is the first source of acceleration compared to traditional OMRI sequences that have a pre-polarization step of order  $T_1$  before acquiring several lines of k-space. Further, for the phantom imaged here, only 30% of k-space is necessary to faithfully reproduce the image, reducing the acquisition time by a factor of 3. This technique will improve our ability to monitor physiological processes involving free radicals as the distribution of radicals can be tracked with greater spatial and temporal resolution. **Acknowledgement:** Funded by DoD, Defense Medical Research and Development Program, Applied and Advanced Technology Development Award W81XWH-11-2-0076 (DM09094).

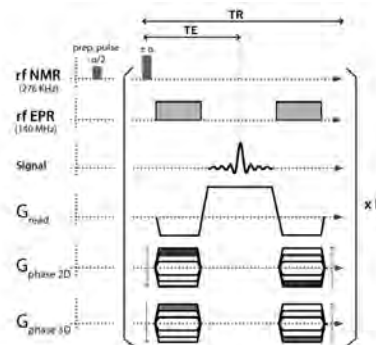


Figure 1. The 3D b-SSFP sequence with embedded EPR pulses.

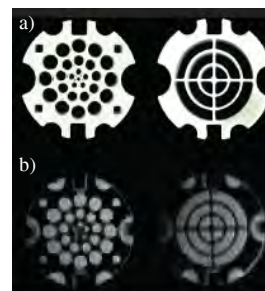


Figure 2. 2 slices from an OMRI image at 6.5 mT with  $1 \times 1 \times 3.5$  mm resolution over a  $200 \text{ cm}^3$  sample in 65 s. Phantom is 5.4 cm in diameter.



# Parallel Imaging and Acceleration in the Johnson Noise Dominated Regime

Cristen D. LaPierre<sup>1,2</sup>, Mathieu Saracanie<sup>1,2</sup>, Lawrence L. Wald<sup>1,3</sup>, and Matthew S. Rosen<sup>1,2</sup>

<sup>1</sup>Department of Radiology, Mass General Hospital, A.A. Martinos Center for Biomedical Imaging, Charlestown, MA, United States, <sup>2</sup>Department of Physics, Harvard University, Cambridge, MA, United States, <sup>3</sup>Harvard-MIT Division of Health Sciences and Technology, Cambridge, MA, United States

**Target Audience:** Those interested in portable MRI, low field imaging, SENSE acceleration, and inductive coil and array construction at low magnetic fields.

**Purpose:** Low field imaging offers a potentially transportable and rapidly deployable human imaging system. Current research for low field human imaging is limited and generally uses superconducting quantum interference device (SQUID) sensors<sup>1</sup>. At conventional magnetic field strengths body noise dominates, resulting in strongly correlated noise on each receive coil in the parallel array. At low field, uncorrelated Johnson noise dominates, providing a benefit to parallel imaging and accelerated imaging using SENSEitivity Encoding (SENSE). The aim of this study was twofold. First, construct an eight-coil receive only array for 276 kHz. Second, acquire accelerated images using SENSE.

**Methods:** NMR parallel imaging at low frequency is a new regime; optimal parameters for inductive receive coils are unknown from the literature. Three design parameters were identified: diameter, wire gauge and number of turns. Parameters were selected using a fractional factorial design at the factor levels indicated in Table 1. Only circular coils were tested.

Once optimal parameters were determined an 8 channel receive-only 276 kHz ring array was constructed. Imaging of 13.1 cm diameter phantoms filled with 0.04% Gadolinium doped saline (0.9% NaCl) was performed in a previously described<sup>2</sup> custom built very-low field MRI scanner with a 6.5 mT biplanar electromagnet and biplanar gradients and eight receive channels. A 3D balanced Steady State Free Precession (b-SSFP) sequence with full Cartesian acquisition of k-space was applied over five 20 mm thick slices, with FOV=225×160×100 mm<sup>3</sup>, acquisition matrix=64×64×5, TE/TR=12/23 ms, number of averages (NA)=150. Image reconstruction was performed with a sum-of-squares method<sup>3</sup>.

1D SENSE reconstruction (reduction factor R=2) was simulated on the middle slice of the fully sampled image using in-house code previously developed in our lab. The noise covariance matrix and coil sensitivity maps were estimated from the data. Finally, the corresponding experiment (R=2) was performed from a structured phantom. Noise data were acquired using a b-SSFP sequence with RF transmission disabled (sequence time = 704s). Sensitivity maps were estimated from the fully sampled data set acquired previously using third-order polynomial smoothing. Aliased images were unfolded using a modified version of the simulation code.



**Figure 1.** 8 channel receive only 6.5 mT parallel imaging array.

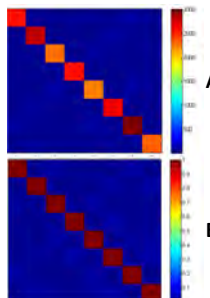


**Figure 4.** Noise covariance (A) and correlation coefficient (B) matrices.

**Results:** Optimal coil design parameters were identified as 8 cm diameter, 24 gage and 30 turns. An 8 channel receive only array with an inner diameter of 15.6 cm was built (Figure 1). Geometric decoupling between neighbors was -38 dB or less for nearest neighbors and -11 dB or less for next nearest neighbors. Figure 2 shows the design of the structured phantom (2a), as well as the reconstructed image of the structured phantom (2b) and a homogeneous phantom (2c) acquired with the 8 channel array. Figure 3 shows the noise covariance matrix (3a) and the correlation coefficient matrix (3b) of the array. Figure 4 shows the results of simulated (left) and actual (right)

SENSE reconstructed images.

**Discussion:** Due to low thermal signal, low field imaging requires signal averaging, increasing scan time. With the eight channel array, SENSE acceleration can be implemented, reducing scan time by at least a factor of 2. The negligible noise correlation between channels benefits this approach.

**Conclusions:** These results represent the first parallel and SENSE reduction images attained in the Johnson noise dominated regime. Development of parallel imaging and SENSE acceleration are important steps toward human imaging at very-low field. Future work will optimize the sequence to further improve image quality. Additional array designs will be tested and SENSE combined with random undersampling strategies will be investigated.

**Acknowledgements:** The authors would like to thank Jonathan Polimeni for his guidance on parallel imaging and Fa-Hsuan Lin for making available his SENSE reconstruction code.

**Financial Disclosure:** This research was supported by the Department of Defense, Defense Medical Research and

Development Program, Applied Research and Advanced Technology Development Award W81XWH-11-2-0076 (DM09094).

**References:** 1. Zotev VS, et al. JMR. Jun 2008;192(2):197-208

2. Tsai LL, et al. JMR. Aug 2008;193(2): 274-85

3. Roemer PB, et al. MRM. Nov 1990;16(2):192-225

Gauge (AWG)	Number of Turns					
	3	10	20	30	50	100
20	+	+	+	+	+	+
24	+	+	+	+	+	+
28	+	+	+	+	+	+

**Table 1.** Fractional factorial design for determining optimal coil design. Parameters tested were number of turns, size of wire and diameter of coil.



**Figure 2.** Phantom pattern (A), reconstruction of structured phantom (NA=150, B) and reconstruction of homogeneous phantom (NA=200, C). Images are masked to the phantom.

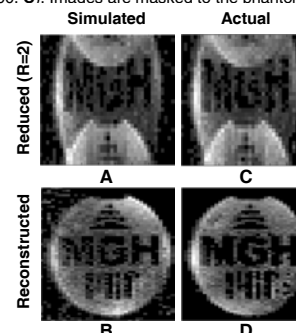


**Figure 3.** Simulated (A,B) and actual (C,D) results for SENSE reconstruction. Images are masked to the phantom.



## A Lightweight, Portable MRI Brain Scanner Based on a Rotating Halbach Magnet

Clarissa Zimmerman Cooley<sup>1,2</sup>, Jason P Stockmann<sup>2,3</sup>, Brandon D Armstrong<sup>2,3</sup>, Matthew S Rosen<sup>2,3</sup>, and Lawrence L Wald<sup>2,4</sup>

<sup>1</sup>Electrical Engineering, Massachusetts Institute of Technology, Cambridge, MA, United States, <sup>2</sup>Athinoula A. Martinos Center for Biomedical Imaging, Department of Radiology, Massachusetts General Hospital, Charlestown, MA, United States, <sup>3</sup>Department of Physics, Harvard University, Cambridge, MA, United States, <sup>4</sup>Department of Radiology, Massachusetts General Hospital, Harvard Medical School, Boston, MA, United States

**PURPOSE:** We constructed and tested a portable permanent magnet based brain MRI scanner suitable for operation in an ambulance, battle field, sports arena, or at the patient's bedside. Our goal is to allow emergency medical teams to assess brain hemorrhage from surgical complications, traumatic brain injury or stroke to accelerate care to those requiring it. The system eliminates the need for gradient coils thru a novel encoding method which rotates the  $B_0$  field inhomogeneity pattern of the lightweight permanent magnet creating generalized projections similar to O-Space<sup>1</sup> or PatLoc<sup>2</sup> encoding. We show experimental 2D, proof-of concept images, and discuss generalization to 3D.

**METHODS:** A 45 kg (36cm dia. 36cm length) Halbach cylinder magnet was built with NdFeB magnets (Fig. 1a)<sup>3,4</sup>. The center field is 77 mT (3.285 MHz) with about 1 mT (43 kHz) field variation in the center slice FOV of 16 cm. The magnet's encoding field has a roughly hyperbolic multipolar shape (Fig. 1b) that is physically rotated around the phantom during data collection. Because the encoding field cannot be switched, a spin echo sequence is used for radiofrequency refocusing of the spins, forming a projection of the phantom at each rotation. The field maps are measured and used as prior knowledge to construct the encoding matrix. Data is collected on a TecMag Apollo spectrometer with a 250 W Tomco RF amplifier and the image is reconstructed using the iterative algebraic reconstruction technique (ART)<sup>5</sup>.

Accurate field maps at each rotation are critical to image reconstruction. A single row of 8 solenoidal field-probes each holding a 1-mm water-filled capillary doped with copper sulfate ( $T_1=100$  ms) are used to collect field information as the magnet is rotated. The field measurements are fit using polynomial basis functions (Fig 1b). The lack of magnet shielding exposes our encoding field to external fields, the most significant being the earth's field which adds vectorially to the encoding field. This is explicitly corrected for when calculating the encoding matrix. Other external fields and magnet field drift ( $\sim 1/2G/^\circ C$ )<sup>6</sup> are measured using an MR field probe fixed to the magnet and also incorporated into the reconstruction.

For proof of concept, imaging phantoms were made using two 1" balls of doped water (Fig. 3a and 3e). In one experiment high SNR was achieved by directly winding the TR coil around the balls of water. In another experiment we used a volume Tx coil and an array of 4x 6.5cm dia. loop coils for Rx. In both case short, high power excitation pulses (125 W for a 40  $\mu s$  refocusing pulse) were necessary to cover the bandwidth of the encoding field.

**RESULTS:** Fig. 2 shows an example set of rotated field maps and the corresponding projections from the phantom. Fig. 3b is the reconstructed image of the same phantom using the Rx single coil. The data consisted of 128-average spin echoes with TR/TE = 200ms/9.4ms and 40 kHz readout bandwidth. Eighty projection angles were used. Fig. 3c shows the same reconstructed phantom imaged using 4 surface coils, 24 projections angles, 256 averages, and TR/TE = 200ms/20.4ms. Fig. 3d shows a simulated reconstruction with the same parameters as Fig. 3c. Fig. 3f and 3g show the experimental and simulated single coil image from the phantom in Fig. 3e (w/ 128 averages of 35 projection angles). Unlike the first phantom, there is a ball in the center of the encoding field.

**DISCUSSION:** Blurring throughout the image is greatly improved by the external field and temperature drift corrections, but some obvious artifacts remain. In Fig. 2b, the balls are located in the top half of the phantom, but we clearly see aliasing in the reconstructed images. This is expected because of the non-bijection of the encoding field<sup>1</sup>. The problem is resolved in Fig. 2c-d, in which the coil sensitivities from a 4 channel coil array are used to remove the ambiguity between frequency-matched isocontours in different quadrants. Blurring in the center is seen in Fig. 3f-g. Similar to Patloc imaging, the resolution of the images is lowest in the center because of the low field variation in that area. We propose shifting the encoding field off-center from the rotation axis (using shims) to address this, similar to O-Space imaging<sup>2</sup>.

**CONCLUSION:** These initial images and simulations are a 2D proof of concept for imaging in a rotating inhomogeneous field without additional gradient coils. Reconstruction would be simpler if the magnet was RF shielded and if the temperature was painstakingly regulated.

However, this would limit portability of the system, and we have shown that these inconveniences can be mitigated by careful field calibration before imaging and field drift monitoring during imaging. Future work will include the use of Transmit Array Spatial Encoding (TRASE)<sup>7</sup> for slice localization in the longitudinal direction to enable 3D imaging.

**REFERENCES:** (1) Schultz G, IEEE Trans Med Imag 2011. (2) Stockmann, MRM 2010. (3) Zimmerman C ISMRM 2012. (4) Halbach K, Nucl Instr Meth 1980. (5) Herman G, Comp. Biol. Med. 1976. (6) Campbell P, Permanent Magnet Materials & their Application, 1994. (7) Sharp J, MRM 2010. **ACKNOWLEDGMENTS:** The authors thank C Lapierre, M Saracanie, J Blau, and E Siskind for their help. Support by DoD/USAMRRA W81XWH-11-2-0076 (DM09094).

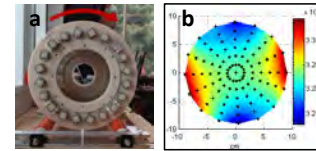


**Figure 1:** (a) magnet on high friction rollers, (b) interpolated field map in Hz, black dots are the field probe positions

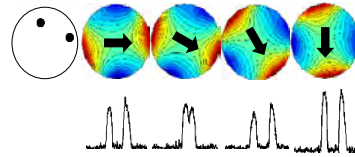


**Figure 2:** Six representative encoding field rotations and experimental projections of phantom on left. (1 coil, 128 averages, SNR ~ 30). Arrow is  $B_0$  direction.

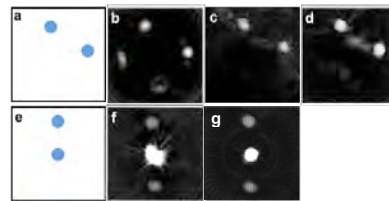


**Figure 3:** (a) ground truth phantom 1, (b) 80 projections of phantom 1 using one solenoid receive coil (c) 24 projections of phantom 1 using 4 receive coils, (d) simulated version of Fig. 3c, (e) ground truth phantom 2, (f) 35 projections of phantom 2 using one coil, (g) simulated version of Fig. 3f. Field of view is 16 cm in all images.



## Flexible spatial encoding strategies using rotating multipolar fields for unconventional MRI applications

J. P. Stockmann<sup>1,2</sup>, C. Z. Cooley<sup>3</sup>, M. S. Rosen<sup>1,2</sup>, L. L. Wald<sup>1</sup>

<sup>1</sup>Massachusetts General Hospital, Charlestown, MA

<sup>2</sup>Department of Physics, Harvard University, Cambridge, MA

<sup>3</sup>Department of Electrical Engineering, Massachusetts Institute of Technology, Cambridge, MA

**PURPOSE:** Our goal is to perform flexible MR imaging with rotating nonlinear spatial encoding magnetic (SEM) fields, removing constraints on hardware design, and reducing the cost, complexity, and weight of imaging systems. By shifting the burden away from hardware performance and toward computer power in the form of generalized reconstruction algorithms, we open the door to unconventional MR imaging systems for applications where spatially-varying resolution can be tolerated. Several encoding strategies using quadratic and nonlinear SEMs have recently been proposed as a way to accelerate parallel imaging and reduce peripheral nerve stimulation during field switching [1-3]. Common to all higher-order encoding methods is the problem of aliasing due to redundant frequency contours (causing a non-bijective mapping), which can be resolved using additional spatial encoding from local RF receive coils. Another issue is the flatness of higher-order SEMs at the center of the FOV, where encoding can only be achieved through the addition of linear SEMs. The present work builds on these approaches by assessing the encoding of a rotating SEM (wrt the object), with and without parallel imaging and a spatial offset between the axis of rotation and the axis of field symmetry, breaking the symmetry of the SEM within the FOV.

**METHODS:** We simulate imaging performance with a nonlinear SEM comprised primarily of second-order spherical harmonics with some additional higher-order terms (Fig. 1). To break the symmetry of the field by shifting it off-center, we also simulate the SEM with the addition of a linear field component (2000 Hz/cm or 3000 Hz/cm). We further simulate the use of multi-channel RF receive coils to remove aliasing. Approximate RF coil sensitivities for an 8-channel loop array are calculated using the Biot-Savart law (Fig. 2). Field maps of the SEM at each rotation angle as well as the coil sensitivities are used to build the encoding matrix. A GRE transverse brain slice acquired on a 3T scanner is used to generate the simulated data. The simulated readout duration is 7 ms with a 36 kHz bandwidth (Nyquist sampled). Reconstruction is performed using the algebraic reconstruction technique (ART) [4], which cycles through the encoding matrix one row at a time, back-projecting the data point corresponding to each row (Fig. 3). The algorithm iterates until convergence is achieved.

**RESULTS:** The spatially-varying resolution of the two SEMs can be visualized by looking at overlaid frequency isocontours of each SEM as it is rotated over the range of encoding angles (Fig. 4). Even with the non-ideal encoding fields used here, much of the detail in the object is retained in the reconstructions (Fig. 5). As expected, a linear offset SEM recovers resolution, though some detail is still lost at the center. Surface coils are effective in reducing aliasing artifacts and also in improving resolution, particularly when no field offset is used.

**DISCUSSION:** All SEMs can be approximated with linear combinations of spherical harmonics. The geometric similarity of a multipolar harmonic implies that unique projections of the object can be obtained using only a limited range of rotation angles [1]. For SEMs without a significant linear term, the range of rotation angles is  $180^\circ/N$ , where  $N$  is the order of the dominant SEM. For the multipolar SEM case considered here, the dominant components are the second-order harmonics  $XY$  and  $X^2-Y^2$ , hence the SEM is rotated over  $90^\circ$ . However, when the multipolar symmetry of the field is broken by the addition of a linear term, unique projections of the object can be acquired over  $360^\circ$ , similar to O-Space imaging. The linear term shifts the symmetry point away from the rotation axis, improving image resolution near the center of the FOV, as shown in Fig. 5.

**CONCLUSION:** Flexible reconstruction methods relax the need for a homogenous  $B_0$  field and linear gradient fields, as illustrated here using a single rotated multipolar SEM. This permits unconventional encoding strategies and MR imaging systems in applications that do not require isotropic resolution. Performance gains are achieved by breaking the symmetry of SEMs using multiple receive coils and/or a linear field offset. Future work will generalize the approach to three dimensions, possibly through curvilinear slice selection [5]. A total generalized variation prior [6] will also be used to help suppress streaking artifacts for highly undersampled data. **REFERENCES:** [1] Schultz G, TMI 2011. [2] Stockmann JP, MRM 2010. [3] Gallichan D, MRM 2011. [4] Kaczmarz S, Bull. Acad. Polon. Sci. Lett. A, 1937. [5] Weber, MRM 2012. [6] Knoll F, MRM 2012. **ACKNOWLEDGEMENTS:** Grant support DoD/USAMRRA W81XWH-11-2-0076 (DM09094).

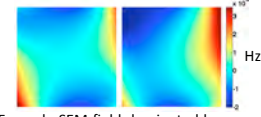


**Fig. 1** Example SEM field dominated by second-order terms (left). In order to provide spatial encoding at the center of the FOV, the SEM is offset using a linear component (a 2000 Hz/cm offset is shown here).

**Fig. 2** Encircling array of 8 RF receive coils used to remove aliasing caused by the non-bijectivity of the multipolar SEM.

**Fig. 3** ART backprojects the  $i_n^{\text{th}}$  row of encoding matrix  $E$  weighted so as to achieve consistency between data vector  $s$  and image  $m$ . The rate of convergence is controlled by  $\lambda$ .

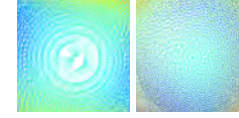


**Fig. 4** Spatially-varying resolution illustrated qualitatively by the density of overlapping frequency isocontours from 16 rotations of the SEMs in Fig. 1. Isocontours are plotted with 1 kHz separation. The symmetric SEM (left) rotates over  $90^\circ$  while the offset SEM rotates over  $360^\circ$  and provides smaller voxel sizes in the center.

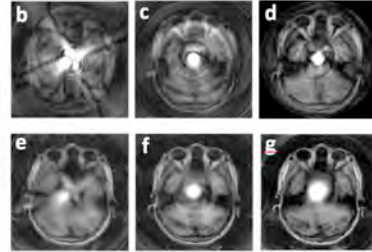


**Fig. 5** Simulated  $256 \times 256$  reconstructions of reference brain image (a) encoded using 128 projections by SEMs with no offset (a), 2000 Hz/cm offset (b), and 3000 Hz/cm (c) with no coil encoding. The offset removes most of the aliasing associated with the symmetry of the multipolar SEM and also recovers some resolution near the center. The addition of 8 receive coils for each case (e-g) improves resolution and removes aliasing, though resolution remains better near the periphery. FOV is 28 cm.



## Flexible encoding and reconstruction strategies using a rotating inhomogeneous magnetic field for new MRI applications

Jason P. Stockmann<sup>1,2</sup>, Clarissa Zimmerman Cooley<sup>3</sup>, Matthew S. Rosen<sup>1,2</sup>, Lawrence L. Wald<sup>1</sup>

<sup>1</sup>Massachusetts General Hospital, Charlestown, MA, USA, <sup>2</sup>Harvard University, Department of Physics, Cambridge, MA, USA, <sup>3</sup>Massachusetts Institute of Technology, Cambridge, MA, USA

**PURPOSE:** Our goal is to perform flexible MR imaging with rotating inhomogeneous  $B_0$  fields, removing constraints on hardware design and reducing the cost, complexity, and weight of imaging systems. By shifting the burden away from hardware performance and toward computer power in the form of generalized reconstruction algorithms, we open the door to unconventional MR imaging systems for applications where spatially-varying resolution can be tolerated. As proof of concept for this approach, we built a portable, lightweight, low-power, permanent magnet brain MR scanner suitable for operation in an ambulance or remote location. The system eliminates the need for gradient coils and power supplies through a novel encoding method which rotates a  $B_0$  field with an approximately quadrupolar inhomogeneity pattern around the object, creating generalized projections similar to “radial PatLoc” [2] encoding. In this abstract, we show preliminary experimental images and discuss encoding and reconstruction in the context of generalized projections.

**NONLINEAR ENCODING:** Common to all higher-order gradient encoding methods [2-4] is the problem of aliasing due to redundant frequency contours, which can be resolved using additional spatial encoding from local RF receive coils [2]. Another issue is the flatness of higher-order fields at the center of the FOV, where encoding can only be achieved through the addition of linear or odd-spatial order fields [3]. The present work builds on these approaches by assessing the encoding of a single rotating field, with and without parallel imaging and a spatial offset between the axis of rotation and the axis of field symmetry.

**METHODS:** We acquire data using a 45kg (36cm dia., 36cm length) Halbach cylinder array built with NdFeB permanent magnets (Fig. 1) [1]. The center field is 77 mT (3.285 MHz) with ~1 mT (43 KHz) field variation within the center slice FOV of 16 cm, permitting generalized projections to be obtained by rotating the magnet around the object (Fig. 2). A spin echo sequence with TR/TE=200ms/9.4ms and 40 kHz bandwidth was played on a Tecmag Apollo spectrometer. We then perform simulated encoding/reconstruction to test the effect of breaking the field symmetry by shifting it off-center using a linear component (2000 Hz/cm or 3000 Hz/cm). We further simulate the use of an encircling array of 8 local RF receive coils to remove aliasing. Time-domain reconstruction is performed using the algebraic reconstruction technique (ART) [5], which cycles through the encoding matrix one row at a time, back-projecting the data point corresponding to each row (Fig. 3). ART iterates until convergence is achieved.

**RESULTS:** Even with the non-ideal encoding fields used here, much of the detail in the object is retained in the reconstructions (Fig. 5). As expected, a linear offset recovers resolution, though some detail is still lost at the center. Surface coils are effective in reducing aliasing artifacts and also in improving resolution, particularly when no field offset is used.

**DISCUSSION:** The geometric redundancy of a multipolar harmonic implies that unique projections of the object can be obtained using only a limited range of rotation angles [2]. For fields without a significant linear term, the range of rotation angles is  $180^\circ/N$ , where  $N$  is the order of the dominant field. For the multipolar case considered here, the dominant components are the second-order harmonics  $XY$  and  $X^2-Y^2$ , hence the field is rotated over  $90^\circ$ . However, when the multipolar symmetry of the field is broken by a linear term, unique projections of the object can be acquired over  $360^\circ$ , similar to O-Space imaging [3]. The linear term shifts the symmetry point away from the rotation axis, improving image resolution near the center of the FOV, as shown in Fig. 5.

**CONCLUSION:** Flexible reconstruction methods relax the need for a homogenous  $B_0$  field and linear gradient fields, as illustrated here using a single rotated multipolar field. This permits unconventional encoding strategies and MR imaging systems in applications that do not require isotropic resolution. Performance gains are achieved by breaking the symmetry of fields using multiple receive coils and/or a linear field offset. Future work will generalize the approach to three dimensions, possibly through curvilinear slice selection [6]. A total generalized variation prior [7] will also be used to help suppress streaking artifacts for highly undersampled data. **REFERENCES:** [1] Zimmerman C, ISMRM 2012. [2] Schultz G, TMI 2011. [3] Stockmann JP, MRM 2010. [4] Gallichan D, MRM 2011. [5] Kaczmarz S, Bull. Acad. Polon. Sci. Lett. A, 1937. [6] Weber, MRM 2012. [7] Knoll F, MRM 2012. **ACKNOWLEDGEMENTS:** Grant support DoD/USAMRRA W81XWH-11-2-0076 (DM09094).

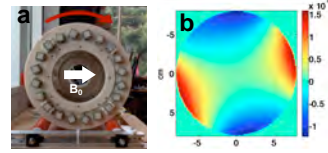


**Figure 1.** (a) Halbach magnet on high friction rollers with rotation direction shown by orange arrow, (b) measured axial field variation (central slice) in Hz.

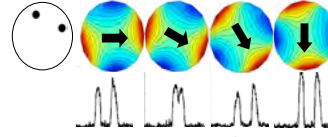


**Figure 2.** Six representative encoding field rotations and experimental projections of phantom on left (1 coil, 128 ave, SNR~30). Arrow is  $B_0$  direction.

**Fig. 3** ART backprojects the  $n^{\text{th}}$  row of encoding matrix  $E$  weighted so as to achieve consistency between data vector  $s$  and the  $n^{\text{th}}$  image estimate,  $m^{(n)}$ . Convergence rate is set by  $\lambda$ .

$$\hat{m}^{(n+1)} = \hat{m}^{(n)} + \lambda \frac{s_n - \langle E_n, \hat{m}^{(n)} \rangle}{\|E_n\|^2} E_n^*$$

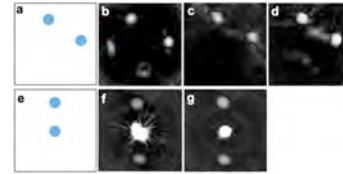


**Figure 4.** (a) Ball locations in ground truth phantom 1, (b) 80 projections of phantom 1 using one solenoid receive coil (c) 24 projections of phantom 1 using 4 receive coils, (d) simulated version of Fig. 3c, (e) ground truth phantom 2, (f) 35 projections of phantom 2 using one coil, (g) simulated version of Fig. 3f. FOV is 16 cm.

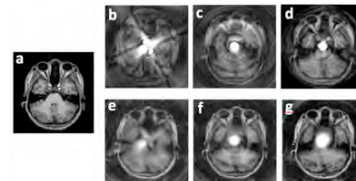


**Figure 5.** Simulated 256x256 reconstructions of reference brain image (a) encoded using 128 projections with no field offset (b), 2000 Hz/cm offset (c), and 3000 Hz/cm (d) with no RF coil encoding. The offset removes much of the aliasing associated with the symmetry of the multipolar fields and recovers some resolution near the center. The addition of 8 receive coils for each case (e-g) further improves resolution and removes aliasing, though resolution remains better near the periphery. Simulated FOV is 28 cm.





## High Speed 3D Overhauser-enhanced MRI using combined b-SSFP and Compressed Sensing

Journal:	<i>Magnetic Resonance in Medicine</i>
Manuscript ID:	MRM-12-13777.R1
Wiley - Manuscript type:	Full paper
Date Submitted by the Author:	11-Jan-2013
Complete List of Authors:	Sarracanie, Mathieu; Harvard University, Department of Physics; MGH/Martinos Center for Biomedical Imaging, Armstrong, Brandon; Harvard University, Department of Physics; MGH/Martinos Center for Biomedical Imaging, Jason, Stockmann; Harvard University, Department of Physics; MGH/Martinos Center for Biomedical Imaging, Rosen, Matthew; Harvard University, Department of Physics; MGH/Martinos Center for Biomedical Imaging, ; Harvard Medical School,
Research Type:	Technique Development < Technical Research
Research Focus:	No specific tissue or organ focus

SCHOLARONE™  
Manuscripts



**High Speed 3D Overhauser-Enhanced MRI using combined b-SSFP and Compressed Sensing**

Mathieu Sarraclane<sup>1,2</sup>, Brandon D. Armstrong<sup>1,2</sup>, Jason Stockmann<sup>1,2</sup>, and Matthew S. Rosen<sup>1,2,3</sup>

<sup>1</sup>Department of Physics, Harvard University, 17 Oxford St, Cambridge, MA 02138, USA

<sup>2</sup>MGH/Martinos Center for Biomedical Imaging, 149 13th St, Suite 2301, Boston MA 02129, USA

<sup>3</sup>Harvard Medical School, 25 Shattuck St, Boston, MA 02115, USA

Running title: 3D OMRI using b-SSFP and Compressed Sensing

**Corresponding author:**

Matthew S. Rosen

**Low Field MRI and Hyperpolarized Media Laboratory**

Harvard University Department of Physics

Massachusetts General Hospital

Martinos Center for Biomedical Imaging

149 13th Street, Suite 2301

Charlestown, MA 02129

USA

e-mail: [mrosen@cfa.harvard.edu](mailto:mrosen@cfa.harvard.edu)

LFI Lab: (617) 643-8636

Fax: (617) 726-7993

Word count: 4994



## Abstract

### Purpose

Overhauser-enhanced MRI (OMRI) is a promising technique for imaging the distribution and dynamics of free radicals. A key challenge for OMRI is attaining high spatial and temporal resolution while simultaneously limiting resonator and sample heating due to the long, high power radiofrequency (RF) pulses needed to saturate the electron resonance.

### Methods

The approach presented here embeds EPR pulses within a balanced steady state free precession (b-SSFP) sequence. Unlike other OMRI methods, no separate Overhauser pre-polarization step is required. This steady-state approach also eliminates the problem of time-varying Overhauser-enhanced signal and provides constant polarization in the sample during the acquisition. A further increase in temporal resolution was achieved by incorporating undersampled k-space strategies and compressed sensing reconstruction.

### Results

We demonstrate  $1 \times 2 \times 3.5 \text{ mm}^3$  resolution at 6.5 mT across a  $54 \times 54 \times 110 \text{ mm}^3$  sample in 33 s while sampling 30% of k-space.

### Conclusion

The presented work overcomes the main limitations of Overhauser enhanced MRI described so far in the literature with drastic improvement in terms of speed and resolution, thus offering new perspectives for the measurement of free radicals in living organisms, and for the study of dynamic processes such as metabolism and flow.

Word count: 191

Key words: 3D Overhauser MRI, free radicals, EPR, b-SSFP, Compressed Sensing



Introduction

Imaging of free radicals has been used to investigate a number of important physiological processes such as the mapping of  $pO_2$  (1-3), free radical distribution and metabolism (4-7), molecular imaging (8), and to monitor changes in local viscosity (9,10). Magnetic Resonance Imaging (MRI) is a powerful and noninvasive tool that provides excellent anatomical detail. However, MRI is sensitive to nuclear spins (typically  $^1H$  of water) and cannot alone reveal spatial information about the distribution of free radical species. EPR imaging (11-17) (EPRI) does give the spatial distribution of unpaired electron spins, but requires a separate MRI to determine where the free radicals are located within the sample. While EPRI is a sensitive technique, images have poor resolution due to broad EPR lines, and are usually time-inefficient due to the usual CW acquisition strategy. Overhauser-enhanced MRI (18-23) (OMRI, also known as proton-electron double resonance imaging) exploits the dipolar coupling between the unpaired electron of the free radical and the  $^1H$  nuclei of water to increase nuclear magnetization via dynamic nuclear polarization (DNP) and subsequently images the enhanced nuclear spin polarization with MRI. OMRI provides an excellent way to image free radical species as narrow NMR line widths enable imaging using reasonable-strength encoding gradients. OMRI also benefits from the ability to use traditional MRI sequences, though specialized hardware is needed to drive the electron spin resonance and the sequences must be modified to allow for EPR saturation pulses.

A difficulty of OMRI is the need for high power RF to saturate the electron spin for a time on the order of the nuclear  $T_1$ . Additionally, as EPR frequencies are two orders of magnitude higher than  $^1H$  frequencies, a high frequency resonator is required, and this leads to high specific absorption rate (SAR) and limited penetration depth. For these reasons OMRI is usually performed at a low- to intermediate magnetic field (5,22,24) or in a field-cycled setup (4,25). A typical field-cycled OMRI experiment begins at very low magnetic field (~5 mT) where EPR irradiation is applied for approximately the nuclear  $T_1$  of the sample at the irradiation magnetic field. The magnetic field is then quickly ramped up to the imaging field and a line or plane of k-space data is acquired. The field must then be switched back down for EPR irradiation because the DNP signal decays with the  $^1H$  nuclear  $T_1$ . Field-cycled OMRI helps to overcome both the hardware and penetration depth challenges by reducing the EPR frequency, but these



experiments are much slower and more complex than traditional MRI due to the need to refresh the DNP-enhanced signal many times within the acquisition time.

We present here a new method for 3D OMRI based on b-SSFP at a constant field of 6.5 mT that provides up to seven fold acceleration compared to the fastest OMRI sequence reported in the literature (24). We further maintain the high acquisition efficiency of b-SSFP by applying the Overhauser saturation pulses during the phase encode step, eliminating the time-consuming pre-irradiation step done in all previously reported OMRI. Additionally, we add undersampling strategies and compressed sensing (CS) techniques to increase the temporal resolution while also reducing the total number of EPR RF pulses. We obtain  $1 \times 2 \times 3.5 \text{ mm}^3$  resolution on a  $54 \times 54 \times 110 \text{ mm}^3$  sample in 33 s. We show that a steady-state signal is still achieved with this new OMRI b-SSFP sequence and that simulations with no free parameters agree very well with the experimental results.

## Materials and Methods

### *OMRI setup*

A custom built, low-field MRI scanner with a bi-planar 6.5 mT electromagnet ( $B_0$ ) and bi-planar gradients was used for all experiments and was previously described (26) (Figure 1.a). The system was upgraded and optimized for  $^1\text{H}$  imaging for this work resulting in improved  $B_0$  stability, higher gradient slew rates, and lower overall noise. This effort included the use of an improved power supply (System 854T, Danfysik, Taastrup, Denmark) for the electromagnet with  $\pm 1$  ppm stability over 20 minutes and  $\pm 2$  ppm stability over 2 hours, and the addition of high-current shielded cables throughout the system. The scanner operates inside a double-screened enclosure (ETS-Lindgren, St. Louis, MO, USA) with a RF noise attenuation factor of 100 dB from 100 kHz to 1 GHz.

The transfer of electron spin polarization to dipolar or scalar coupled nuclear spins via the Overhauser effect requires high power irradiation of the electron spin resonance (27,28). A 7 cm OD, 13 cm long Alderman-Grant coil (29,30) (Figure 1.b) with guard rings to reduce sample heating was used to saturate the electron spin resonance of the nitroxide radical 4-hydroxy TEMPO (Sigma-Aldrich, St. Louis, MO, USA). The electron spin resonance is split into three



transitions by the hyperfine coupling of the spin 1  $^{14}\text{N}$  nucleus (at 6.5 mT, there still exist other transitions described by the Breit-Rabi equations but their transition probabilities are small and ignored here) (31). As SAR scales with  $\omega^2$  (32-36) the EPR coil was tuned to the low energy transition of 140.8 MHz to minimize SAR. The EPR coil was placed inside a 10 cm OD, 16 cm long solenoid coil used for NMR excitation and detection at 276 kHz (Figure 1.c). The coils were oriented such that their  $B_1$  fields were perpendicular to each other and to  $B_0$ . Placing the NMR coil outside the ESR coil sacrifices NMR filling factor to gain larger  $B_1$  for electron spin saturation as our DNP signal enhancement (defined as  $\langle I_z \rangle / I_0$  where  $I_0$  is the thermal equilibrium NMR signal and  $\langle I_z \rangle$  is the DNP signal) is limited by the available RF power.

A Redstone NMR console (Tecmag Inc., Houston, TX, USA) was used for data acquisition and controlled the gradients and RF channels. The console has two transmit channels allowing for both NMR and EPR irradiation. A 100 W, CW amplifier (BT00100-DeltaB-CW) was used for EPR saturation and a 500 W pulsed amplifier (BT00500-AlphaS) was used for NMR (both from Tomco Technologies, Stepney, Australia).

*Phantom design*

A configurable imaging phantom was built for these experiments. Various pieces designed to demonstrate resolution in three dimensions and test the ability to resolve sharp edges in under-sampled k-space were 3D printed in polycarbonate on a Fortus 360mc (StrataSys, Eden Prairie, MN, USA). The 3D printed pieces were stacked inside a 5.5 cm ID, 13 cm long machined polycarbonate cylinder. The advantage of this phantom is the flexibility to design and 3D print any desired structure for a particular experiment. The cylinder was then filled with 250 mL of 2.5 mM 4-hydroxy TEMPO solution in water, and a leak-tight polycarbonate cap inserted. The assembled phantom and individual pieces are shown in Figure 2a, 1-3. Imaging experiments were performed in two different phantom stacking configurations. The first stacked geometry consists of two interlocking sets of a trio of stepwise-smooth cones and was used to evaluate the 3D character of the sequence and the minimum structure sizes that can be resolved for round-shaped objects (Figure 2.f-i). The second configuration used more complex structures with finer details to assess the sequence performance, ability to resolve small in-plane structures, and the results of undersampling on sharp edges (Figure 2.b-e). Fiber optic temperature probes (Luxtron,



LumaSense Technologies, Santa Clara, CA, USA) were placed inside the phantom and near a ring capacitor on the EPR coil during tests of the imaging sequence to monitor sample and coil temperatures.

### *3D Balanced SSFP with DNP*

The pulse sequence used is shown in figure 3. It is important to note that there is no separate EPR saturation step unlike all OMRI sequences reported in the literature. The sequence is a b-SSFP sequence with the addition of EPR (Overhauser) irradiation during the balanced phase encode gradients. The b-SSFP excitation train consists of an initial  $-\alpha/2$  preparation pulse immediately followed by a train of alternating  $\pm\alpha$  excitation pulses as previously described by Sheffler *et al* (37). The  $\pm\alpha$  pulses are separated by TR and the time interval between the  $-\alpha/2$  preparation pulse and the first  $\alpha$  pulse was set to 2  $\mu$ s. The main benefit of using a preparation pulse is that it prevents large fluctuations of the pre-steady state signal that would produce image artifacts and thus could not be used for signal acquisition (37). In b-SSFP, the optimal flip angle  $\alpha$  is given by  $\cos(\alpha) = \frac{T_1/T_2 - 1}{T_1/T_2 + 1}$  (37).  $T_1$  and  $T_2$  in our phantom were measured to be 545 ms and 488 ms respectively, which leads to an optimal flip angle of  $\alpha \sim 90^\circ$ .

Bloch simulations were performed for a sequence without phase gradients (i.e., at the center of k-space), both with- and without EPR irradiation to model the buildup and time course of transverse magnetization as well as the signal enhancement provided by DNP. The simulations were run in Matlab (MathWorks, Natick, MA, USA) using code written in-house. Input parameters to the simulations were the measured  $T_1$  and  $T_2$  relaxation times, the measured enhancement provided by DNP with a 1.5 s EPR pulse ( $\sim 3 \times {}^1\text{H } T_1$ ) in a 1D spectroscopy experiment ( $-44.5$  fold enhancement),  $TR/TE = 54/27$  ms and  $\alpha = 90^\circ$ . This negative enhancement results from Overhauser DNP pumping into the opposite spin nuclear ground state compared to the Boltzmann case. This sign is important for the simulations. OMRI experiments with these parameters, a total bandwidth  $BW = 9091$  Hz, and a 71 Hz bandwidth per pixel, were run and compared with the simulations.

The 3D imaging experiment was performed initially with full Cartesian acquisition of k-space. The sequence was set with  $TR/TE = 54/27$  ms, a  $256 \times 64 \times 112 \text{ mm}^3$  field of view, and acquisition matrix of  $128 \times 64 \times 32$ , resulting in a  $2 \times 1 \times 3.5 \text{ mm}^3$  voxel size. The balanced phase



gradient durations were both set to 20 ms to reach the desired in-plane spatial resolution when the gradient amplifiers were at maximum power. The readout duration was 14 ms with 9091 Hz bandwidth and total acquisition time was 114 s for fully sampled k-space. Critical to the success of these experiments is a very stable magnetic field as off-resonance effects can distort the image and cause severe banding artifacts (37).

It should be noted that the application of EPR saturation pulses while the gradients are on is only possible because our maximum gradient strength is low,  $0.1 \text{ Gauss}\cdot\text{cm}^{-1}$ , giving a spread in electron resonance frequencies across the 5.5 cm sample (in-plane dimension) of  $\sim 1.54 \text{ MHz}$ . The loaded Q of the EPR coil was determined using a vector network analyzer and an untuned pick up coil to measure the transmission response of the EPR coil (S21). The measured Q of 62 corresponds to a bandwidth of  $\sim 2.3 \text{ MHz}$ , thus the spread in electron spin frequencies during the phase encode step is well covered.

*Compressed sensing*

Most images are sparse in the sense that they can be accurately represented with fewer coefficients than one would assume given their spectral bandwidth (38). Compressed sensing (CS) is a framework for exploiting sparsity to reconstruct high-fidelity MR images from undersampled k-space datasets that do not fulfill the Nyquist sampling theorem. In CS image reconstruction, image sparsity is enforced by truncating the small coefficients of an object's representation in a *sparse basis*, typically chosen to be a wavelet transform domain. During image reconstruction, the data are transformed from k-space (the *sensing basis*) into the wavelet basis via a sparsifying transform,  $\Psi$ , taken for the present work to be the Dirichlet wavelet transform.

Compressed sensing uses norms to modify the objective function that is optimized during image reconstruction. To understand the role of norms in the objective function, it is helpful to recall standard Fourier reconstruction. For a discrete image  $m$ , Fourier operator  $F$ , and k-space dataset  $y$ , the  $L_2$ -norm,  $\|Fm - y\|_2 = \left( \sum_i |(Fm)_i - y_i|^2 \right)^{1/2}$ , is implicitly used to find an image whose Fourier transform differs as little as possible from the k-space data in the Euclidean sense. For fully sampled data, the least squares solution is provided by the Fourier transform. In the case of



underdetermined matrix problems (as when the k-space data is undersampled), the  $L_2$ -norm may be additionally used to constrain image reconstruction so as to reduce the noise (an approach known as Tikhonov regularization). However, when the  $L_2$ -norm is used in this way, it functions as a low-pass filter, penalizing noise at the expense of introducing bias. It does not promote image sparsity. By contrast, the  $L_1$ -norm, defined as  $\|x\|_1 = \sum_i |x_i|$  for an arbitrary function  $x$ , has a tendency to preserve edges and large coefficients, e.g., for neighboring voxels  $\{0,3,0\}$  the  $L_2$ -norm will tend to penalize the difference toward  $\{1,1,1\}$ , while the  $L_1$ -norm of both cases is the same, tending to preserve the edge.

The ability of the  $L_1$ -norm to preserve large coefficients makes it an appealing choice for enforcing sparsity in images (39,40). In the compressed sensing framework, the  $L_1$ -norm is applied to the wavelet transform of the image, where it naturally selects the large coefficients representing image features while reducing the small coefficients corresponding to noise and incoherent artifacts. For additional denoising and artifact suppression, a finite difference norm (a discrete implementation of the Total Variation, or  $TV$ , norm) is applied in the image domain (41). This norm has been shown to preserve object edges while eliminating noise.

As shown in (42), the resulting image reconstruction problem is expressed as a balance between the  $L_1$ -norm constraints and the  $L_2$ -norm data consistency constraint:

$$\min \left[ \|F_u m - y\|_2 + \alpha \|\Psi m\|_1 + \beta TV(m) \right]$$

where  $F_u$  is the undersampled Fourier transform operator,  $y$  is the undersampled k-space data, and coefficients  $\alpha$  and  $\beta$  weight the relative contributions of each norm to the final image. A variety of algorithms are available for minimizing this nonlinear objective function (42). Specific details about our implementation of compressed sensing for OMRI b-SSFP are given below.

### *Undersampled OMRI b-SSFP*

The use of CS in MRI relies on the possibility to acquire *a priori* compressed information and be able to reconstruct the original image as if the latter was fully sampled (42). In the context of data acquisition, this motivates the use of undersampling. Compressed sensing has been found to work best when k-space is randomly undersampled so as to produce incoherent artifacts rather



than the familiar wrap-around ghosts due to field-of-view (FOV) contraction when k-space lines are skipped in a regular coherent pattern as is done in conventional parallel imaging (43). For the images presented here, a choice was made to acquire random lines of k-space chosen in the phase-encode directions ( $k_y$ ,  $k_z$ ) following a Gaussian probability density function. The readout direction was fully sampled. The standard deviations of the sampling pattern as a fraction of the FOV along y and z,  $\sigma_y$  and  $\sigma_z$  respectively, were adjusted manually to preserve adequate high-frequency information for each undersampling rate. We investigated 4 undersampling fractions, 50%, 70%, 80% and 90%. The undersampling patterns are shown in Figure 5. On the acquisition side, this resulted in programming different phase encode tables for each undersampled sequence. The total acquisition time for each undersampling rate is shown in Table 1. To perform image reconstruction according to the  $L_1$ -norm and the data consistency constraints, the Sparse MRI code (<http://www.eecs.berkeley.edu/~mlustig/Software.html>) was used. This code solves this optimization problem using a nonlinear conjugate gradient method along with backtracking line-search as described in (42). The parameters for the wavelet and image domain norms were tuned manually to produce low-noise images with preserved object features. The missing values in the acquired k-space data were made identically zero. To separate out the data into slices, a Fourier transform was performed along the readout direction (x). Each sagittal slice of k-space data (y-z plane) was then fed individually into the Sparse MRI algorithm. After all slices were reconstructed, the resulting 3D block of image domain data was then displayed as transverse (x-y) slices. The computation time for a laptop equipped with a 2.3 GHz quad-core processor was 4.5 min, permitting CS image reconstruction immediately following k-space acquisition.

**Results**

*Steady-state signal with embedded EPR pulses*

In order to understand the approach of transverse magnetization to steady state with embedded EPR pulses in the sequence, Bloch simulations were performed without the phase encode



gradients and compared to acquired data. The results are shown in Figure 4. The data was normalized such that the maximum measured signal and the maximum simulated signal were both set to 1. The experimental data with DNP ( $\square$ ) begins at thermal equilibrium, but rapidly builds up to 30 times that of the non-DNP data ( $\circ$ ). This build up corresponds to the  $T_1$  relaxation time of the sample (545 ms). The signal reaches approximately 90% of its steady state value after 24 echoes, or 1.3 s, and the simulation is in good agreement with the data (dashed line; not a fit).

### *Fully sampled versus undersampled*

Images for the two different phantom configurations, 1 and 2, are shown in Figures 6 and 7 respectively after CS reconstruction. Images reconstructed from fully sampled k-space and from 50%, 70%, 80%, and 90% undersampling are shown. Figure 6.a and 6.b show the top and center structures of the interlocking cones (configuration 1). Figure 6.c displays 3D rendered images of the segmented cones for each undersampling rate. Figure 7.a-e shows the different segments of the phantom in configuration 2. For both phantom configurations, 50% and 70% undersampling reproduces the fully sampled images well. Even small structures such as 2 mm diameter holes (Figure 6.a), 1 and 1.5 mm solid separators and 2.5 mm holes (marked by white arrows in Figure 7.b,c,d) are well resolved at 70% undersampling. For 80% and 90% undersampling most of the structures are still visible though substantial blurring and ghosting artifacts begin to appear. Figure 7.a and 7.e correspond to the top and bottom slice of the phantom and show lower signal magnitude due to the  $B_1$  profile of the EPR coil. The maximum SNR was calculated from maximal signal amplitudes divided by two times the standard deviation of a user defined noise region before and after CS reconstruction and is shown in Table 1. The increase in SNR with undersampling rate is due to the undersampling pattern acting as an apodization filter that removes high spatial frequencies from k-space. However, all images show an increase in SNR after CS reconstruction. The SNR enhancement using CS increases with the initial SNR of the image and ranges from about 1.5 to 2.5.

To quantify the errors that occur in the undersampled images, the mean absolute error (MAE) was calculated for each image (Table 1). The MAE was calculated by first thresholding the images such that only points that were five times greater than the noise ( $\sigma_n$ ) were kept. The



undersampled image was then subtracted from the fully sampled image and all non-zero values counted as an error. As seen in Table 1, the MAEs for the 50% and 70% undersampling rates are small and comparable while those for 80% and 90% increase significantly. The MAE for each of the 32 phase encode gradients along z for configuration 1 is shown in Figure 8 for all undersampling rates. There is little difference across the entire sample between 50% and 70%, again showing that the image is well reproduced with only 30% of the k-space data. Losses in SNR due to the  $B_1$  profile of the EPR coil on slices 1-5 and 25-32 result in increased MAE values for all undersampling rates.

*SAR considerations*

A problem limiting the use of OMRI is that the high power RF pulses necessary for DNP lead to high SAR. Two methods were used to estimate SAR. A fiber optic temperature probe was placed inside the sample and the fully sampled k-space sequence was run several times, waiting several minutes in between runs to allow the EPR coil to cool. The maximum measured temperature increase was  $0.4^{\circ}\text{C}$ . No temperature increase was measured for any of the undersampled sequences. Estimating  $\text{SAR} \sim c\Delta T/\Delta t$  (44) where  $c$  is the specific heat,  $\Delta T$  is the temperature change and  $\Delta t$  is the time of the sequence gives  $\text{SAR} \sim 15 \text{ W}\cdot\text{kg}^{-1}$ . We expect this to represent a lower limit as heat may have dissipated during the sequence. As a second method, the power dissipated in the sample was estimated using (45):

$$P_{\text{sample}} = P_{\text{coil}}(1 - Q_{\text{loaded}}/Q_{\text{unloaded}})$$

The forward power was measured using a directional coupler (Model 3020A, Narda Microwave Co., Hauppauge, NY, USA) and power meter (V3500A, Agilent Technologies, Santa Clara, CA, USA), and the maximum forward power to the coil was  $\sim 62 \text{ W}$ . The loaded  $Q$  was measured to be 52 while the unloaded  $Q$  was 62. Thus the power to the sample during an EPR pulse is  $\sim 10 \text{ W}$ . The EPR irradiation is on for 73% of TR and the sample mass is 0.25 kg, therefore  $\text{SAR} \sim 29 \text{ W}\cdot\text{kg}^{-1}$ .

The 50% undersampled images in figures 6 and 7 have high SNR and accurately represent the phantom. Therefore we reduced the forward power to the coil by factors of 2, 4, 8,



and 16 to investigate how much the SAR could be reduced (thusly reducing the Overhauser enhancement) while maintaining high image quality. The results are shown in Figure 9 and table 2. Image quality is well maintained for 31 and 15.5 W forward power corresponding to an estimated SAR of  $\sim 14.5$ , and  $7.25 \text{ W}\cdot\text{kg}^{-1}$  respectively.

## Discussion

The 3D Overhauser-enhanced b-SSFP sequence presented here in combination with compressed sensing and undersampling techniques allows us to attain  $1 \times 2 \times 3.5 \text{ mm}^3$  voxel size in our phantom in 33 s (70% undersampling in Figures 6 and 7) at 6.5 mT. The resulting CS reconstructed image is nearly identical to the original fully sampled image and has  $\sim 2$  times higher SNR. This was achieved by inserting the EPR saturation pulses within TR during the pre-phase/re-phase gradients, thus removing the time consuming pre-polarization step as in other OMRI sequences. As shown in our experiments and simulations (Figure 4), a large steady-state signal is quickly reached with 90% of the maximum signal reached in less than 1.5 s, and constant polarization in the sample is maintained during the remainder of the acquisition. This eliminates the need to correct acquisitions for  $T_1$  decay and to rectify undesirable phase shifts that can occur when using pre-polarization techniques (25,46). The maximum signal with b-SSFP at thermal equilibrium is given by  $M_{ss} = \frac{1}{2} M_0 \sqrt{T_2/T_1} = 0.47 M_0$  (37). Overhauser saturation pulses during the phase gradient increases  $M_{ss}$  by approximately 30 for the sample used here, thus allowing high SNR images comparable to those obtained with conventional OMRI techniques. The simulations provide a reliable tool to optimize the phase encode gradient durations depending on  $T_1$  and  $T_2$ .

The application of EPR saturation pulses during the balanced phase encode gradient events is our first major source of acceleration. This allows us to acquire images twice as fast as spin echo OMRI sequences recently published in the literature (24) with nearly 7 times higher spatial resolution ( $1 \times 2 \times 3.5 \text{ mm}^3$  vs  $1.25 \times 1.25 \times 30 \text{ mm}^3$ ). This is possible by covering the spread in electron spin frequencies in the phantom when the maximum  $0.1 \text{ Gauss}\cdot\text{cm}^{-1}$  phase encode gradient was turned on. This sets an upper limit on the Q factor of the EPR coil, or alternatively, the maximum gradient strength that can be used for these experiments. While the maximum steady-state DNP enhancements would benefit from a higher Q coil, the goal of maintaining



nearly constant signal enhancement across the sample during imaging would suffer. However, when the EPR irradiation occurs as separate step before imaging as in other OMRI sequences, the DNP signal is also not constant across the image due to the decay of polarization, so a compromise of higher gradient strength for uneven DNP polarization may be acceptable.

Partial sampling of k-space (and subsequent reconstruction via CS) is our second major acceleration factor. In the case of 70% undersampling this results in an additional 3.5 fold acceleration while keeping the voxel size unchanged, thus resulting in 7 times faster acquisition compared to recently published work (24). By undersampling in each phase encode direction according to a Gaussian probability density function, the center of k-space is emphasized, preserving image contrast without completely sacrificing the high frequency information at the edge of k-space. However, the choice of the lines sampled in k-space was empirically determined and only a few undersampling patterns were empirically tested for a given undersampling rate. The degrees of freedom in the generation of undersampling patterns is large (choice of lines sampled,  $\sigma_{y,z}$ ) and a large number of combinations could have been tested with the opportunity to give even better results. However, for the  $\sigma_{y,z}$ 's used here, the 50% and 70% undersampling rates accurately reproduced the image for different random samplings of k-space. Also, this work focuses on Cartesian sampling, but alternative sampling trajectories (spiral, radial) have been shown to offer more flexibility in the design of 3D incoherent sampling sequences that are particularly well for the use of compressed sensing techniques (47-50).

Compressed sensing performs natural de-noising, bringing an improvement in SNR. Incoherent artifacts resulting from sub-sampled k-space are efficiently suppressed using  $L_1$ -norm constraints in the image and wavelet domains as previously detailed in the literature (42). However, more than 70% undersampling could not provide satisfying reconstruction in spite of high SNR. The incorporation of prior knowledge (51-53) in the image reconstruction process could overcome this limitation by partially recovering irretrievable loss of information caused by heavy undersampling and further increase our temporal resolution. In addition, it is important to note that the 4.5 min computation time required for the CS reconstruction does not significantly penalize the time saved from undersampling.

The gain in temporal resolution obtained here for 70 % undersampling, around 1 s per acquired slice, provides new insight for investigating cases where high temporal resolution is needed, such as monitoring the concentration change, oxidation, and metabolism of free radicals



that correlate directly with organ functions and tissue health. Also, shorter durations for the read and phase encode gradients could have been implemented to give significantly shorter acquisition times but at the cost of a decreased spatial resolution. Likewise, doubling the gradient strength in read and both phase encode directions would allow us to reach  $2^3$  times higher spatial resolution for a fixed acquisition time.

Considering the SAR resulting from the sequence, the amount of power sent to the EPR coil was decreased by a factor of 4 while still keeping the SNR greater than 25. Even if a compromise has to be found between the desired spatial resolution of the image and sample heating due to the high power RF, the total amount of RF power sent to the sample during imaging is considerably reduced by the use of undersampling strategies. No temperature rise was measured in the sample for the 50 to 90 % undersampling rates with the maximum EPR power used in this study. This allows the investigator to push the in-plane resolution of the acquired image to  $1 \times 1 \text{ mm}^2$  as shown in figure 10 with configuration 2, 70 % undersampling (while maintaining the 3.5 mm slice thickness), and maximum available power sent to the EPR coil. Total acquisition time was 65 s. This image displays excellent in-plane resolution with very little blurring of the 1 mm features and high SNR.

The images presented here were acquired with a sufficiently long TR to obtain the desired in-plane resolution while keeping the gradient strength low enough for efficient EPR saturation during phase encoding. We note that the phantom used here has significantly longer  $T_2$  and  $T_1$  relaxation times than would be expected for *in vivo* applications. Bloch simulations were run to estimate how the current sequence would perform with relaxation times 10 times shorter than the phantom used here. Keeping all simulation parameters as in Figure 4, but decreasing  $T_1$  to 55 ms and  $T_2$  to 49 ms resulted in less than a 15% reduction in signal intensity (compared to the dashed line in Fig. 4). While relaxation times comparable to TR tend to reduce signal, this is partially offset by a faster approach to steady state. More likely to hamper the effectiveness of OMRI *in vivo*, however, is a decrease in the maximum DNP signal enhancement due to extra  $^1\text{H}$  nuclear spin relaxation pathways that compete with relaxation caused by dipolar coupling to the electron spin (27). To observe this effect, simulations were run with the short  $T_1$  and  $T_2$  times above while decreasing the maximum DNP signal enhancement to -10 and -5. This reduced the steady state signal intensity by 80% and 90% respectively compared to the dashed line in Figure 4. Although the signal is much smaller, it is still a factor of 7 and 3.5 times larger than the



1  
2  
3  
4  
5  
6  
7  
8  
9  
10  
11  
12  
13  
14  
15  
16  
17  
18  
19  
20  
21  
22  
23  
24  
25  
26  
27  
28  
29  
30  
31  
32  
33  
34  
35  
36  
37  
38  
39  
40  
41  
42  
43  
44  
45  
46  
47  
48  
49  
50  
51  
52  
53  
54  
55  
56  
57  
58  
59  
60

thermal equilibrium signal with the same parameters, and therefore still provides very useful contrast. In the case of injected free radical detection, this decrease in signal can be partially overcome by increasing the free radical concentration. For example, injection of 0.6 mL 100 mM nitroxide radical in mice has been reported in recent work (24). Assuming 60-80 mL of blood per kg of bodyweight (54), the dilution factor is between 3 and 4 for a 30 g mouse, resulting in a nominal 29 mM free radical concentration, more than 10 times higher than the 2.5 mM used in the work presented here.

**Conclusion**

We have demonstrated a new strategy for fast high-resolution 3D Overhauser MRI using b-SSFP in a phantom containing 2.5 mM 4-hydroxy TEMPO solution at 6.5 mT. The embedding of EPR excitation pulses directly into the b-SSFP sequence eliminates the pre-polarization step used in other OMRI sequences, reducing the acquisition time and obviating the need for long, high power RF EPR pulses. The use of undersampling strategies and compressed sensing reconstruction algorithms further reduces imaging time. We have shown that an undersampling rate of 70 % gives unperceivable reconstruction errors when compared with the fully sampled data sets, allowing the acquisition of 32 slices in our phantom volume within 33 s. The presented work overcomes the main limitations of Overhauser enhanced MRI described so far in the literature with drastic improvement in terms of speed and resolution, thus offering new perspectives for the measurement of free radicals in living organisms, and for the study of dynamic processes such as metabolism and flow.



## References

1. Ardenkjaer-Larsen JH, Laursen I, Leunbach I, Ehnholm G, Wistrand LG, Petersson JS, Golman K. EPR and DNP properties of certain novel single electron contrast agents intended for oximetric imaging. *J Magn Reson* 1998;133:1–12.
2. James PE, Madhani M, Roebuck W, Jackson SK, Swartz HM. Endotoxin-induced liver hypoxia: defective oxygen delivery versus oxygen consumption. *Nitric Oxide* 2002;6:18–28.
3. Ahn KH, Scott G, Stang P, Conolly S, Hristov D. Multiparametric imaging of tumor oxygenation, redox status, and anatomical structure using overhauser-enhanced MRI-prepolarized MRI system. *Magn Reson Med* 2011;65:1416–1422.
4. Lurie DJ, Davies GR, Foster MA, Hutchison JMS. Field-cycled PEDRI imaging of free radicals with detection at 450 mT. *Magn Reson Imaging* 2005;23:175–181.
5. Massot P, Parzy E, Pourtau L, Mellet P, Madelin G, Marque S, Franconi J-M, Thiaudiere E. In vivo high-resolution 3D Overhauser-enhanced MRI in mice at 0.2 T. *Contrast Media Mol Imaging* 2012;7:45–50.
6. Kosem N, Naganuma T, Ichikawa K, Phumala Morales N, Yasukawa K, Hyodo F, Yamada K-I, Utsumi H. Whole-body kinetic image of a redox probe in mice using Overhauser-enhanced MRI. *Free Radic Biol Med* 2012;53:328–386.
7. Caia GL, Efimova OV, Velayutham M, El-Mahdy MA, Abdelghany TM, Kesselring E, Petryakov S, Sun Z, Samouilov A, Zweier JL. Organ specific mapping of in vivo redox state in control and cigarette smoke-exposed mice using EPR/NMR co-imaging. *J Magn Reson* 2012;216:21–27.
8. Mellet P, Massot P, Madelin G, Marque SRA, Harte E, Franconi J-M, Thiaudiere E. New concepts in molecular imaging: non-invasive MRI spotting of proteolysis using an overhauser effect switch. *PLoS ONE* 2009;4:e5244.
9. Halpern HJ, Chandramouli GV, Barth ED, Yu C, Peric M, Grdina DJ, Teicher BA. Diminished aqueous microviscosity of tumors in murine models measured with in vivo radiofrequency electron paramagnetic resonance. *Cancer Res* 1999;59:5836–5841.
10. Barros W, Engelsberg M. Enhanced Overhauser contrast in proton-electron double-resonance imaging of the formation of an alginate hydrogel. *J Magn Reson* 2007;184:101–107.
11. Eaton GR, Eaton SS, Ohno K. EPR imaging and in vivo EPR. Boca Raton: CRC Press; 1991.
12. Kuppusamy P, Chzhan M, Zweier J. Principles of imaging. In: Berliner LJ, editor. *Biological magnetic resonance*, Vol. 18. In vivo EPR (ESR): theory and applications. New York: Kluwer Academic/Plenum Publishers; 2003.p 99–152
13. Halpern HJ, Yu C, Peric M, Barth ED, Karczmar GS, River JN, Grdina DJ, Teicher BA.



Measurement of differences in pO<sub>2</sub> in response to perfluorocarbon/carbogen in FSa and NFSa murine fibrosarcomas with low-frequency electron paramagnetic resonance oximetry. *Radiat Res* 1996;145:610–618.

14. Halpern HJ, Yu C, Peric M, Barth E, Grdina DJ, Teicher BA. Oxymetry deep in tissues with low-frequency electron paramagnetic resonance. *Proc Natl Acad Sci* 1994;91:13047–13051.

15. Subramanian S, Yamada K-I, Irie A, Murugesan R, Cook JA, Devasahayam N, Van Dam GM, Mitchell JB, Krishna MC. Noninvasive in vivo oximetric imaging by radiofrequency FT EPR. *Magn Reson Med* 2002;47:1001–1008.

16. Velayutham M, Li H, Kuppusamy P, Zweier JL. Mapping ischemic risk region and necrosis in the isolated heart using EPR imaging. *Magn Reson Med* 2003;49:1181–1187.

17. He G, Samouilov A, Kuppusamy P, Zweier JL. In vivo imaging of free radicals: applications from mouse to man. *Mol Cell Biochem* 2002;234/235:359–367.

18. Lurie DJ, Bussell DM, Bell LH, Mallard JR. Proton-electron double magnetic resonance imaging of free radical solutions. *J Magn Reson* 1988;76:366–370.

19. Golman K, Petersson JS, Ardenkjaer-Larsen JH, Leunbach I, Wistrand LG, Ehnholm G, Liu K. Dynamic in vivo oxymetry using overhauser enhanced MR imaging. *J Magn Reson Imaging* 2000;12:929–938.

20. Krishna MC, English S, Yamada K, Yoo J, Murugesan R, Devasahayam N, Cook JA, Golman K, Ardenkjaer-Larsen JH, Subramanian S, Mitchell JB. Overhauser enhanced magnetic resonator imaging for tumor oximetry: coregistration of tumor anatomy and tissue oxygen concentration. *Proc Natl Acad Sci* 2002;99:2216–2221.

21. Utsumi H, Yamada K-I, Ichikawa K, Sakai K, Kinoshita Y, Matsumoto S, Nagai M. Simultaneous molecular imaging of redox reactions monitored by Overhauser-enhanced MRI with <sup>14</sup>N- and <sup>15</sup>N-labeled nitroxyl radicals. *Proc Natl Acad Sci* 2006;103:1463–1468.

22. Li H, He G, Deng Y, Kuppusamy P, Zweier JL. In vivo proton electron double resonance imaging of the distribution and clearance of nitroxide radicals in mice. *Magn Reson Med* 2006;55:669–675.

23. Benial AM, Ichikawa K, Murugesan R, Yamada K, Utsumi H. Dynamic nuclear polarization properties of nitroxyl radicals used in Overhauser-enhanced MRI for simultaneous molecular imaging. *J Magn Reson* 2006;182:273–282.

24. Sun Z, Li H, Petryakov S, Samouilov A, Zweier JL. In vivo proton electron double resonance imaging of mice with fast spin echo pulse sequence. *J Magn Reson Imaging* 2012;35:471–475.

25. Youngdee W, Lurie DJ, Foster MA. Rapid imaging of free radicals in vivo using hybrid FISP field-cycled PEDRI. *Phys Med Biol* 2002;47:1091–1100.

26. Tsai LL, Mair RW, Rosen MS, Patz S, Walsworth RL. An open-access, very-low-field MRI



system for posture-dependent  $^3\text{He}$  human lung imaging. *J Magn Reson* 2008;193:274–285.

27. Hausser KH, Stehlik D. Dynamic nuclear polarization in liquids. *Adv Magn Reson* 1968;3:79–139.

28. Muller-Warmuth W, Meise-Gresch K. Molecular motions and interactions as studied by dynamic nuclear polarization (DNP) in free radical solutions. *Adv Magn Reson* 1983;11:1–45.

29. Alderman DW, Grant DM. An efficient decoupler coil design which reduces heating in conductive samples in superconducting spectrometers. *J Magn Reson* 1979;36:447–451.

30. Lurie DJ, Li H, Petryakov S, Zweier JL. Development of a PEDRI free-radical imager using a 0.38 T clinical MRI system. *Magn Reson Med* 2002;47:181–186.

31. Rabi II, Zacharias JR, Millman S, Kusch P. A new method of measuring nuclear magnetic moment. *Phys Rev* 1938;53:318.

32. Bottomley PA, Andrew ER. RF magnetic field penetration, phase shift and power dissipation in biological tissue: implications for NMR imaging. *Phys Med Biol* 1978;23:630–643.

33. Jin J. Electromagnetic analysis and design in magnetic resonance imaging. CRC Press;1998.

34. Collins CM, Li S, Smith MB. SAR and B1 field distributions in a heterogeneous human head model within a birdcage coil. Specific energy absorption rate. *Magn Reson Med* 1998;40:847–856.

35. Collins CMC, Smith MBM. Calculations of B(1) distribution, SNR, and SAR for a surface coil adjacent to an anatomically-accurate human body model. *Magn Reson Med* 2001;45:692–699.

36. Collins CM, Wang Z. Calculation of radiofrequency electromagnetic fields and their effects in MRI of human subjects. *Magn Reson Med* 2011;65:1470–1482.

37. Scheffler K, Lehnhardt S. Principles and applications of balanced SSFP techniques. *Eur Radiol* 2003;13:2409–2418.

38. Candes EJ, Romberg J, Tao T. Robust uncertainty principles: exact signal reconstruction from highly incomplete frequency information. *IEEE Trans Inform Theory* 2006;52:489–509.

39. Donoho DL. Compressed sensing. *IEEE Trans Inform Theory* 2006;52:1289–1306.

40. Candes EJ, Wakin MB. An introduction to compressive sampling. *Signal Processing Magazine, IEEE*. 2008;25:21–30.

41. Rudin LI, Osher S, Fatemi E. Nonlinear total variation based noise removal algorithms. *Physica D: Nonlinear Phenomena* 1992;60:259–268.

42. Lustig M, Donoho D, Pauly JM. Sparse MRI: The application of compressed sensing for rapid MR imaging. *Magn Reson Med* 2007;58:1182–1195.



1  
2  
3  
4  
5  
6  
7  
8  
9  
10  
11  
12  
13  
14  
15  
16  
17  
18  
19  
20  
21  
22  
23  
24  
25  
26  
27  
28  
29  
30  
31  
32  
33  
34  
35  
36  
37  
38  
39  
40  
41  
42  
43  
44  
45  
46  
47  
48  
49  
50  
51  
52  
53  
54  
55  
56  
57  
58  
59  
60

43. Pruessmann KP, Weiger M, Scheidegger MB, Boesiger P. SENSE: sensitivity encoding for fast MRI. *Magn Reson Med* 1999;42:952–962.

44. Oh S, Webb AG, Neuberger T, Park B, Collins CM. Experimental and numerical assessment of MRI-induced temperature change and SAR distributions in phantoms and in vivo. *Magn Reson Med* 2010;63:218–223.

45. Matsumoto S, Yamada K, Hirata H, Yasukawa K, Hyodo F, Ichikawa K, Utsumi H. Advantageous application of a surface coil to EPR irradiation in overhauser-enhanced MRI. *Magn Reson Med* 2007;57:806–811.

46. Puwanich P, Lurie DJ, Foster MA. Rapid imaging of free radicals in vivo using field cycled PEDRI. *Phys Med Biol* 1999;44:2867–2877.

47. Lustig M, Lee J, Donoho D, Pauly J. Faster imaging with randomly perturbed, undersampled spirals and L1 reconstruction. In *Proceedings of the 13th Annual Meeting of ISMRM, Miami Beach, Florida, USA, 2005*. p. 155.

48. Santos JM, Cunningham CH, Lustig M, Hargreaves BA, Hu BS, Nishimura DG, Pauly JM. Single breath-hold whole-heart MRA using variable-density spirals at 3T. *Magn Reson Med* 2006;55:371–379.

49. Ye JC, Tak S, Han Y, Park HW. Projection reconstruction MR imaging using FOCUSS. *Magn Reson Med* 2007;57:764–775.

50. Block KT, Uecker M, Frahm J. Undersampled radial MRI with multiple coils. Iterative image reconstruction using a total variation constraint. *Magn Reson Med* 2007;57:1086–1098.

51. Mistretta CA, Wieben O, Velikina J, Block W, Perry J, Wu Y, Johnson K, Wu Y. Highly constrained backprojection for time-resolved MRI. *Magn Reson Med* 2005;55:30–40.

52. Chen G-H, Tang J, Leng S. Prior image constrained compressed sensing (PICCS): a method to accurately reconstruct dynamic CT images from highly undersampled projection data sets. *Med Phys* 2008;35:660–663.

53. Lauzier PT, Tang J, Chen G-H. Prior image constrained compressed sensing: Implementation and performance evaluation. *Med Phys* 2012;39:66–80.

54. Sluiter W, Oomens LWM, Brand A, Van Furth R. Determination of blood volume in the mouse with 51Chromium-labelled erythrocytes. *J. Immunol. Methods* 1984;73:221–225



## Figure Captions

Figure 1. OMRI setup. Photographs of (a) the custom built 6.5 mT MR scanner with bi-planar electromagnet and gradient set inside the shielded room, (b) the EPR (141 MHz) and (c) NMR (276 kHz) coils used for the OMRI experiments.

Figure 2. Photograph of (1a) the assembled OMRI phantom, (2a) a 10 mm thick internal piece, and (3a) a stack of internal pieces. Shown in (b-h) are individual pieces of the phantom in configuration 1 (f-h) and configuration 2 (b-e). A top view of the stacked pieces for the phantom in configuration 1 as described in the text is shown in (i).

Figure 3. Diagram of the 3D b-SSFP sequence with embedded EPR pulses (rf EPR). N is the total number of TRs in the sequence.

Figure 4. Simulation and measurement of the approach to steady-state with- and without DNP. Plotted are the echo amplitudes acquired during the pulse sequence in Figure 3 with only the read gradient active. The DNP signal is nearly 30 times larger than the signal without DNP after reaching steady-state. Solid curves plotted are not a fit to the data but an exact simulation with no free parameters as described in the text.

Figure 5. Undersampling (US) patterns used for (a) 50% undersampling, (b) 70% undersampling, (c) 80% undersampling, and (d) 90% undersampling. For an undersampling rate of 50%, 995 of 2048 lines were acquired. For 70% undersampling, 585 of 2048 lines were acquired. For 80% and 90% undersampling, 383 and 185 of 2048 lines were acquired respectively.

Figure 6. Fully and undersampled (US) images of the phantom in configuration 1 after CS reconstruction as a function of undersampling fraction. a) Representative slices: Top (a) and center (b) of the full 32 slice dataset. Acquisition matrix:  $128 \times 64 \times 32$ , voxel size:  $2 \times 1 \times 3.5 \text{ mm}^3$ . C) 3D rendered images of the interlocked cones structure obtained from the fully and undersampled datasets.

Figure 7. Fully and undersampled (US) images of 5 representative slices after CS reconstruction. The full 32-slice data set was acquired with the phantom in configuration 2 as described in the text. MR images are shown alongside photographs of the corresponding phantom piece. Acquisition matrix:  $128 \times 64 \times 32$ , voxel size:  $2 \times 1 \times 3.5 \text{ mm}^3$ . White arrows show 1 and 1.5 mm solid separators, (b) and (d) respectively, and 2.5 mm diameter structures (c).

Figure 8. Mean absolute error (MAE) computed each slice number for each undersampling fraction with the phantom in configuration 1: 50% US (black), 70% US (red), 80% US (green), 90% US (blue).

Figure 9. Images taken with the phantom in configuration 2 and 50% undersampling as a function of Overhauser drive power: (a) 62 W, (b) 31 W, (c) 15.5 W, (d) 7.8 W, and (e) 3.9 W EPR power. Acquisition matrix:  $128 \times 64 \times 32$ , voxel size:  $2 \times 1 \times 3.5 \text{ mm}^3$ , TR/TE: 54/27 ms. Total acquisition time per image was 56 s.

Figure 10. High-resolution CS reconstructed images taken in the phantom in configuration 2 (5 slices are shown) with 70% undersampling. Acquisition matrix:  $256 \times 64 \times 32$ , voxel size:  $1 \times 1 \times 3.5 \text{ mm}^3$ , TR/TE: 54/27 ms. Total acquisition time was 65 s.



1  
2  
3  
4  
5  
6  
7  
8  
9  
10  
11  
12  
13  
14  
15  
16  
17  
18  
19  
20  
21  
22  
23  
24  
25  
26  
27  
28  
29  
30  
31  
32  
33  
34  
35  
36  
37  
38  
39  
40  
41  
42  
43  
44  
45  
46  
47  
48  
49  
50  
51  
52  
53  
54  
55  
56  
57  
58  
59  
60

Tables

Table 1. Comparison of acquisition time, maximum SNR, and mean absolute error (MAE) as a function of the undersampling rate for the two different phantom configurations with the maximum applied RF power of 62 W at the EPR coil.

	Acq. time (s)	maximum SNR		MAEs
		no CS	CS	
Configuration 1				
Fully sampled	114	23	40.6	
50% undersampling	56	35.8	75.8	0.073±0.006
70% undersampling	33	44.6	95	0.072±0.008
80% undersampling	21	64.3	160	0.112±0.011
90% undersampling	10	69.8	148	0.149±0.014
Configuration 2				
Fuly sampled	114	24.6	42.6	
50% undersampling	56	30.47	49.7	0.049±0.005
70% undersampling	33	42	78.3	0.059±0.010
80% undersampling	21	49.9	94.7	0.100±0.013
90% undersampling	10	58.1	88.3	0.114±0.014



Table 2. The maximum SNR as a function of power at the EPR coil with and without CS for the phantom in configuration 2.

Power to EPR coil (W)	Max. SNR	
	no CS	CS
62	36	75
31	29.3	48
15.5	21	26.4
7.8	15.2	18.2
3.9	11.4	16.2



1  
2  
3  
4  
5  
6  
7  
8  
9  
10  
11  
12  
13  
14  
15  
16  
17  
18  
19  
20  
21  
22  
23  
24  
25  
26  
27  
28  
29  
30  
31  
32  
33  
34  
35  
36  
37  
38  
39  
40  
41  
42  
43  
44  
45  
46  
47  
48  
49  
50  
51  
52  
53  
54  
55  
56  
57  
58  
59  
60

**Acknowledgments**

The authors thank Ronald Walsworth and Stephen DeVience for assistance with relocating and upgrading the low-field scanner, Jennifer McNab and Thomas Witzel for valuable discussions on implementing b-SSFP sequences at 6.5 mT, and David Donoho and Michael Lustig for sharing the package wavelet toolbox (Wavelab) online with the scientific community. This research was supported by the Department of Defense, Defense Medical Research and Development Program, Applied Research and Advanced Technology Development Award W81XWH-11-2-0076 (DM09094).



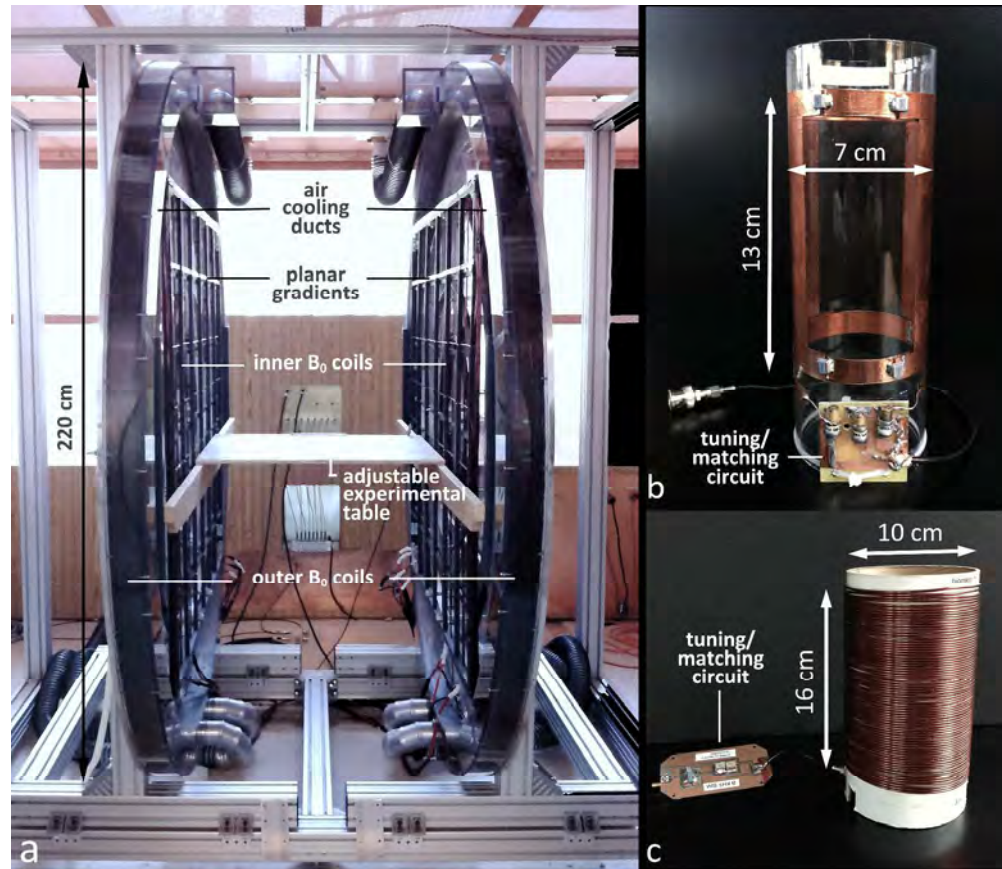


Figure 1. OMRI setup. Photographs of (a) the custom built 6.5 mT MR scanner with bi-planar electromagnet and gradient set inside the shielded room, (b) the EPR (141 MHz) and (c) NMR (276 kHz) coils used for the OMRI experiments.

943x816mm (600 x 600 DPI)



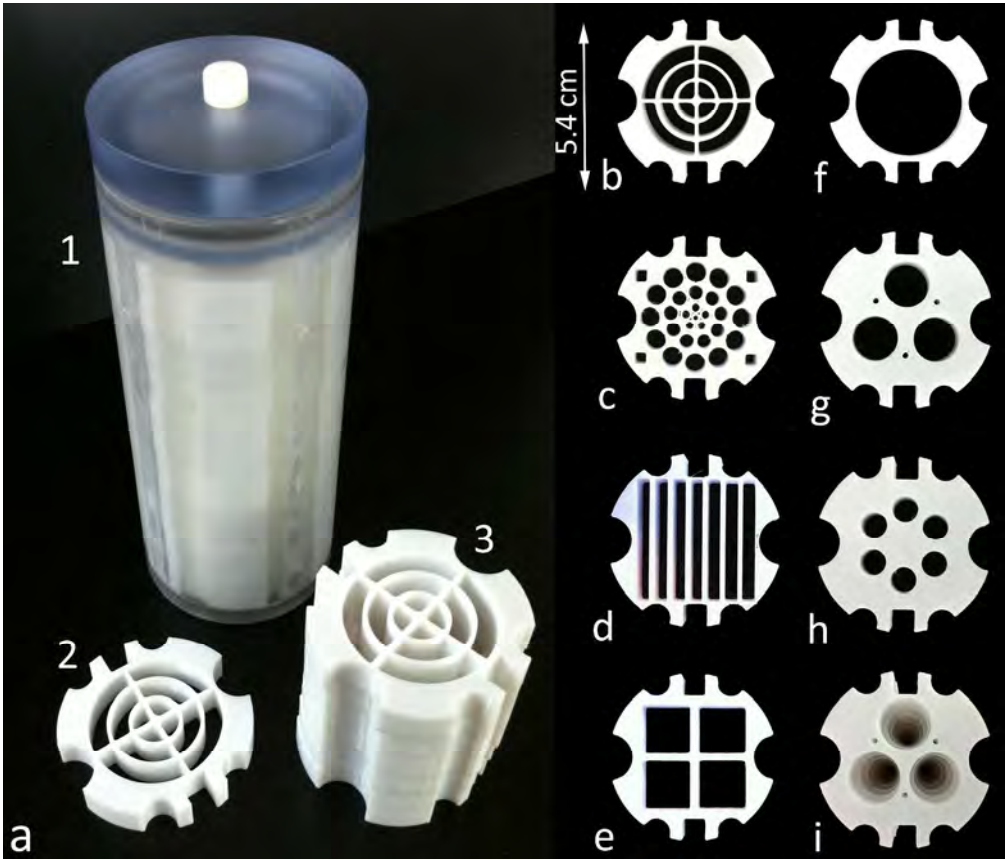


Figure 2. Photograph of (1a) the assembled OMRI phantom, (2a) a 10 mm thick internal piece, and (3a) a stack of internal pieces. Shown in (b-h) are individual pieces of the phantom in configuration 1 (f-h) and configuration 2 (b-e). A top view of the stacked pieces for the phantom in configuration 1 as described in the text is shown in (i).  
869x743mm (600 x 600 DPI)



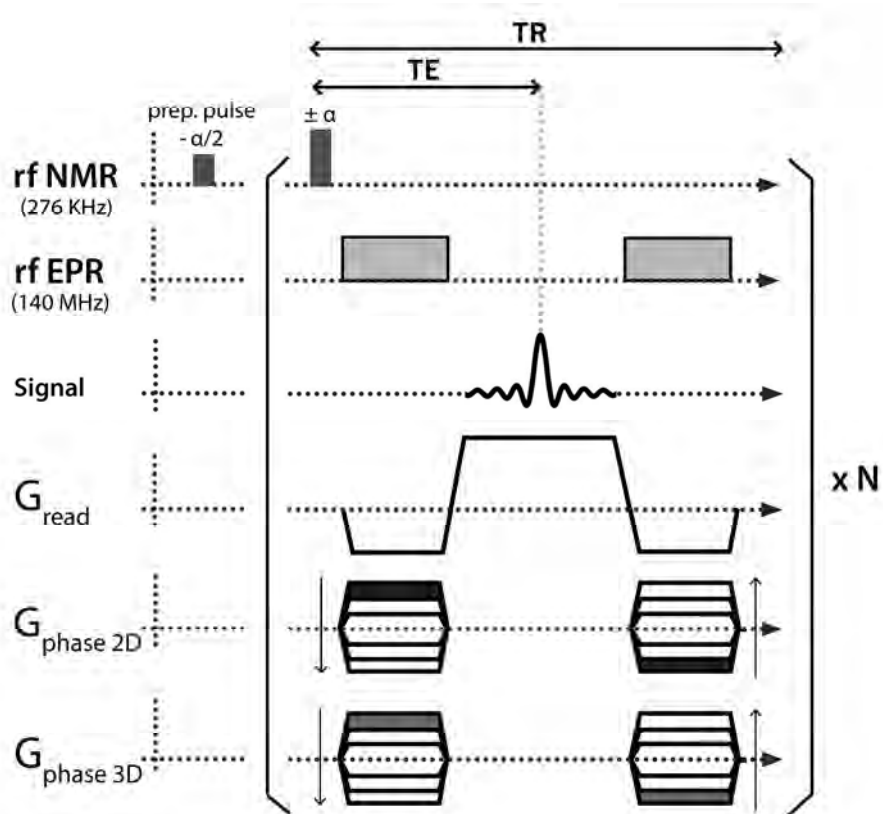


Figure 3. Diagram of the 3D b-SSFP sequence with embedded EPR pulses (rf EPR).  $N$  is the total number of TRs in the sequence.  
199x166mm (300 x 300 DPI)



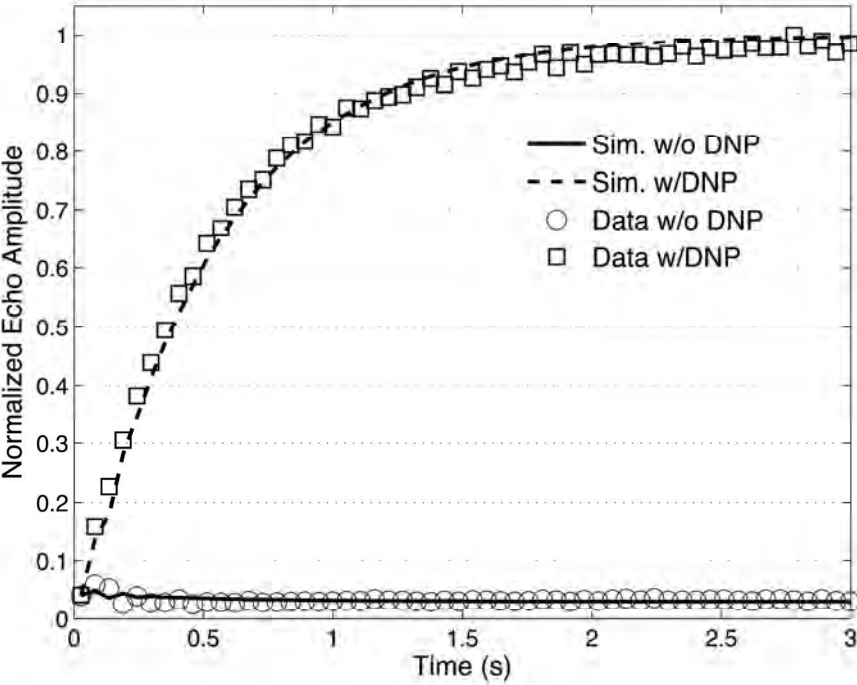


Figure 4. Simulation and measurement of the approach to steady-state with- and without DNP. Plotted are the echo amplitudes acquired during the pulse sequence in Figure 3 with only the read gradient active. The DNP signal is nearly 30 times larger than the signal without DNP after reaching steady-state. Solid curves plotted are not a fit to the data but an exact simulation with no free parameters as described in the text.

137x103mm (300 x 300 DPI)



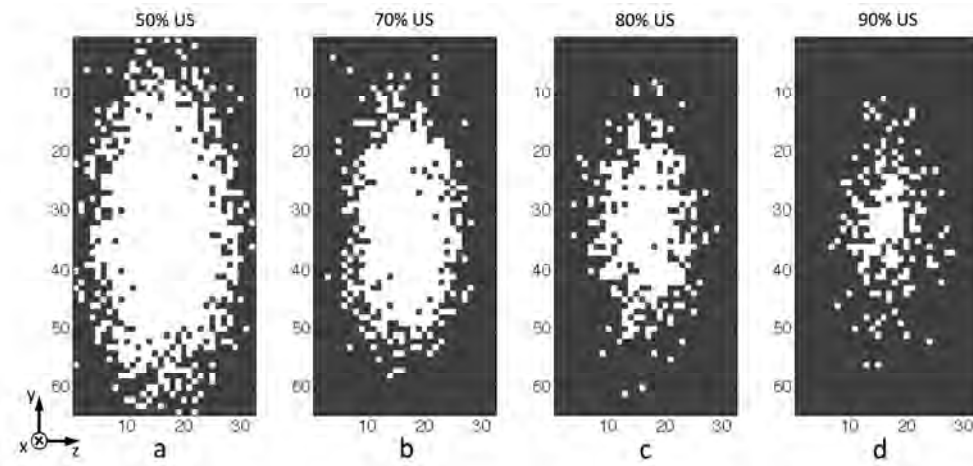


Figure 5. Undersampling (US) patterns used for (a) 50% undersampling, (b) 70% undersampling, (c) 80% undersampling, and (d) 90% undersampling. For an undersampling rate of 50%, 995 of 2048 lines were acquired. For 70% undersampling, 585 of 2048 lines were acquired. For 80% and 90% undersampling, 383 and 185 of 2048 lines were acquired respectively.  
168x77mm (300 x 300 DPI)



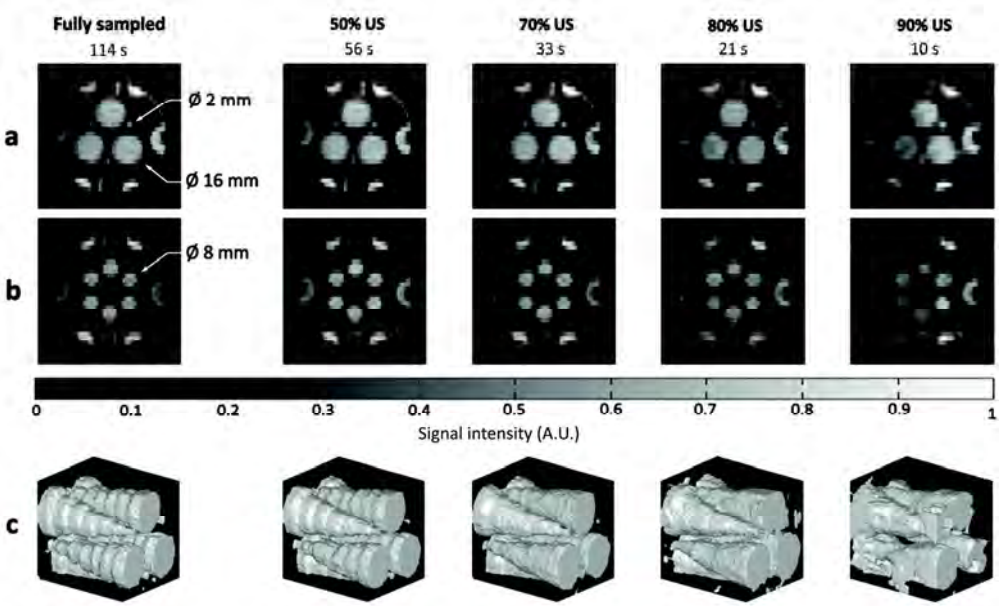


Figure 6. Fully and undersampled (US) images of the phantom in configuration 1 after CS reconstruction as a function of undersampling fraction. a) Representative slices: Top (a) and center (b) of the full 32 slice dataset. Acquisition matrix: 128x64x32, voxel size: 2x1x3.5 mm<sup>3</sup>. C) 3D rendered images of the interlocked cones structure obtained from the fully and under-sampled datasets. 221x137mm (300 x 300 DPI)



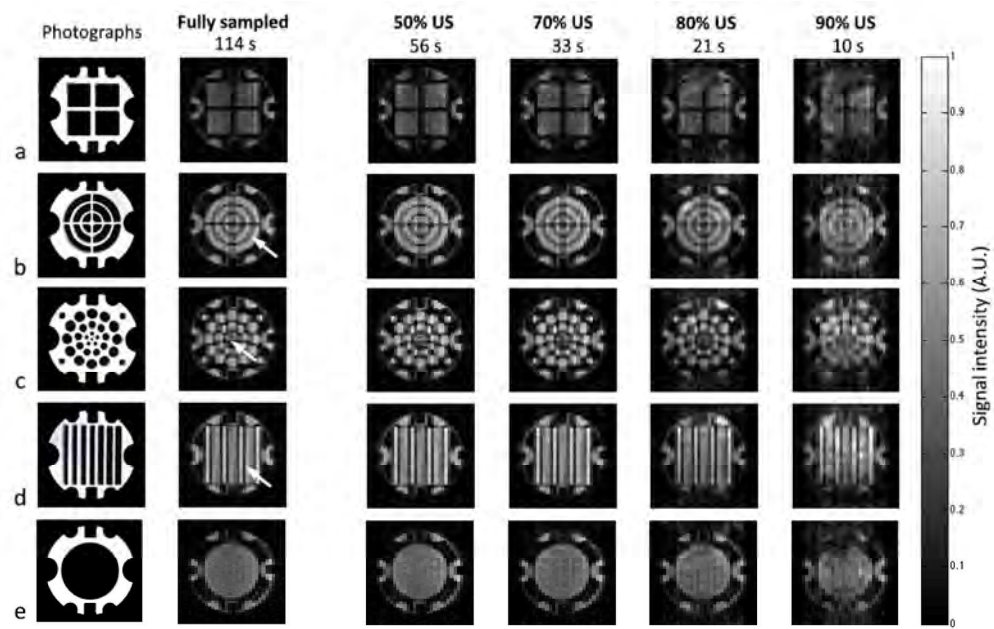


Figure 7. Fully and undersampled (US) images of 5 representative slices after CS reconstruction. The full 32-slice data set was acquired with the phantom in configuration 2 as described in the text. MR images are shown alongside photographs of the corresponding phantom piece. Acquisition matrix: 128x64x32, voxel size: 2x1x3.5 mm<sup>3</sup>. White arrows show 1 and 1.5 mm solid separators, (b) and (d) respectively, and 2.5 mm diameter structures (c).  
163x106mm (300 x 300 DPI)



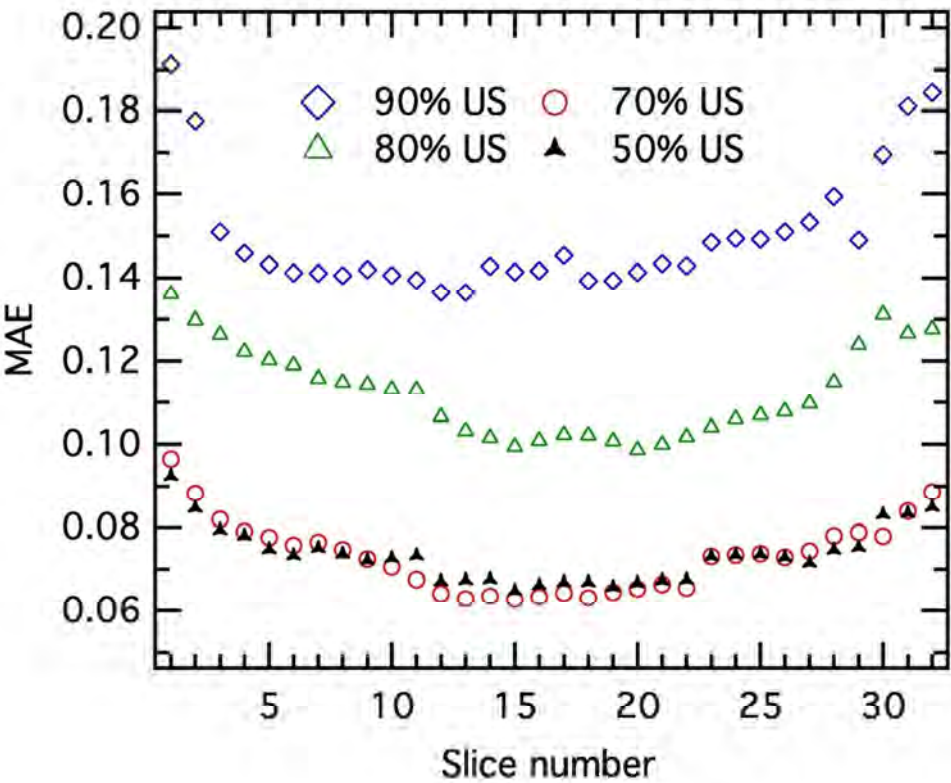


Figure 8. Mean absolute error (MAE) computed each slice number for each undersampling fraction with the phantom in configuration 1: 50% US (black), 70% US (red), 80% US (green), 90% US (blue). 84x70mm (300 x 300 DPI)



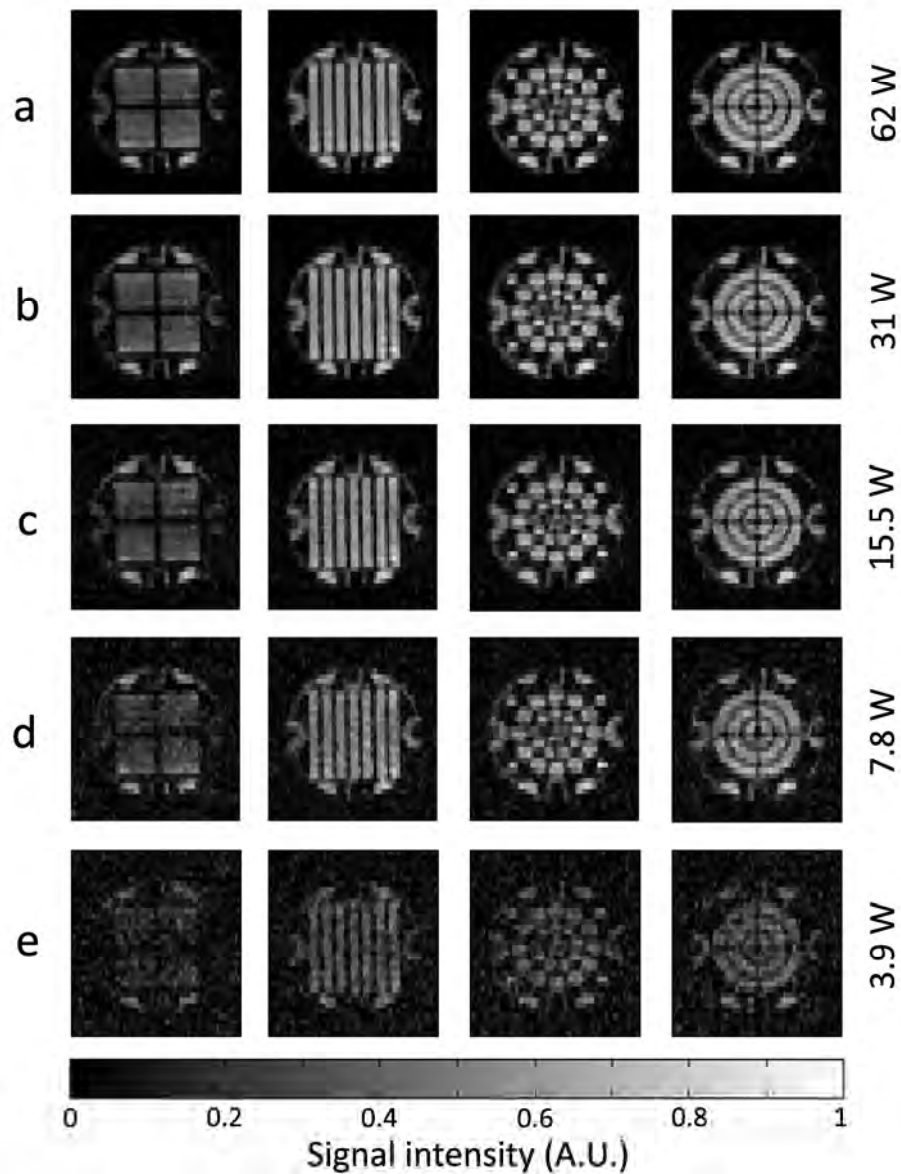


Figure 9. Images taken with the phantom in configuration 2 and 50% undersampling as a function of Overhauser drive power: (a) 62 W, (b) 31 W, (c) 15.5 W, (d) 7.8 W, and (e) 3.9 W EPR power. Acquisition matrix: 128x64x32, voxel size: 2x1x3.5 mm<sup>3</sup>, TR/TE: 54/27 ms. Total acquisition time per image was 56 s. 204x267mm (300 x 300 DPI)



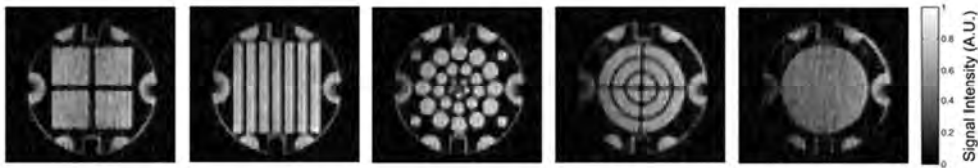


Figure 10. High-resolution CS reconstructed images taken in the phantom in configuration 2 (5 slices are shown) with 70% undersampling. Acquisition matrix: 256x64x32, voxel size: 1x1x3.5 mm<sup>3</sup>, TR/TE: 54/27 ms. Total acquisition time was 65 s.  
70x12mm (300 x 300 DPI)

1  
2  
3  
4  
5  
6  
7  
8  
9  
10  
11  
12  
13  
14  
15  
16  
17  
18  
19  
20  
21  
22  
23  
24  
25  
26  
27  
28  
29  
30  
31  
32  
33  
34  
35  
36  
37  
38  
39  
40  
41  
42  
43  
44  
45  
46  
47  
48  
49  
50  
51  
52  
53  
54  
55  
56  
57  
58  
59  
60



## Tables

Table 1. Comparison of acquisition time, maximum SNR, and MAE as a function of the undersampling rate for the two different phantom configurations with the maximum applied RF power of 62 W at the EPR coil.

	Acq. time (s)	maximum SNR		MAEs
		no CS	CS	
<b>Configuration 1</b>				
Fully sampled	114	23	40.6	
50% undersampling	56	35.8	75.8	0.073±0.006
70% undersampling	33	44.6	95	0.072±0.008
80% undersampling	21	64.3	160	0.112±0.011
90% undersampling	10	69.8	148	0.149±0.014
<b>Configuration 2</b>				
Fuly sampled	114	24.6	42.6	
50% undersampling	56	30.47	49.7	0.049±0.005
70% undersampling	33	42	78.3	0.059±0.010
80% undersampling	21	49.9	94.7	0.100±0.013
90% undersampling	10	58.1	88.3	0.114±0.014



1  
2  
3  
4  
5  
6  
7  
8  
9  
10  
11  
12  
13  
14  
15  
16  
17  
18  
19  
20  
21  
22  
23  
24  
25  
26  
27  
28  
29  
30  
31  
32  
33  
34  
35  
36  
37  
38  
39  
40  
41  
42  
43  
44  
45  
46  
47  
48  
49  
50  
51  
52  
53  
54  
55  
56  
57  
58  
59  
60

Table 2. The maximum SNR as a function of power at the EPR coil with and without CS for the phantom in configuration 2.

Power to EPR coil (W)	Max. SNR	
	no CS	CS
62	36	75
31	29.3	48
15.5	21	26.4
7.8	15.2	18.2
3.9	11.4	16.2